博士論文

Quantitative analysis of homeostatic T cell development in the thymus

(胸腺におけるT細胞生成プロセスの恒常性に関する定量生物学的研究)

令和元年11月29日提出

指導教員 小林 徹也 准教授

東京大学大学院工学系研究科

電気系工学専攻

37-177069

金子 和正

Acknowledgements

I would first like to express my deep appreciation to my supervisor, Prof. Tetsuya J. Kobayashi for providing invaluable mentorship in conducting research for the last five years. Your patient guidance and support for independence have shaped my scientific attitude. I am also indebted to you for providing me wonderful opportunities to encounter stimulating research communities by attending conferences and workshops.

I am grateful to my thesis committee, Professors Hitoshi Iba, Kazuyuki Aihara, Takashi Kohno, and Yasuyuki Ozeki, for their insights during committee meetings and their close reading of the manuscript.

The work presented in this thesis would not have been possible without the invaluable collaborators, Dr. Taishin Akiyama and the members of his laboratory, Ryosuke Tateishi, Takahisa Miyao, Dr. Yuki Takakura, Dr. Nobuko Akiyama, and Maki Miyauchi. I am blessed with the opportunity to explore my interest in the field of immunology with you.

I am extremely delighted to have wonderful colleagues, Dr. Ryo Yokota, Dr. Yuki Sughiyama, Dr. Yohei Saito, So Nakashima, Kento Nakamura, Takehiro Tottori, and Shuhei Horiguchi. Discussion with you on a wide range of topics was delightful and full of insights.

I would also like to thank Miho Aoki for efficient handling of complicated bureaucracy during my doctoral studies.

Finally, I would like to say a heartfelt thank you to my family for always supporting me to follow my curiosity.

Kazumasa Kaneko

Abstract

T cells play vital roles in the immune system. A diverse T cell receptor (TCR) repertoire is essential to defend the body against numerous kinds of pathogens, and a variety of T cell phenotypes shape sophisticated immune reactions to eliminate and remember pathogens while keeping cells of the body undamaged. The diverse TCR repertoire and the functional phenotype composition, along with a large number of cells, owe their origin to the thymus. T cell development in the thymus is thus essential for the immune system. Although we have accumulating evidence that T cell development is a homeostatic process in various aspects, it remains elusive how homeostatic T cell development is maintained. In this thesis, we quantitatively studied homeostasis of population size, TCR repertoire diversity, and intracellular signaling network in thymic T cell development utilizing mathematical modeling and high throughput sequence analysis.

Thymocytes, immature T cells in the thymus, differentiate in a stepwise manner. The differentiation process of a significant fraction of T cells is divided into three steps; $CD4^{-}CD8^{-}$ double negative (DN), $CD4^{+}CD8^{+}$ double positive (DP), and $CD4^{+}CD8^{-}$ single positive (SP4) stage. This differentiation process is regulated by mutual interactions with two types of thymic epithelial cells (TECs), cortical and medullary TECs (cTECs and mTECs). It remains unclear how the mutual interactions contribute to the stable population size of thymocytes and TECs. To address this problem, we construct a mathematical model for population dynamics of thymocytes and TECs during the recovery from irradiation to investigate the relationship between cell-to-cell interactions and their population sizes.

The mathematical model can reproduce experimentally observed time courses of cell population size. We can also infer a regulatory network of thymocytes and TECs from the model, and reveal its role for the homeostasis of thymic cell populations. We find that DN

thymocytes and cTECs form a negative feedback loop, which results in the overshooting dynamics of population sizes thereof. We further analyze the detail differentiation process of DN thymocytes because the DN stage is subdivided into DN1, DN2, DN3, and DN4 stages in the order of differentiation, and they interact with cTECs in different ways. We modify the model to include more detailed differentiation stages from DN1 to DN4. The detailed model reproduces the dynamics of subpopulations of DN1 to DN4. We also obtain the DN population dynamics almost the same as the proposed model by summing up DN subpopulations of the detailed model. The detail model indicates that the influx of thymocyte progenitors is quite small, which agrees well with other estimates.

In addition, we observe that the recovery of DP thymocytes is much faster than that of DN thymocytes. Our model predicts that DP thymocytes accelerate their recovery of population size by proliferating temporally upon the decrease in its population size. A subsequent experiment of proliferation assay verifies this prediction by showing that the proportion of proliferating DP thymocytes gets higher temporarily after irradiation. We also demonstrate that the model of SP4 thymocytes and mTECs can mimics the previous study which impaired interaction between them.

Our model establishes a pivotal step towards the integrative understanding of T cell development as a regulatory network system. We anticipate a future extension of our model by incorporating the dynamics of other thymic resident cells, such as B cells, dendritic cells, and thymic endothelial cells, to understand thymic development and its homeostasis more comprehensively.

Although the mathematical model for population dynamics in the thymus revealed the contribution of intercellular interactions to homeostasis of thymic populations size, it remains unclear how the TCR repertoire diversity, the quality of T cell population, is maintained against perturbation. Therefore, we next investigate the dynamics of the TCR repertoire change by thymic selection in which thymocytes with inappropriate TCRs are weeded out via interactions with TECs. We perform deep sequencing of TCR α and β chains from matured DP and SP4 thymocytes during the recovery from irradiation to measure the effect of negative selection, an elimination of self-reactive TCRs, and its temporal disorder by irradiation. TCR repertoire analysis clarifies that the repertoires of α and β chains are temporally impaired by irradiation in different ways.

In the normal TCR α chain repertoire before irradiation, we find that unique α derived from invariant natural killer T cells (iNKT cells) becomes significantly abundant in SP4 thymocytes. However, irradiation curtailed the abundance of the unique α chain. We also observe that the recovery of the unique α chain abundance is much slower than that of the other α chains. This slower recovery suggests that the iNKT-like fraction undergoes different differentiation process from other thymic T cells.

We also characterize the difference of TCR β chain repertoire by the usage of V and J genes, which code variable regions of TCR chains. We find that linear transformations of V and J gene usage counts quantify the effect of negative selection and irradiation. Furthermore, we also find that the effect of both negative selection and irradiation are correlated more with V genes than with J genes. This correlation of the irradiation effect with V genes suggests that the TCR, especially its V gene, may contribute to the thymocyte ability to survive and proliferate after irradiation. We next investigate how the proportion of common CDR3 sequences, one of the variable regions of the TCR, changes after irradiation. We find that the proportion of several CDR3s gets higher after irradiation. This also supports the prediction of TCR-dependent radiation tolerance, because thymocytes of small population size under normal conditions would not get abundant by irradiation if every clone is equally eliminated by irradiation

These results can serve as a first step of the forthcoming study of the repertoire time course to dissect the mechanism of thymic selection and the repertoire homeostasis in the thymus.

Finally, we investigated developmental control of thymocytes phenotypes. The phenotype composition of T cells, as well as their TCR repertoire diversity, is also vital for appropriate immune reaction. The lineage choice of thymocytes in the thymus is the first step that shapes various phenotypes of T cells. Despite the exploration of numerous molecules that engage in the lineage choice, it remains unclear how those molecules as a whole process multiple extracellular signals for appropriate differentiation.

To address this problem, we construct a mathematical model of intracellular signaling during thymocyte differentiation. In particular, we focus on a homeostatic property of differentiation duration. The mathematical model suggests that incoherent regulations of the TCR signal to the cytokine signal contributes to the constant differentiation duration independently from

TCRs. We expect that our model evokes experimental verification of the model.

Our quantitative studies exploit mathematical modeling and sequence analysis, emerging approaches in immunology, to provide a systematic viewpoint that integrates previous findings on various aspects of T cell development, and deepen understanding of the homeostasis in the thymus. We anticipate that our studies have a pivotal impact on future directions for immunological research from a systematic perspective.

Contents

Chapter 1

Introduction

1.1 Immunological role of T cell

Most of living organisms have immune systems to protect themselves against unwanted biological invasion. The adaptive immune system of vertebrates defends the body against pathogens by pathogen-specific responses. To cope with numerous kinds of pathogens, the adaptive immune system is composed of immune cells with a diverse repertoire of receptors, each of which has different antigen specificity. One of the major types of immune cells is T lymphocyte. Each clone of T cells has a unique T cell receptor (TCR). It is estimated that the number of T cells in a human body is about 2×10^{11} and that the number of possible TCRs is about 10^{15} [49].

TCRs bind with antigens, peptides presented on a histocompatibility complex (MHC) molecule that antigen-presenting cells (APCs) such as dendritic cells (DCs) express on their cell surface [6]. The binding of TCRs with specific antigens induces various immune responses by T cells according to their differentiation status. Major groups of differentiated T cells are helper T cells and cytotoxic T cells. When activated, helper T cells secrete cytokines to control immune response of other cells; cytotoxic T cells induce apoptosis of infected cells or tumor cells. Helper T cells and cytotoxic T cells are characterized by their expression of cell surface markers CD4 and CD8 for each. CD4 and CD8 support TCR to bind with peptides on different types of MHC, class I and class II, respectively.

Disorder of the T cell function leads to severe immune deficiency; attacking reaction to self-antigens result in autoimmune diseases, and unnecessary reaction to harmless antigens may cause allergy. Therefore, it is essential to develop a T cell population with an appropriate TCR repertoire and differentiation states.

1.2 T cell development in the thymus

T cells originate from hematopoietic stem cells that reside in the bone marrow. Hematopoietic stem cells reach the thymus through the circulation of the blood and differentiate from progenitors of T cells, thymocytes, into T cells in the thymus (Fig. 1.1). T cell development in the thymus should be appropriate in terms of its population size, TCR repertoire,

and lineage commitment so that T cells can properly respond to various pathogens in the periphery. We aim to elucidate the homeostasis of each of these aspects in this thesis. In this section, we give a brief overview of a biological process related to each aspect; stepwise differentiation, somatic recombination and thymic selection, and intracellular signaling of lineage choice.

1.2.1 Differentiation process

The differentiation stages of thymocytes are divided into three major stages based on the expression of CD4 and CD8. The first stage is the $CD4^{-}CD8^{-}$ double negative (DN) stage, where thymocytes express neither CD4 nor CD8. DN thymocytes can be further divided into 4 sequentially ordered subpopulations; DN1 ($CD117^{+}CD44^{+}CD25^{-}$), DN2 ($CD117^{+}CD44^{+}CD25^{+}$), DN3 ($CD117^{lo/-}CD44^{-}CD25^{+}$), and DN4 ($CD117^{-}CD44^{-}CD25^{-}$) [14]. DN4 thymocytes proceed to the $CD4^{+}CD8^{+}$ double positive (DP) stage and finally reach the $CD4^{+}CD8^{-}$ or $CD4^{-}CD8^{+}$ single positive (SP) stage. 1-4 $\times 10^{6}$ matured SP thymocytes egress from the thymus via post-capillary venules as naive T cells per day in mice on average [42].

During this differentiation process, thymocytes move around the thymus mutually interacting with the thymic environment; they first reside in the cortex and migrate to the medulla as they differentiate from DP to SP. Among cells that compose the thymic environment, two types of thymic epithelial cells (TECs), cortical TECs (cTECs) and medullary TECs (mTECs) take essential roles for thymocyte development; they control differentiation, migration, TCR repertoire formation, and lineage choice of thymocytes.

1.2.2 Generation of TCR repertoire diversity

Thymocytes start to express TCRs during the differentiation. TCRs are heterodimers consisting of α- and β- chains. The α-chain is composed of variable(V), joining(J), and constant(C) genes, while the β-chain has diversity(D) genes in addition to V, J, and C [63]. The diversity of TCRs is generated by the germline recombination of the gene segments termed V(D)J rearrangement [6] that randomly chooses V, J, and D genes and combines them with

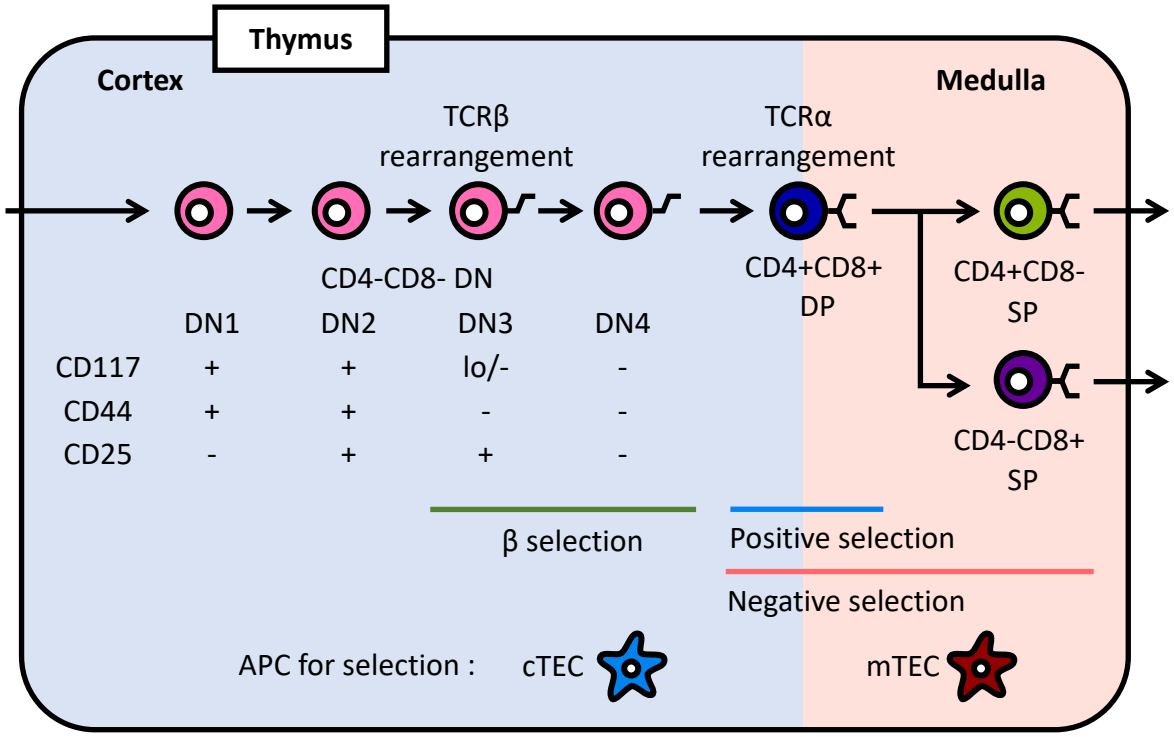

Figure 1.1: Differentiation process of thymocytes.

insertion and deletion of nucleotides to create a gene for the TCR (Fig. 1.2). Murine TCRα locus contains 98 TRAV and 60 TRAJ segments; murine TCRβ locus contains 35 TRBV, 2 TRBD, and 14 TRBJ segments [5, 24]. Each V, D, and J coding segment has conserved DNA sequence elements, termed recombination signal sequences (RSSs), adjacent to both ends of its coding segment. The V(D)J recombinase, a complex of RAG1 and RAG2 (recombination activating gene 1 and 2), recognizes RSSs to cleave and joint V(D)J segments [64]. Formation of a hairpin coding end by sealing the end of DNA double-strands follows the DNA cleavage between RSSs and coding segments. Subsequently, the recombinase opens the hairpin coding end. The position of the opening is often shifted a few bases off-center. This shifted cleavage results in short, single-stranded extensions that can give rise to palindromic insertions (P nucleotides). Then, nontemplated nucleotides (N nucleotides) are added to the single-strand by the enzyme, terminal deoxynucleotidyl transferase (TdT), for the formation of coding joints. During the process of cleavage and sealing, nucleotide deletion may occur.

The resultant α and β chains contain three hypervariable loops in its structure, termed complementarity determining regions (CDR1-3). While CDR1 and CDR2 are required to interact with pMHC, and encoded by V genes, CDR3 directly contacts with a peptide of pMHC and thus takes an vital role for peptide recognition [63]. The insertion and deletion

of DNA fragments during the rearrangement contributes to the diversity of CDR3 region more than the combinatorial variation of V(D)J genes.

The V(D)J rearrangement takes place during the differentiation of thymocytes [78]. In the DN3 stage, thymocytes first rearrange their TCRβ locus, and form a pre-TCR by combining TCRβ and pre-TCRα chains. Lack of a pre-TCR signal due to a failure of the TCRβ rearrangement leads to apoptosis of thymocytes. This selection process is called β-selection [10]. pre-TCRs had been thought to transmit the signal without binding with pMHC. However, they were recently reported actually to bind to pMHC [50]. Thymocytes that passed the β-selection further rearrange their TCRα locus during their differentiation from DN4 to DP.

DP thymocytes again encounter the presentation of self-peptide by cTECs. DP thymocytes can differentiate to the SP stage only if their TCRs have sufficient affinity to the self-peptides; otherwise they end up in apoptosis. This process is referred to positive selection and ensures that T cells can receive antigen presentation in the periphery. On the other hand, thymocytes that express TCRs with high affinity to self-peptides and thus receive a strong signal are also eliminated by apoptosis. This process, in turn, is called negative selection and prevents T cells from attack self-derive cells in the periphery. While only cTECs engage in positive selection, both cTECs and mTECs engage in negative selection and negative selection lasts through the SP stage. Thymocytes that passed positive selection and negative selection forms appropriate diversity of TCRs that only respond to foreign antigens.

1.2.3 Lineage choice between $CD4^+$ and $CD8^+$ T cells

After the V(D)J recombination, every thymocyte chooses to express either CD4 or CD8 as they differentiate from DP to SP. The mechanism how they choose their lineage is best explained by the kinetic signaling model [73] as follows. The TCR signal first leads all DP thymocytes to terminate CD8 expression and convert into $CD4^+CD8^{low}$. Thymocytes with the lasting TCR signal eventually differentiate to $CD4^+$ SP. On the other hand, if the TCR can recognize antigen presentation only with CD8, the TCR signal gets weak as CD8 ceases to exist on the cell surface. This cessation of the TCR signal allows an interleukin-7 (IL-7)-mediated signal to induce re-expression of CD8 and also to inhibit expression of CD4,

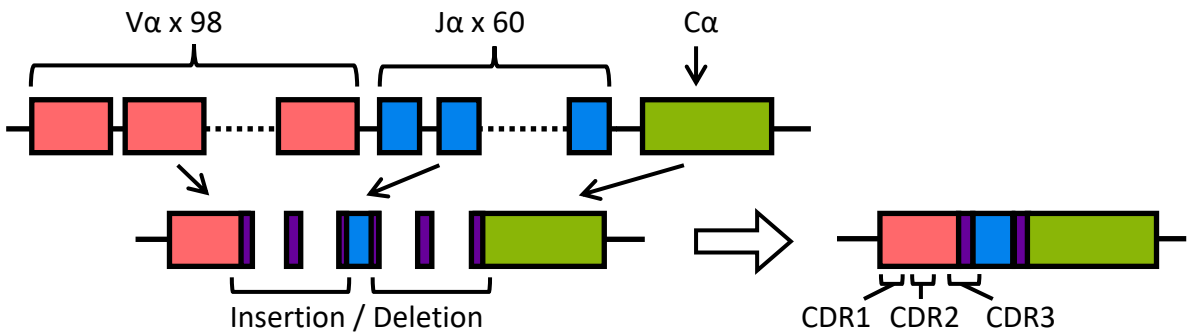

(a)

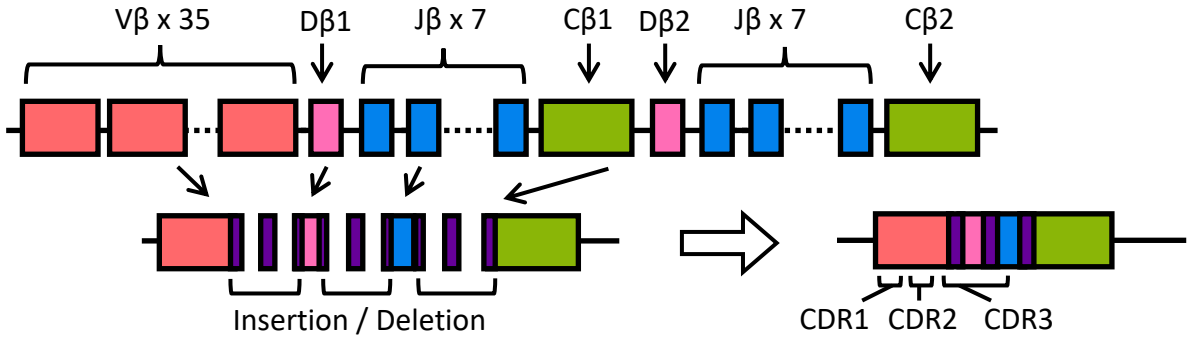

(b)

Figure 1.2: V(D)J rearrangement of (a) α and (b) β chains.

and eventually, thymocytes differentiate to $CD8^{+}$SP. This switch-like expression of CD4 and CD8 is achieved by antagonistic cross-regulation between ThPOK (T helper inducing POZ/Krueppel-like factor) and Runx3 (runt-related transcription factor 3), transcription factors of CD4 and CD8, respectively; ThPOK represses Runx3 and CD8 expression whereas Runx3 limits ThPOK and CD4 expression [32].

The fundamental relationship between ThPOK and Runx3 is regulated by extracellular signals and a large number of downstream molecules Fig. 1.3. The initial TCR signal upregulates ThPOK through c-Myb and GATA3, and ThPOK and GATA3 form positive feedback [23, 85]. While ThPOK represses CD8 by directly binding to the CD8 locus [65], it limits Runx3 expression more indirectly through Socs1 (Suppressor of cytokine signaling 1) upregulation [48]. Runx3 is induced by the IL-7 signal through Jak1 and Jak3 (Janus kinase 1 and 3), and their downstream pSTAT5 (phosphorylated signal transducer and activator of transcription 5) [35], and Socs1 blocks the IL-7 signaling [13]. The TCR signal has other pathways that block Runx3; upregulation of miR-17 (microRNA-17) that blocks Jak1 translation [35], and Caplain that dissociate Jak3 from IL-7R [59]. On the other hand, the TCR

signal also induces the IL-7R (IL-7 receptor) expression and inhibits Socs1 during cessation of the CD8 expression [60], and the IL-7 signal upregulates CD8 through Runx3 as the TCR signal stops for the CD8 lineage.

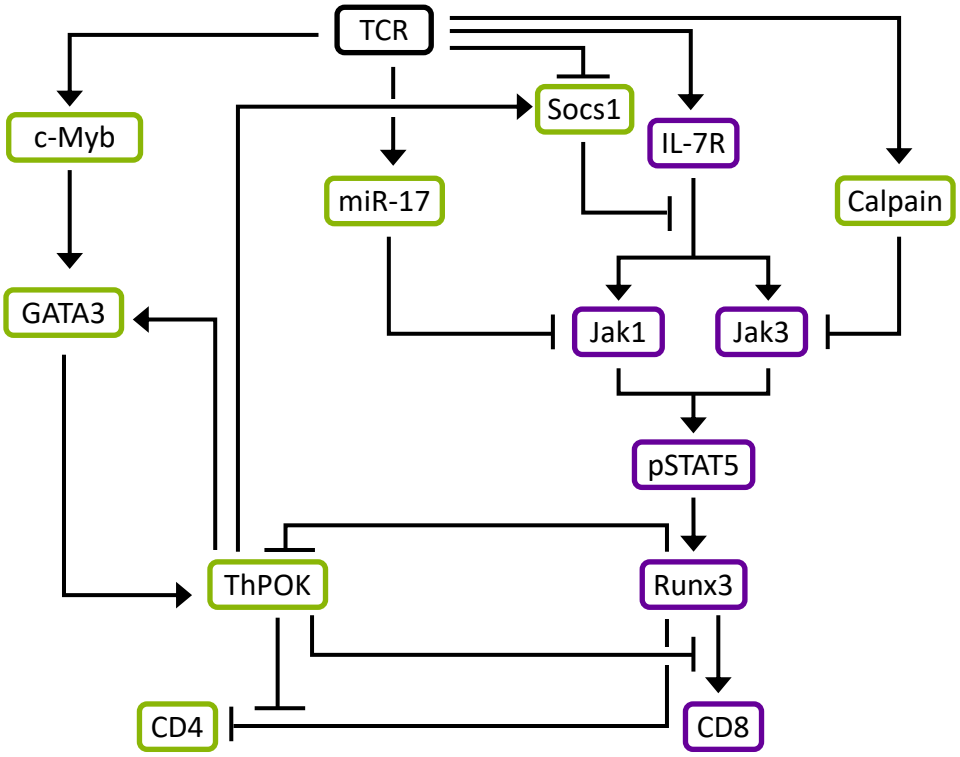

Figure 1.3: Signaling network of thymocyte lineage choice to $CD4^+$or $CD8^+$SP cell. Molecules with light green border induce CD4 expression, and those with purple border induce CD8 expression. The arrows and the lines with the T-shaped head represent positive and negative interaction between molecules, respectively.

1.3 Outline of thesis

T cells play crucial roles in the immune system to recognize pathogens and control the immune response. The immune system maintains an enormous amount of T cells with appropriate TCR diversity and phenotypic composition to deal with various pathogens. Therefore, the homeostasis of T cell development for its population size, TCR repertoire, and lineage commitment is fundamental to the immune system (Fig. 1.4). To unveil the mechanisms of these aspects of homeostasis, a quantitative approach employing mathematics and informatics is advantageous. In this thesis, we study this homeostatic T cell development

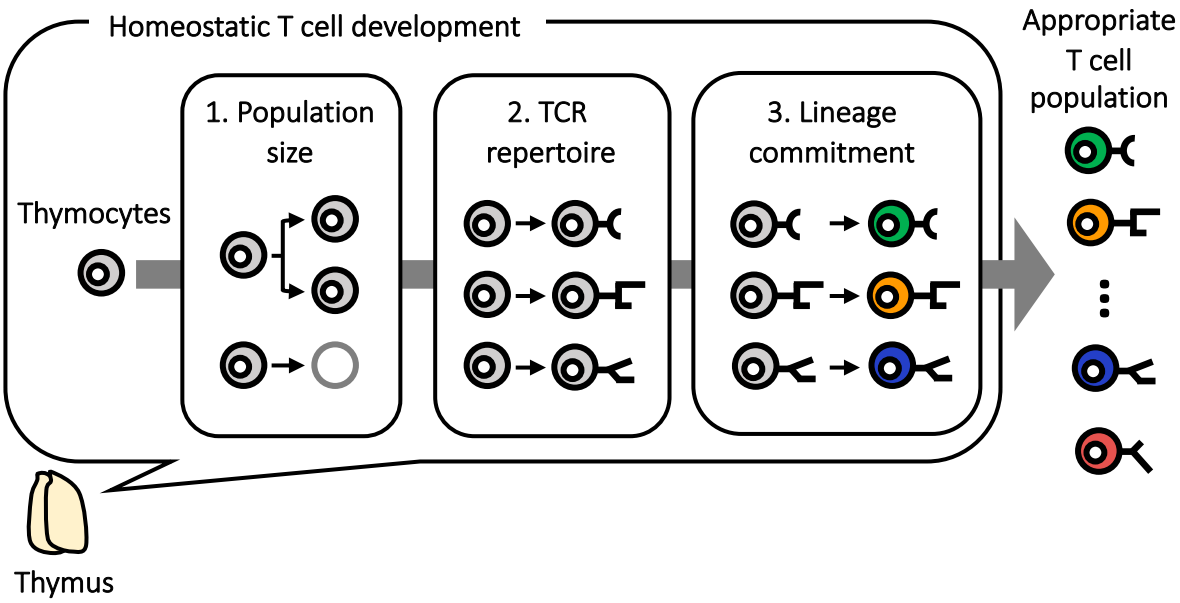

Figure 1.4: Overview of research topics in this thesis.

by utilizing mathematical modeling and high throughput sequence analysis.

We first construct a mathematical model of population dynamics in the thymus that reproduces experimentally observed population change during the recovery from irradiation(Chapter 2). We compare models that assume different intercellular interactions, and identify the most probable interactions that contribute to the homeostasis of thymic cell populations. The most probable model predicts, and the subsequent experiment verifies that DP thymocytes temporarily increase their proliferation rate to compensate for a reduction in population size. Results presented in Chapter 2 are taken from the publication [34] by the author of this thesis. We next investigate how thymic selection of the TCR repertoire gets affected by irradiation using high throughput sequence analysis (Chapter 3). We compare V and J genes usage and CDR3 frequencies in TCR α and β chains during the recovery from irradiation. We find multiple indices that quantify repertoire change by the thymic selection and its damage by irradiation. We then work on mathematical modeling of intracellular signaling during lineage commitment from DP to $CD8^+SP$ (Chapter 4). From the derived model, we infer a mechanism that thymocytes differentiate for a constant time independently from their TCRs. Finally, we summarize these results and discuss future prospects (Chapter 5).

Chapter 2

Quantitative analysis reveals reciprocal regulations underlying recovery dynamics of thymocytes and thymic environment in mice

2.1 Introduction

The thymus is an organ responsible for producing a large part of T cells with appropriate repertoires [78]. However, it is relatively sensitive to insults from stress, viral infection, radiation, and other stimuli [4, 28]. While a thymus in a healthy animal can be normally recovered from these damages, a relatively prolonged process of thymic recovery may impair T cell-mediated immunity due to a reduced replenishment of naïve T cell repertoire during the recovery period [28, 61].

Sub-lethal dose radiation on mice has been utilized as an experimental model of the thymic regeneration after insults [17, 75]. Ionizing irradiation is also broadly used for hematopoietic transplantation and cancer therapy [8, 53], and total body irradiation causes acute thymic injury and slow recovery of thymopoiesis. Several studies have shown that irradiation reduces cellularity, not only of thymocytes but also of thymic epithelial cells (TECs), which are major constituents of the thymic environment [17, 18, 88]. Because thymopoiesis is supported by interactions between thymocytes and TECs [1], understanding thymic recovery requires characterization of the reciprocal regulations between thymocytes and TECs.

Concomitantly, various techniques to trace, perturb, and quantify cells involved in these events have enabled us to quantitatively characterize their dynamics [19, 41, 76, 94]. By combining mathematical models with such quantitative data, dynamic aspects of thymopoiesis have been distilled into the form of detailed kinetic information, e.g., rates of proliferation, death, and differentiation [41, 90]. Mehr *et al.* [55] developed the first kinetic model of thymocyte development using ordinary differential equations [9]. Since this seminal work, kinetic models of the thymopoiesis have been progressively refined by considering detailed cellularity and developmental states of the thymocytes, as well as by incorporating different experimental conditions [3, 51, 69, 72, 80].

However, previous works have focused only on thymocytes. Thymic development and thymic recovery are not thymocyte-autonomous but rather are supported by the thymic environment. In the last decade, we have accumulated molecular-biological evidence that the thymic environment itself is homeostatically maintained by thymic crosstalk, bidirectional interactions between the thymocytes and the thymic environment [1, 27, 79]. Among several cells

comprising the thymic environment, cortical and medullary thymic epithelial cells (cTECs and mTECs) play integral roles in inducing and controlling proliferation, apoptosis, and lineage commitments of thymocytes [1, 15, 22, 38, 39, 89]. Thymocytes also regulate TECs by modulating their maturation and proliferations [17, 40, 46, 87]. Despite the evident relevance and importance of thymic crosstalk for the thymopoiesis and the thymic recovery, kinetic aspects of the reciprocal regulations between the thymocytes and the TECs have not yet been clarified.

In this work, we investigate the joint dynamics of thymocytes and TECs by combining a mathematical model with a quantitative measurement of the number of thymocytes and TECs during recovery after irradiation. Recovery dynamics are reproduced by out mathematical model, in which we identified reciprocal interactions between thymocytes and TECS that are relevant for recovery and consistent with thymic crosstalk. Furthermore, we demonstrate that the model provides an explanation for the mechanism of the dynamical change in population size. Particularly, our model predicts, and a subsequent experiment verifies, a previously unrecognized regulation of $CD4^+CD8^+$ double positive (DP) thymocytes which temporarily increases their proliferation rate upon the decrease in their population size.

2.2 Result

2.2.1 Quantification of recovery dynamics of thymocytes and TECs

To quantitatively investigate the kinetic relationship between thymocytes and TECs as well as the establishment of thymic recovery, we artificially perturbed populations of thymocytes and TECs in thymi by using sub-lethal 4.5 Gy irradiation, and measured the dynamic changes in their population sizes over three weeks following irradiation(Fig. 2.1a). Fig. 2.1b summarizes the changes in cell numbers, which were sorted based on conventional markers of thymocytes (Figs. 2.1c and 2.2a) and TECs (Figs. 2.1d and 2.2b). Fig. 2.1b shows that all types of investigated thymocytes and TECs decreased exponentially at different rates immediately after the irradiation. Then, both thymocytes and TECs started recovering within 10 days at the longest; the $CD4^-CD8^-$ double negative (DN) thymocytes and the cTECs began recovery within 5 days whereas the $CD4^+CD8^-$ single positive (SP) thymocytes

and the mTECs required longer intervals, reflecting the temporal order of the thymocyte development from DN to CD4$^+$ SP (SP4) cells through interactions from cTECs to mTECs.

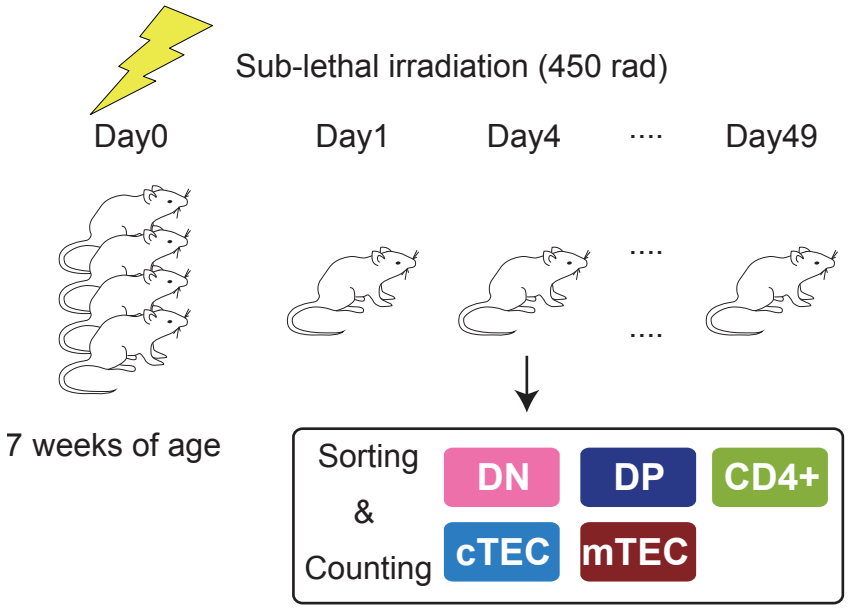

(a)

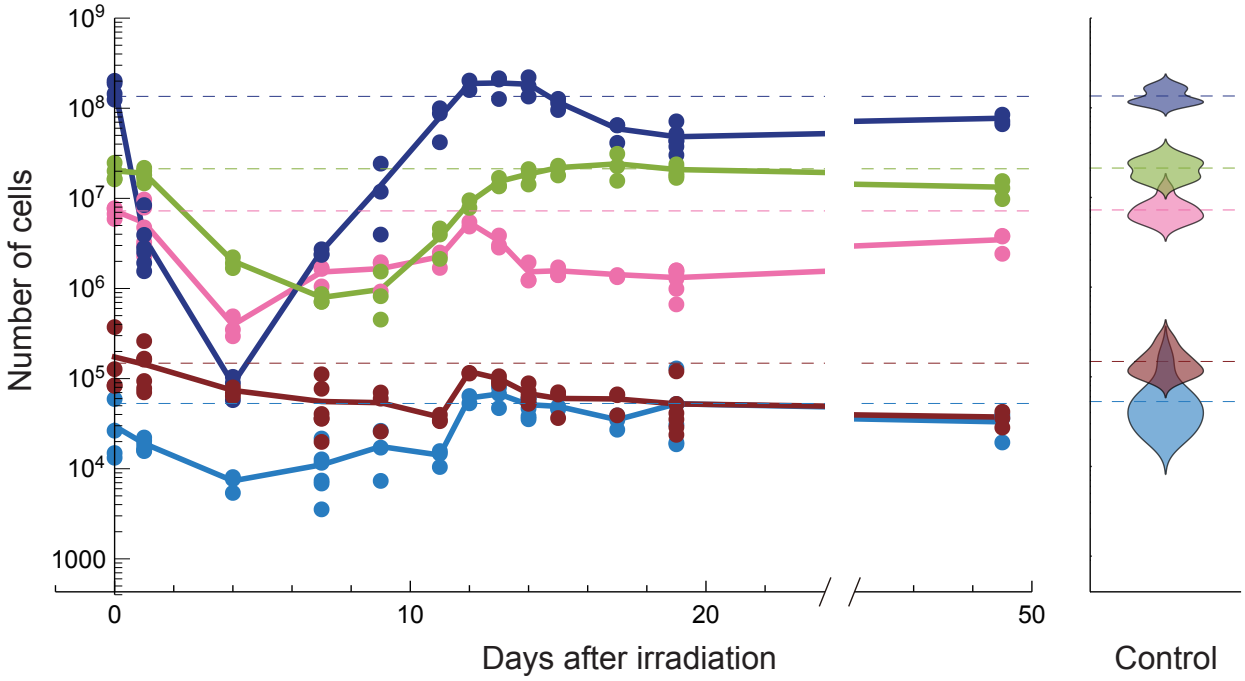

(b)

Figure 2.1: (Continued on the following page.)

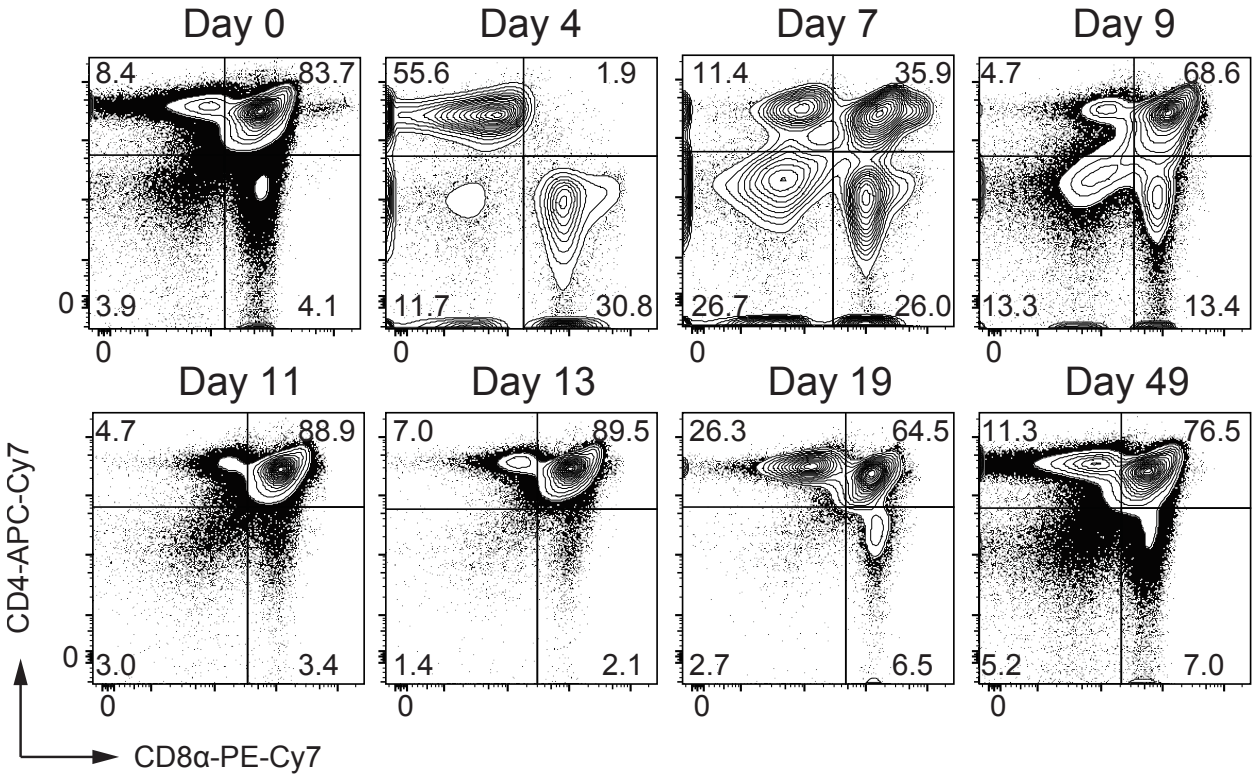

(c)

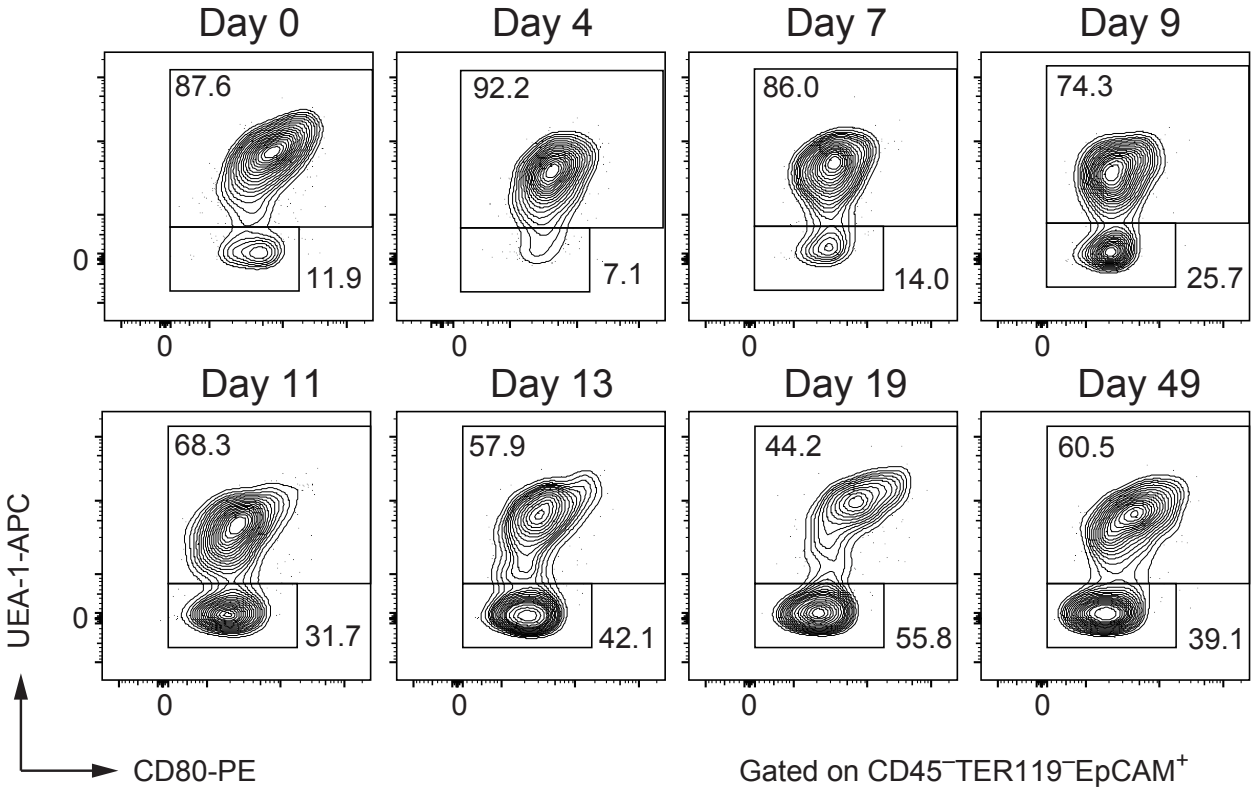

(d)

Figure 2.1: (Continued on the following page.)

Figure 2.1: Recovery dynamics of thymocytes and TECs after sub-lethal irradiation. (a) A schematic diagram of the perturbation experiment. (b) The left panel shows trajectories of the counts of thymocytes (DN: pink, DP: blue, SP4: light green) and TECs (cTEC: cyan, mTEC: brown) after irradiation. Points correspond to the experimental cell counts, and the solid curves are linear interpolations of the average counts at each time point. The numbers of samples at each time point are shown in Table 2.1. The right panel shows violin plots of the numbers of thymocytes and TECs without perturbation. ($n = 15$ for thymocytes, $n = 16$ for TECs) (c) Typical flow cytometric profiles of the thymocytes after the sub-lethal dose radiation. Thymocytes were analyzed by staining with anti-CD4 and anti-CD8α. Percentage of each fraction is shown in the panels. (d) Typical flow cytometric profiles of TECs after the sub-lethal dose radiation. TECs (EpCAM$^+$CD45$^-$TER119$^-$) were analyzed by staining with a combination of UEA-1 lectin and anti-CD80. Percentages of UEA-1$^+$cells (mTECs) and UEA-1$^-$cells (cTECs) are shown in the panels.

Days after irradiation	0	1	4	7	9	11	12	13	14	15	17	19	49
The number of samples (thymocytes)	4	6	3	3	3	3	2	3	3	3	3	6	3
The number of samples (TECs)	4	6	3	6	3	3	2	3	6	3	3	6	3

Table 2.1: The numbers of samples at each time point after irradiation.

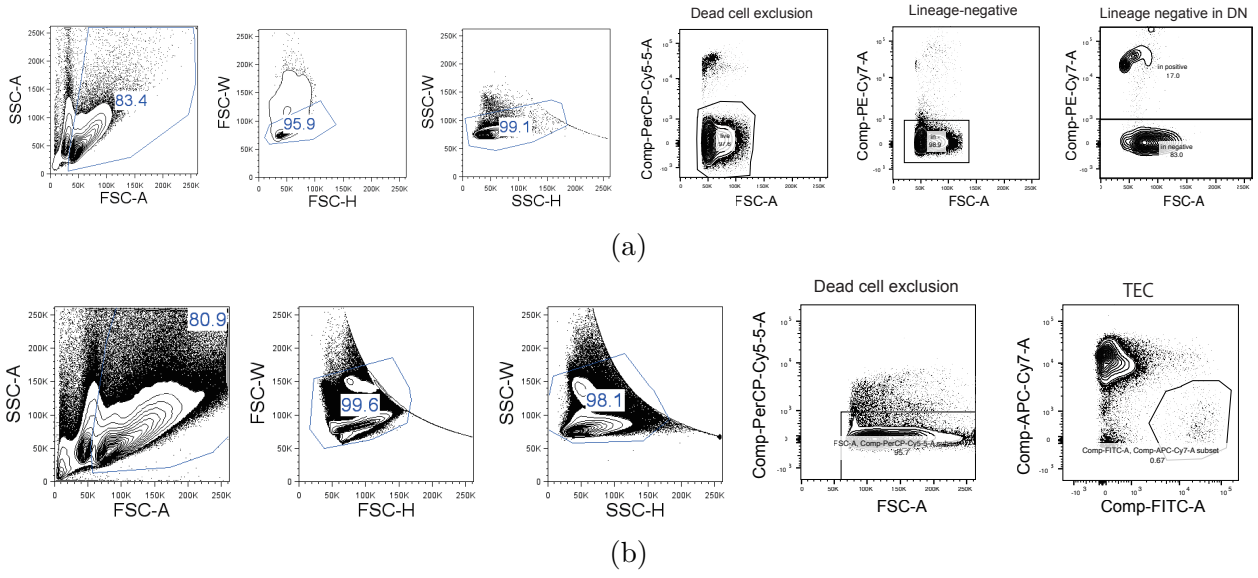

Figure 2.2: (a) Gating strategy for thymocytes. (b) Gating strategy for TECs.

Upon recovery, the population sizes of all but the SP cells peaked around 15 days, and eventually returned to stationary numbers, which are almost equivalent to or at least half of the original population sizes before irradiation. Such overshooting behaviors suggest that the numbers of thymocytes and TECs are dynamically and mutual regulated via reciprocal interactions.

2.2.2 Mathematical model can reproduce recovery dynamics

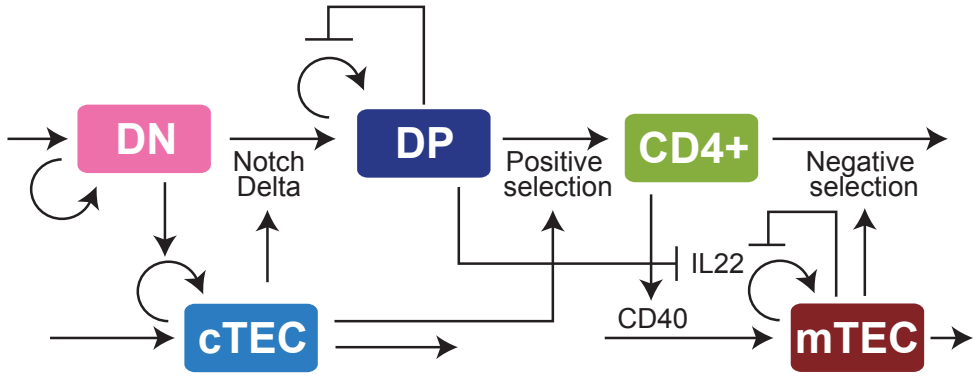

(a)

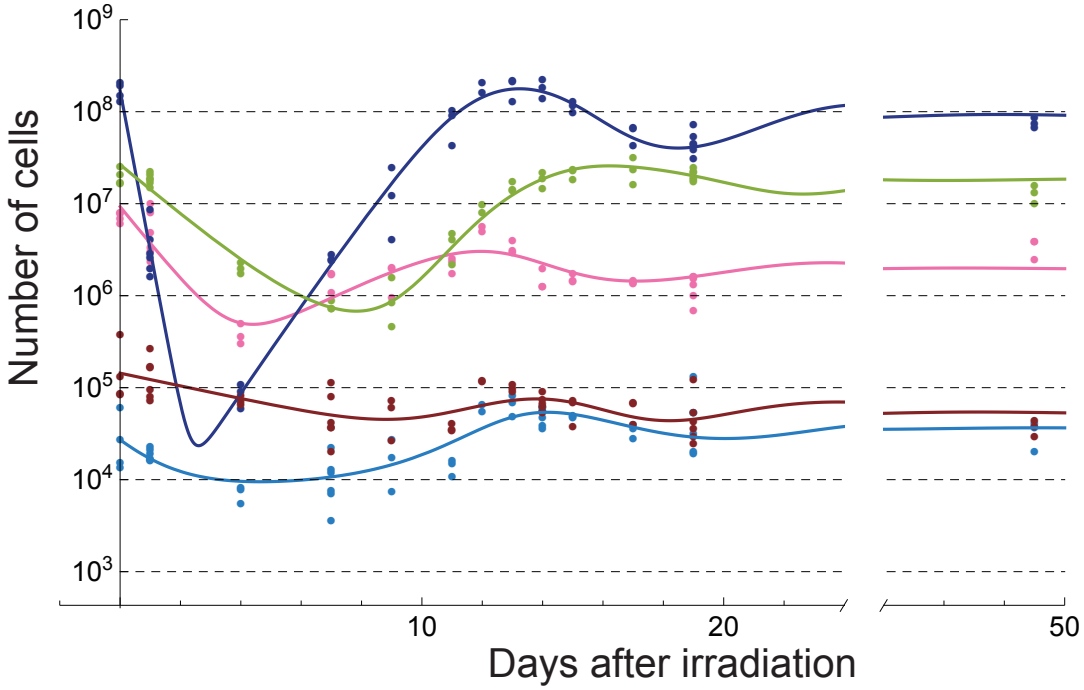

(b)

Figure 2.3: (Continued on the following page.)

To infer regulatory interactions behind the dynamics, we constructed a mathematical model for the population dynamics of the thymocytes and the TECs using ordinary differential equations, which explicitly include five cell types: $i \in C := \{\mathrm{DN}, \mathrm{DP}, \mathrm{SP4}, \mathrm{cTEC}, \mathrm{mTEC}\}$. To account for the acute influence of irradiation on the cells, the total number of the cell type i at time t (day), $n_i^{\mathrm{tot}}(t)$ is decomposed into two parts; $n_i^{\mathrm{x}}(t)$ represents exponentially dying cells by the irradiation and $n_i(t)$, represents cells that survived or were newly generated after irradiation. $n_i^{\mathrm{x}}(t)$ is assumed to decrease exponentially at a constant rate, ω_i (day^{-1}),

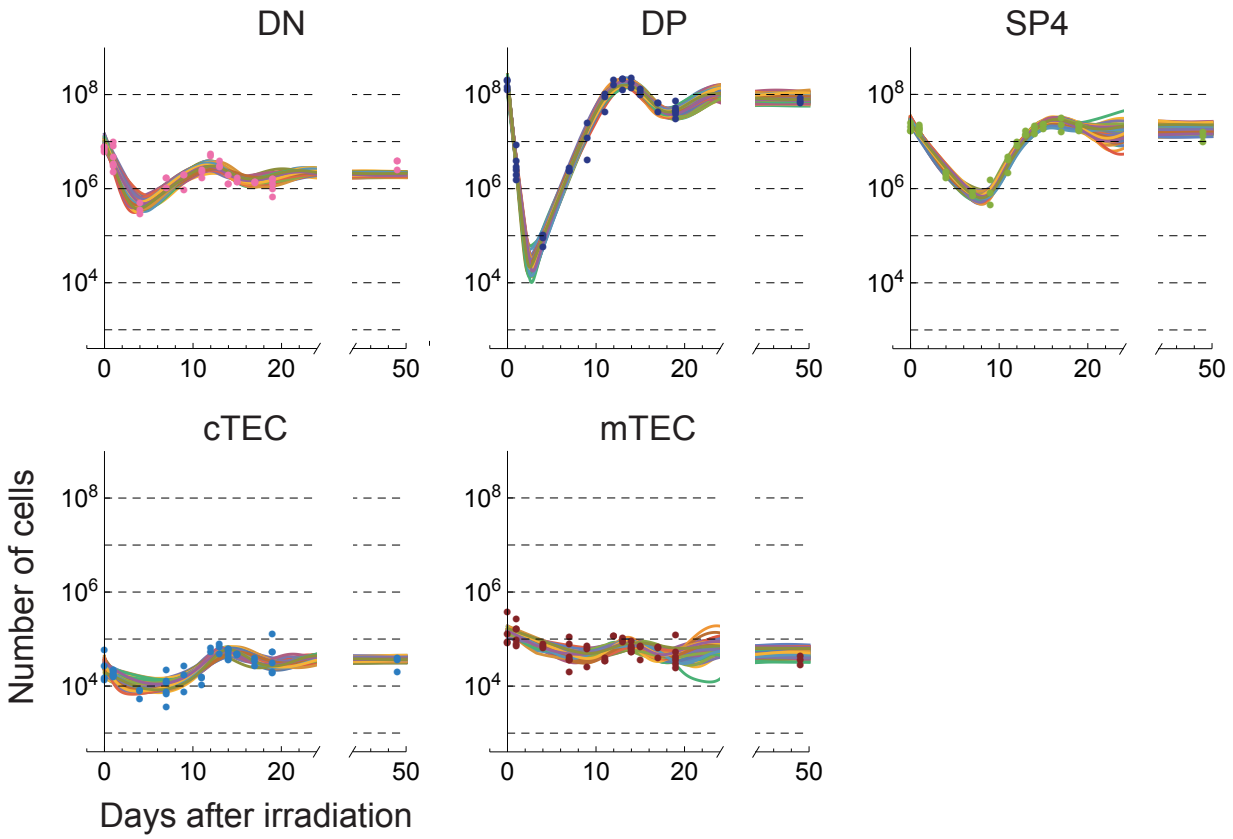

(c)

Figure 2.3: Schematic diagram and trajectories of the mathematical model inferred from the quantitative data. (a) A schematic diagram of the intercellular interactions inferred from the experimental data and represented by Eq.(2.2). (b) Trajectories of the numbers of thymocytes and TECs obtained by simulating Eq.(2.2) with the optimally fitted parameter set. The curves represent simulated trajectories, and the points represent the same experimental data as Fig. 2.1b. Cell types are designated by the color codes which are defined in (a). (c) Trajectories obtained by the bootstrap parameter estimation. Trajectories in different panels with the same color correspond to a simulation with a parameter set estimated from a bootstrapped sample. The trajectories of 100 randomly selected samples are shown in the panels. The points represent the same experimental data as Fig. 2.1b.

as $n_i^{\mathrm{x}}(t) = n_i^{\mathrm{tot}}(0)(1-p_i)e^{-\omega_i t}$ where p_i is the proportion of survived cells after irradiation; we modelled the dynamics of $n_i(t)$ with ordinary differential equations. Therefore, the total number of the cell type i, n_i^{tot}, which we observed experimentally, is described as $n_i^{\mathrm{tot}}(t) = n_i^{\mathrm{x}}(t) + n_i(t)$.

The temporal change in $n_i(t)$ is driven by the imbalance among influx, proliferation, death, and outflux of the type i cells, each of which depends on the number of other cells $\mathbf{n}(t) := [n_{\mathrm{DN}}(t), n_{\mathrm{DP}}(t), n_{\mathrm{SP4}}(t), n_{\mathrm{cTEC}}(t), n_{\mathrm{mTEC}}(t)]^T$, where T denotes transpose. While the influx may be independent of the number of the type i cells, the other should, in nature, depend on

the number of existing type i cells, $n_i(t)$. This allows us to generally represent the ordinary differential equations for $n_i(t)$ as

$$\frac{\mathrm{d}n_i(t))}{\mathrm{d}t} = \phi_i(\mathbf{n}(t)) + f_i(\mathbf{n}(t))n_i(t), \tag{2.1}$$

where the influx should be non-negative, $\phi_i(\mathbf{n}(t)) \geq 0$, whereas the marginalized rate of proliferation, death, and outflux, $f_i(\mathbf{n}(t))$, can be either positive or negative. The actual value of $f_i(\mathbf{n}(t))$ is determined by the balance among proliferation, cell death, and outflux of the type i cells. To obtain a minimal model with minimal complexity, we assume that both $\phi_i(\mathbf{n}(t))$ and $f_i(\mathbf{n}(t))$ are at most linear with respect to $\mathbf{n}(t)$ with possible constant time delays. Therefore, our ordinary differential equation model as a whole has, at most, quadratic nonlinearity. Considering reproducibility of the recovery dynamics after the irradiation and consistency with previously known molecular evidence, we obtained the whole model described as:

$$\begin{aligned}
\frac{\mathrm{d}n_{\mathrm{DN}}(t)}{\mathrm{d}t} &= \phi_1 + (\delta_1 - \mu_1 n_{\mathrm{cTEC}}(t))n_{\mathrm{DN}}(t) \ , \\
\frac{\mathrm{d}n_{\mathrm{DP}}(t)}{\mathrm{d}t} &= r_1\mu_1 n_{\mathrm{cTEC}}(t)n_{\mathrm{DN}}(t) + \left\{\theta_2\left(1 - \frac{n_{\mathrm{DP}}(t)}{K_2}\right) - \mu_2 n_{\mathrm{cTEC}}(t-\tau_2)\right\} n_{\mathrm{DP}}(t) \ , \\
\frac{\mathrm{d}n_{\mathrm{cTEC}}}{\mathrm{d}t} &= \phi_{\mathrm{c}} + (-\delta_c + \mu_c n_{\mathrm{DN}}(t))n_{\mathrm{cTEC}}(t) \ , \\
\frac{\mathrm{d}n_{\mathrm{SP4}}(t)}{\mathrm{d}t} &= r_{24}\mu_2 n_{\mathrm{cTEC}}(t-\tau_2)n_{\mathrm{DP}}(t) - \mu_4 n_{\mathrm{mTEC}}(t)n_{\mathrm{SP4}}(t) \ , \\
\frac{\mathrm{d}n_{\mathrm{mTEC}}(t)}{\mathrm{d}t} &= \phi_{\mathrm{m}} + \phi_{\mathrm{m4}} n_{\mathrm{SP4}}(t) + \left\{r_{\mathrm{m}}\left(1 - \frac{n_{\mathrm{mTEC}}(t)}{K_{\mathrm{m}}}\right) - \gamma_{\mathrm{mp}} n_{\mathrm{DP}}(t-\tau_{\mathrm{m}})\right\} n_{\mathrm{mTEC}}(t) \ ,
\end{aligned} \tag{2.2}$$

a diagrammatic representation of which is shown in Fig. 2.3a. Based on this model with candidate parameter values as the initial condition, we conducted a nonlinear least square estimation of the whole parameter values in Eq. (2.2), $\{n_i^{\mathrm{tot}}(0)\}_{i\in C}$, $\{\omega_i\}_{i\in C}$, and $\{p_i\}_{i\in C}$ so that the whole model can reproduce all the experimental data at once (Fig. 2.3b and Table 2.2). As shown in Fig. 2.3b, our model, Eq.(2.2), nicely reproduced the experimentally observed recovery, demonstrating that the interactions depicted in Fig. 2.3a sufficiently account for the dynamics. Moreover, to reevaluate the importance and statistical confidence of several parameters, we statistically estimated the potential variability of the estimated values by conducting a bootstrap parameter estimation (Figs. 2.3c and 2.4 and Table 2.3). As shown in Fig. 2.4, most parameter values statistically fluctuate around single-peak, whereas

a few parameters, e.g., the influx rate of DN, ϕ_1, have multiple peaks in their estimates.

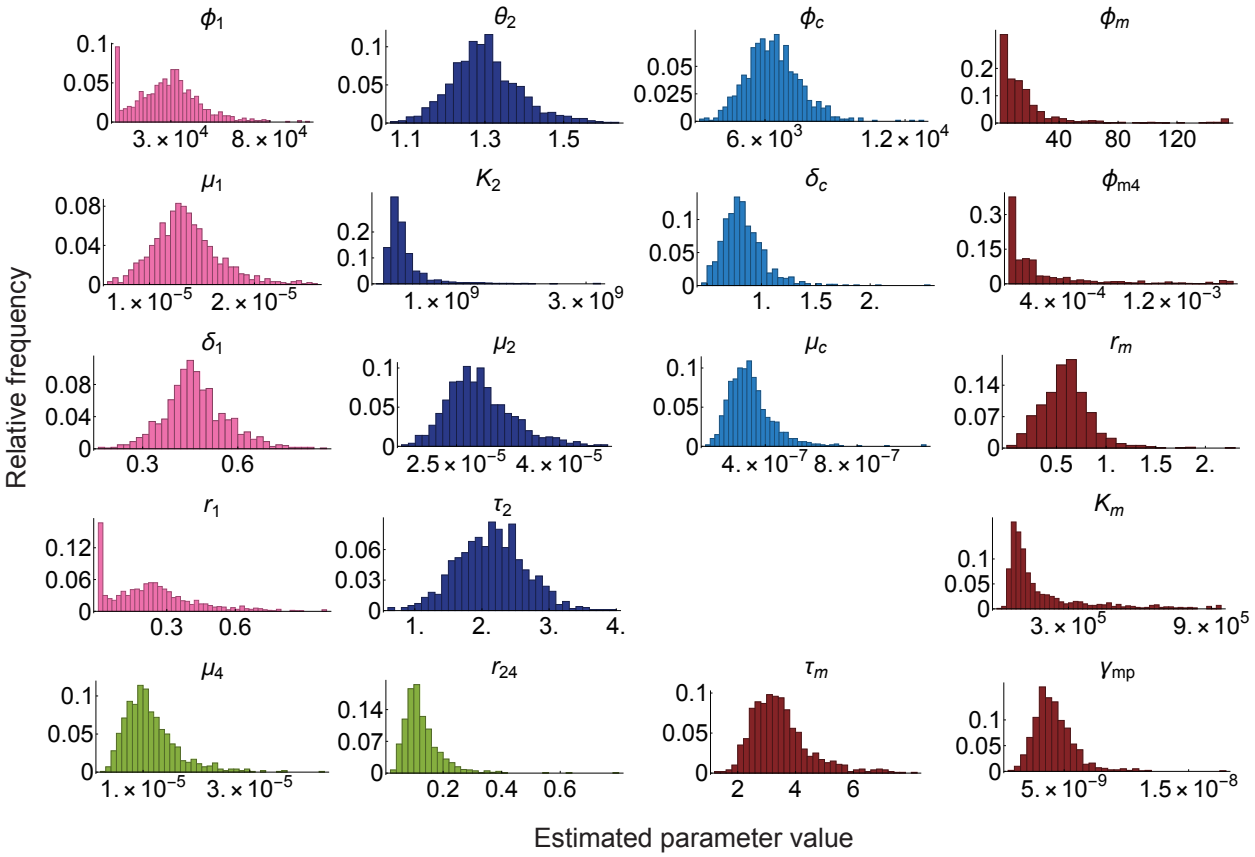

Figure 2.4: Variations of parameters estimated by bootstrap parameter estimation. The color of each histogram of a parameter designates the related cell type in Fig. 2.3a to that parameter. The variations of the other parameters and pairwise scatter plots of the estimated values are also shown in Figs. 2.5 and 2.6, respectively.

2.2.3 DN thymocytes and cTECs form a negative feedback

Our estimated model indicates that DN thymocytes and cTECs form a negative feedback. DN cells marginally work to increase the number of cTECs because μ_c in Eq. (2.2) is positive, whereas cTECs effectively inhibit the increase in DN cells because $-\mu_1$ in Eq. (2.2) is negative(Fig. 2.3a). This negative feedback is the source of the overshooting behaviors in the recovery dynamics, and can account for slower onset of cTECs recovery, which lagged a few days behind DN cells.

These interactions inferred from the quantitative recovery data are also consistent with previously identified molecular evidence. On one hand, the positive interaction from DN thymocytes to cTECs may be interpreted as induction of cTEC proliferation by DN cells,

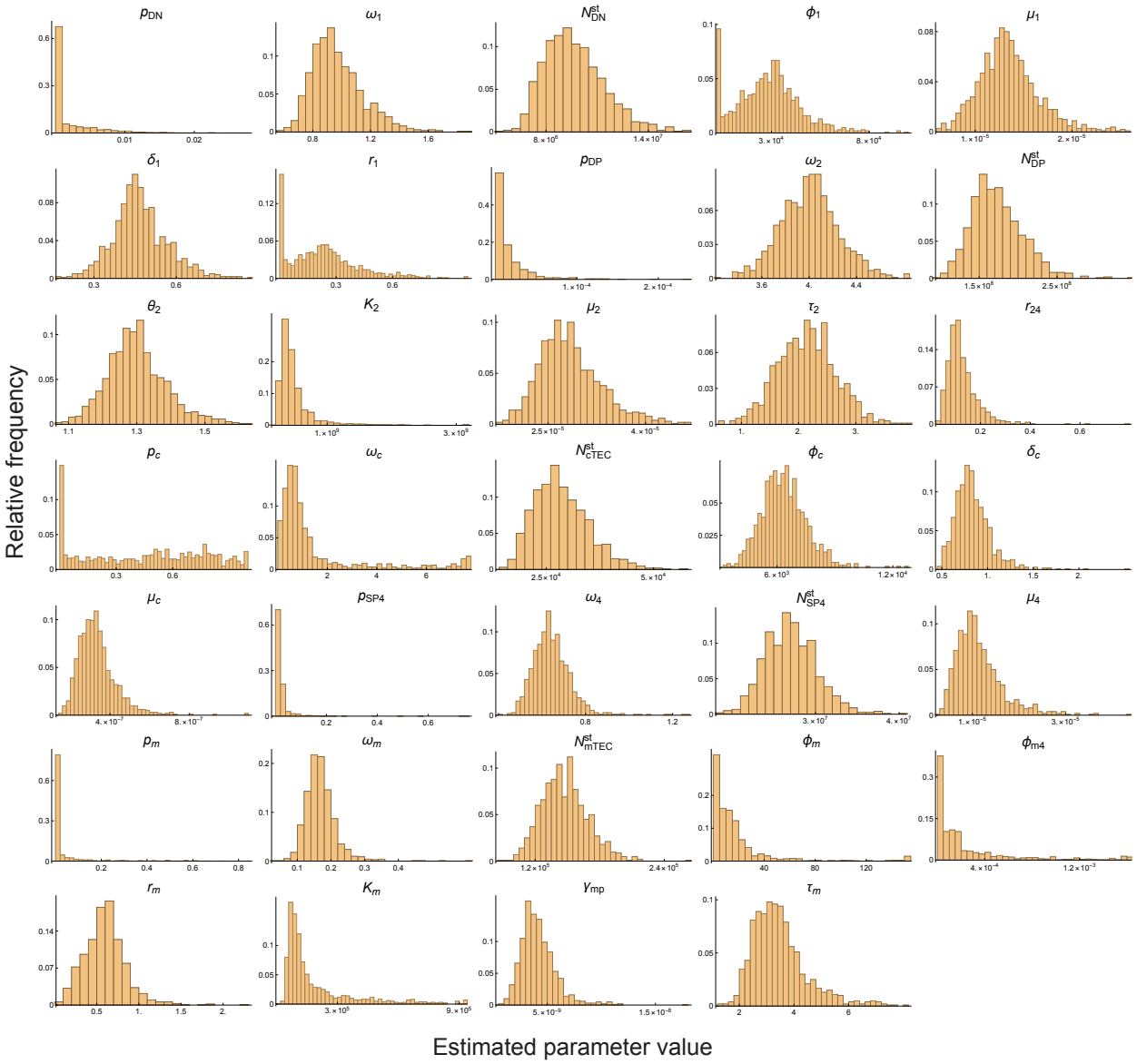

Figure 2.5: Histograms of the parameter values obtained by the bootstrap estimation.

evidenced by the fact that the number of mature cTECs decreases if DN differentiation is blocked at early stages [40, 71]. On the other hand, our model suggests that cTECs work to decrease the number of DN cells. This negative interaction is a marginal effect of induced cell death, induced differentiation from the DN to the DP stages, and inhibition of DN proliferation by cTECs. This negative regulation of DN cells by cTECs is consistent with the lineage commitment of DN cells to the DP stage mediated by cTECs in the Notch1-Delta-like4-dependent manner [22, 89]. It should be noted, however, that our model does not exclude other possibilities of additional molecular interactions as long as their marginal influences are consistent with the diagram in Fig. 2.3a.

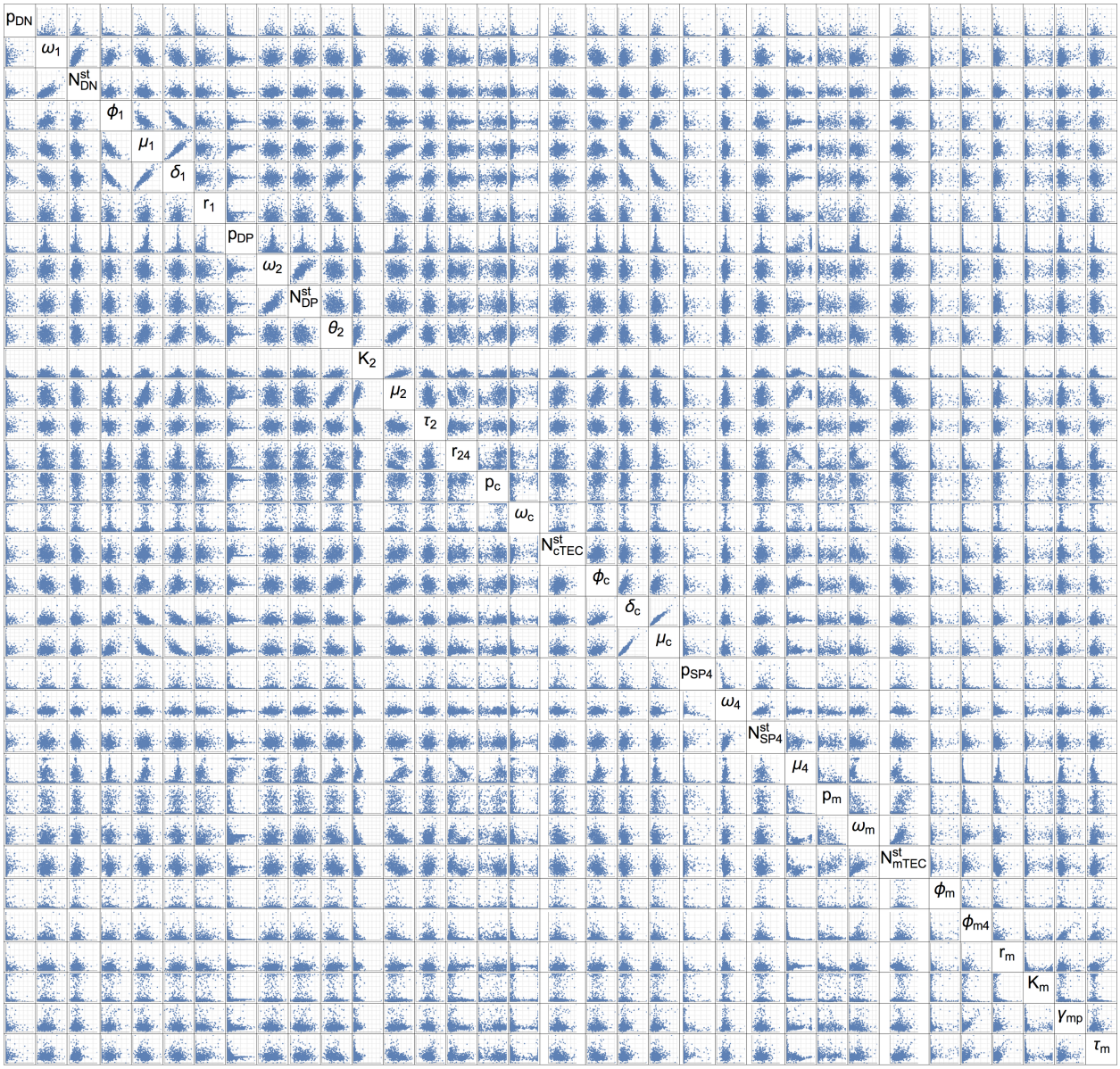

Figure 2.6: Two dimensional scatter plots of the parameter values obtained by the bootstrap estimation. The plot range of each parameter is set to be the same as that in Fig. 2.5.

To further analyze the consistency of our model with the underlying dynamics of DN subpopulations (DN1, DN2, DN3, and, DN4), we additionally quantified the dynamics of these populations after irradiation (Fig. 2.8). We also modified Eq.(2.2) (denoted here as a coarse-grained model) to include DN subpopulations (denoted as a detailed model and shown in Method), the parameter values of which were similarly estimated. As demonstrated in Figs. 2.7a and 2.7b, the detailed model reproduces the dynamics of the DN subpopulations (Fig. 2.7a) with only small deviation from the coarse-grained model in which DN subpopulations are lumped together (Fig. 2.7b). We should mention that our estimates of DN1 and DN2 subpopulations can be overestimates because an additional cell surface marker,

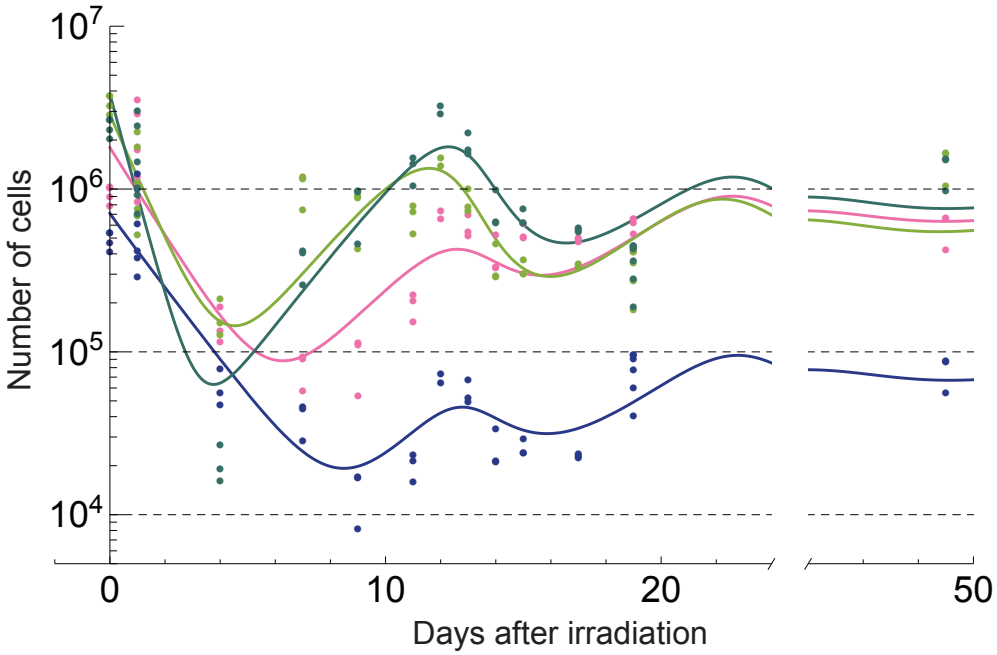

(a)

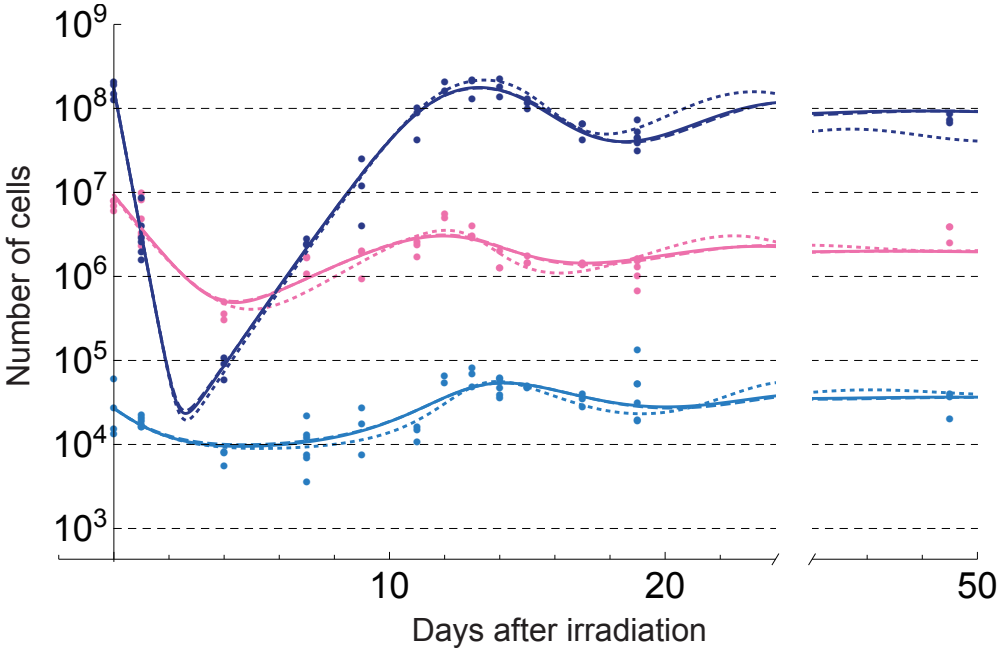

(b)

Figure 2.7: (Continued on the following page.)

CD117, is required to exclude non-T-lineage fractions [11]. This overestimate, however, has little effect on the inferred dynamics of the total DN population (Fig. 2.7b), because the major fraction of DN cells consist of DN3 and DN4 cells. The estimated parameter values were also consistent with those of the coarse-grained model except for the DN1 influx rate ϕ_1 estimate, which was much smaller than that of coarse-grained model. Because the peak other than that around the optimal value in the bootstrap estimate of ϕ_1 was at the lower

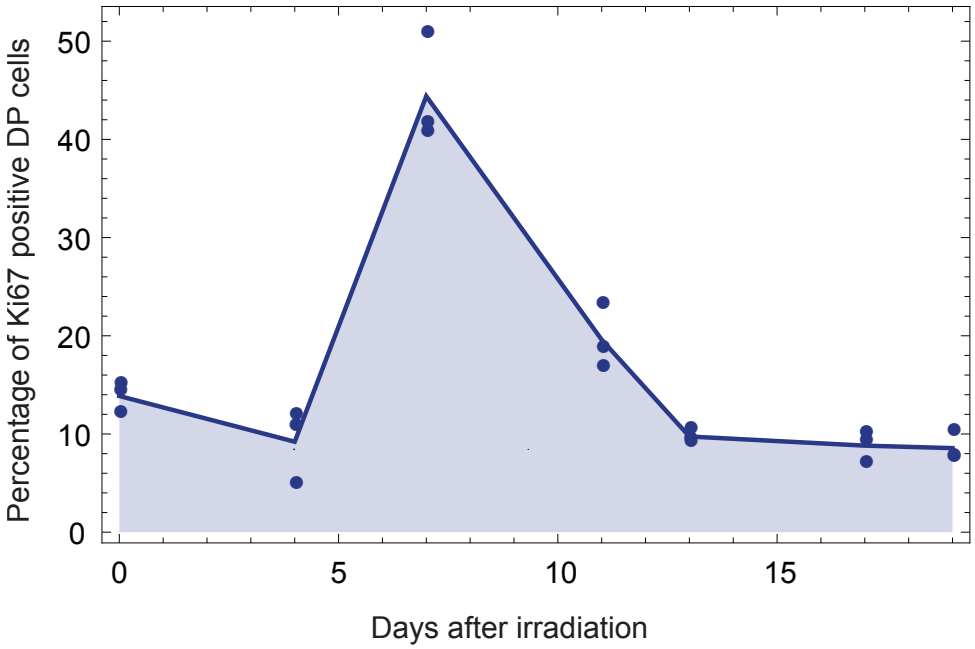

(c)

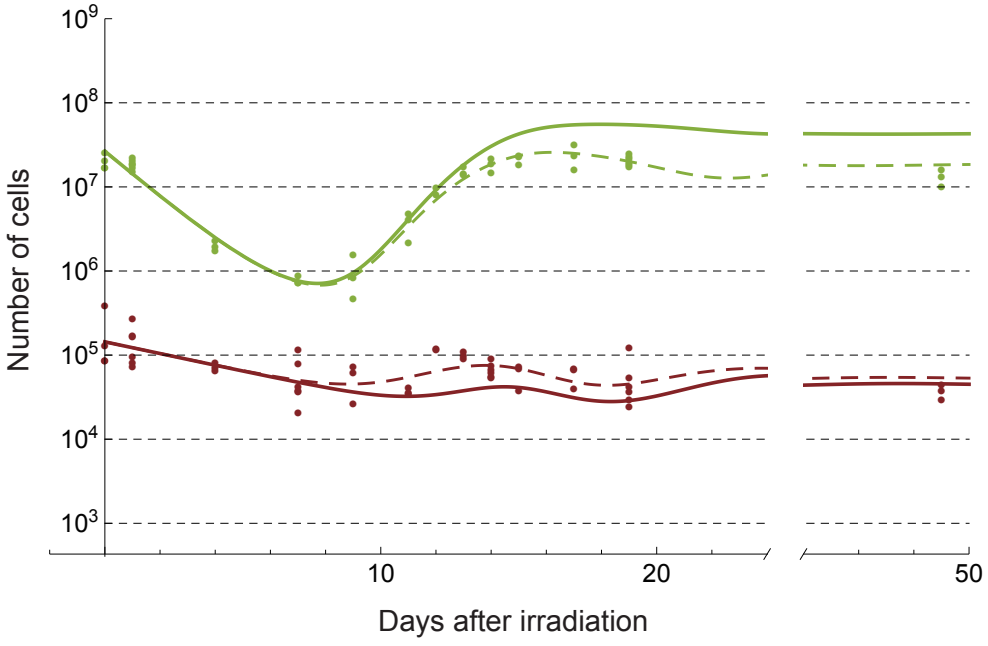

(d)

Figure 2.7: (Continued on the following page.)

bound of its estimation range (Fig. 2.4), a value smaller than the lower bound may also reproduce the same recovery dynamics. To verify whether the estimate of ϕ_1 in the detailed model is also consistent with the coarse-grained model, we simulated coarse-grained model by replacing the value of ϕ_1 in the model with the estimate from the detailed model. As shown in Fig. 2.7b, the trajectories were almost unaffected by this replacement. Moreover, from the biological viewpoint that the number of the influx DN progenitors is quite small [42],

Figure 2.7: Detailed analysis of the proposed mathematical model Eq.(2.2). (a) Dynamics of DN subpopulations obtained experimentally with the corresponding fitted trajectories of the detailed model. DN1 : pink, DN2 : blue, DN3 : light green, DN4 : green. (b) A comparison of the trajectories obtained by the detailed model (dotted line) with those of the coarse-grained model for high (solid line) and low (broken line) DN influx rates. The solid and broken lines are almost perfectly overlapped in this panel. The colors represent cell types; DN : pink, DP : blue, cTEC : cyan. (c) Validation of the model prediction by a proliferation assay of DP cells. Percentages of Ki67 positive DP cells are obtained at 0, 4, 11, 13, 17, and 19 days after irradiation. Points represent experimental cell counts, and shaded lines represent linear interpolations of the average counts. ($n = 3$ at each time point) (d) *In silico* evaluation of the impact from the disturbed crosstalk between SP4 thymocytes (light green) and mTECs (brown). Thick solid curves are simulated trajectories of SP4 thymocytes and mTECs with parameter values mimicking the experimental condition in ref. [87], $\gamma_4 = 5.0 \times 10^{-6}$ and $\phi_{\mathrm{m4}} = 0$. The thin broken curves are those obtained with the optimal parameter values used in Fig. 2.3b for comparison.

this value of ϕ_1 is also reasonable. Altogether, analysis of the detailed model revealed that the smaller value of ϕ_1, which cannot be selected only from the analysis of the coarse-grained model, is more relevant.

2.2.4 DP recovery by temporal increase in proliferation rate

The kinetic component characteristic to the DP dynamics is its much faster recovery compared to DN cells (Fig. 2.1b), which strongly suggests that the DP recovery is achieved by self-proliferation rather than by the influx from the DN population. However, evidence about the self-proliferation ability and speed of DP cells is inconsistent may depend on strains [42, 82]; some studies showed that DP cells proliferate little [54, 72] while others have suggested that DP cells can proliferate faster than other types of thymocytes [44, 82]. Our model coordinates these properties with auto-inhibitory regulation of the DP proliferation, represented by the logistic term $\theta_2(1-n_{\mathrm{DP}}(t)/K_2)$ in Eq.(2.2), which can realize fast proliferation during the recovery period and slowdown at the steady state. Nevertheless, such auto-inhibitory regulation in DP proliferation has not yet been reported.

To experimentally verify this prediction by our model, we estimated the fraction of proliferating DP cells under the same condition as in Fig. 2.1a by staining the DP population with proliferation marker Ki67 (Fig. 2.7c). We observed that the fraction of the proliferating DP cells transiently increased and peaked at day 7 after irradiation, coinciding perfectly with

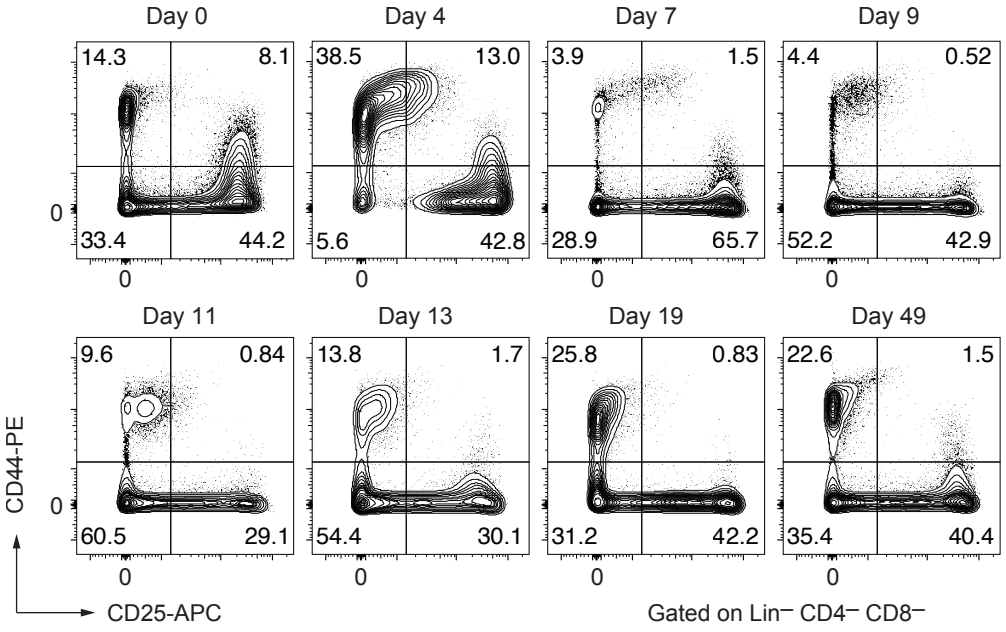

(a)

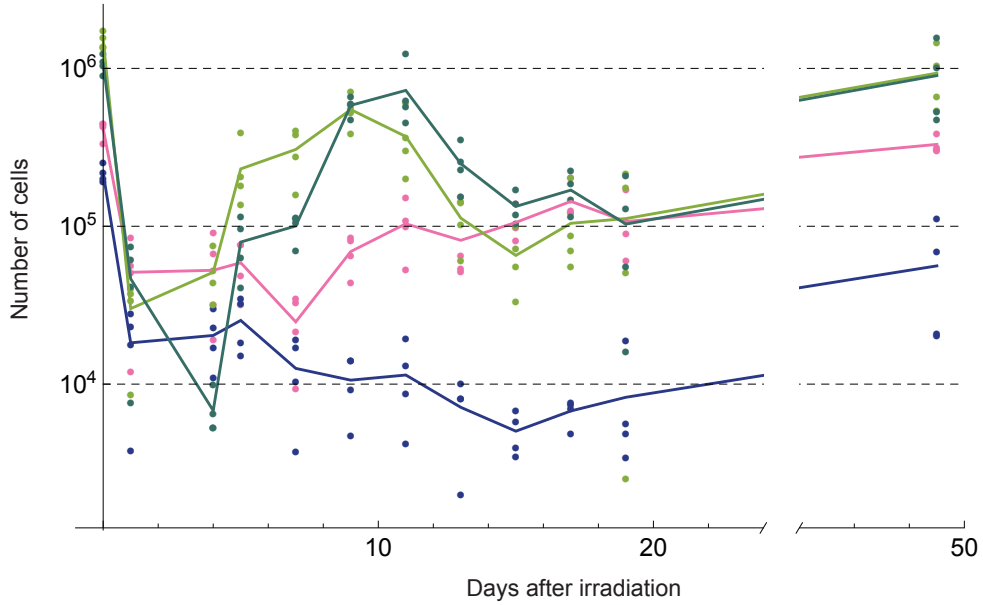

(b)

Figure 2.8: (a) Typical flow cytometric profiles of DN thymocytes after the sub-lethal dose radiation. Lineage marker-negative, CD4-negative, CD8-negative thymocytes were analyzed by staining with anti-CD25 and anti-CD44. Percentage of each fraction is shown in the panels. (b) The trajectories of the counts of the DN1 (pink), DN2 (blue), DN3 (light green), DN4 (green) thymocytes after the irradiation. Points correspond to the experimental counts of the cells, and the solid curves are linear interpolations of the average counts at each time point. (n=4 at each time point)

the timing of exponential increase in DP cells during recovery. Self-proliferation ceased when the number of the DP cells recovered to the normal population size before the irradiation. This result strongly supports that the proliferation rate of DP cells is inhibited by total pop-

ulation size to maintain homeostasis. Further, this autoregulatory mechanism is consistent with the previous observations that the DP cells proliferate little when their numbers are at the steady state [54].

While the autoregulatory proliferation of DP cells is necessary for reproducing fast recovery, it cannot solely account for the overshooting behavior of DP cells, which suggests that other cells regulate DP cells. Supported by the well-established evidence that cTECs engage in positive selection of DP cells, our model includes a negative influence of cTECs to DP cells with a time-delay, which can nicely reproduce the overshoot of DP cell count. This negative interaction with a time delay can be interpreted as the marginal effect of an induced apoptosis of DP cells with non-functional TCRs and the differentiation of DP cells into SP cells upon apoptosis rescue. The existence of the time delay may be interpreted by the sequential and multiple interactions of DP cells with cTECs that are required for positive selection.

Our model estimates that the stable rate of the DP cells to differentiate into CD4 SP cells, $r_{24}\mu_2 n^*_{\mathrm{cTEC}}$ is ranging from 9.1×10^{-2} to 8.4×10^{-1} (day^{-1}), which overlaps the range of the previous estimates from 1.2×10^{-2} to 9.9×10^{-2} (day^{-1}) (Table 2.2).). The estimated value of r_{24} varied from 10% to 75%, which mostly overlaps with the range of the previous estimates that $0.02 \sim 65\%$ of DP cells survive and differentiate into CD4 SP via positive and negative selection (Table 2.2). This coincidence supports interpretation that r_{24} is the fraction of the rescued DP cells that differentiated into CD4 SP and that the remaining fraction $1 - r_{24}$ of the DP cells undergoes apoptosis. However, we should note that an apoptosis rate cannot be estimated directly only from the dynamics of the population sizes, and this is the main reason that the estimated fraction of the rescued DP cells varies in the previous studies and also in our case.

2.2.5 DP and CD4 SP thymocytes incoherently regulate mTEC recovery

Compared with other thymocytes and TECs, CD4$^+$ SP cells recovered much slower, with less pronounced overshooting (Fig. 2.1b). This slow recovery of CD4$^+$ SP cells is consistent with their lack of proliferation capacity [19, 82], which leads to prolonged recovery. The CD4$^+$ SP dynamics can be reproduced by assuming no proliferation and mTEC-dependent

Term	Symbol	Value	CI	Previous Study
Inflow rate to DN [Cells Day^{-1}] (estimated by the coarse-grained model)	ϕ_1	3.3×10^4	$[3.3 \times 10^4, 6.6 \times 10^4]$	2.0×10^4[80] 1.3×10^4 [92]
Inflow rate to DN [Cells Day^{-1}] (estimated by the detailed model)	ϕ_1	6.61×10^1	N/A	$1.0 \times 10^1 \sim 2.0 \times 10^2$[42] 5.0×10^1 [51]
DN apparent proliferation rate [Day^{-1}]	$\delta_1 - \mu_1(1-r_1)n^*_{\mathrm{cTEC}}$	1.3×10^{-1}	$[-2.2 \times 10^{-2}, 3.3 \times 10^{-1}]$	2.3×10^{-1} [80] 6.2×10^{-4}[92] 3.6×10^{-1}[51]
DN differentiation rate [Day^{-1}]	$\mu_1 r_1 n^*_{\mathrm{cTEC}}$	1.4×10^{-1}	$[5.7 \times 10^{-6}, 3.5 \times 10^{-1}]$	2.4×10^{-1}[80] 2.8×10^{-2}[92] 3.4×10^{-1}[51] 4.5×10^{-1}[58]
DN residence time [Hour]	$24/(\mu_1 r_1 n^*_{\mathrm{cTEC}})$	1.7×10^2	$[6.9 \times 10^1, 4.3 \times 10^6]$	4.2×10^2[80] 3.5×10^2 [51]
DP apparent proliferation rate [Day^{-1}]	$\theta_2(1 - n^*_{\mathrm{DP}}/K_2) - (1-r_{24})\mu_2 n^*_{\mathrm{cTEC}}$	1.0×10^{-1}	$[5.8 \times 10^{-2}, 2.5 \times 10^{-1}]$	1.5×10^{-2}[80] -3.7×10^{-1}[69] -1.6×10^{-1}[58] -9.0×10^{-3}[92]
DP differentiation rate to SP4 [Day^{-1}]	$r_{24}\mu_2 n^*_{\mathrm{cTEC}}$	1.1×10^{-1}	$[6.0 \times 10^{-2}, 2.5 \times 10^{-1}]$	2.1×10^{-2}[80] 1.2×10^{-2} [69] 3.0×10^{-2}[58] 1.8×10^{-2}[92]
DP residence time [Hour]	$24/(r_{24}\mu_2 n^*_{\mathrm{cTEC}})$	2.3×10^2	$[9.5 \times 10^1, 4.0 \times 10^2]$	9.4×10^1[80] 7.6×10^1[69] 1.2×10^2[72]
Proportion of DP to SP4 in DP export [%]	r_{24}	1.0×10^1	$[4.9 \times 10^0, 3.0 \times 10^1]$	6.0×10^0[80] 1.6×10^{-2}[69] 8.1×10^0[58] 6.5×10^1[92]
SP4 apparent export rate [Day^{-1}]	$\mu_4 n^*_{\mathrm{mTEC}}$	5.2×10^{-1}	$[2.7 \times 10^{-1}, 1.2 \times 10^0]$	2.0×10^{-2}[80] 9.0×10^{-2}[69]

Table 2.2: A comparison of the estimated kinetic rates with those from previous studies.(CI: Confidence interval) The value of each term is calculated with the steady state values of cell populations n_i^*. We note that our point estimate of the DP residence time 230 h may be an overestimate, although the previous estimates overlap the statistically confident range of the values obtained by our bootstrap analysis. This is because the residence time was estimated only from the output flux rate, due to the fact that the apoptosis rate cannot be estimated in our model.

death and outflux $-\mu_4 n_{\mathrm{mTEC}}(t)$, which may represent the negative selection of SP cells by mTECs (Fig. 2.3a).

In contrast, the mTEC recovery was initiated almost concurrently with that of cTEC (Fig. 2.1b). While interactions with $CD4^+$ SP cells have been proven essential for the maturation of mTECs [77], the prolonged $CD4^+$ SP recovery is insufficient for reproducing earlier onset of mTEC recovery. Our model incorporates an auto-inhibitory regulation of mTEC proliferation $r_{\mathrm{m}}(1-n_{\mathrm{mTEC}}(t)/K_{\mathrm{m}})$ and its negative regulation by DP cells with a time delay $-\gamma_{\mathrm{mp}} n_{\mathrm{DP}}(t-\tau_{\mathrm{m}})$ as in Eq.(2.2). The auto-inhibitory regulation is necessary because without it, we obtained biologically inconsistent parameter values in mTEC dynamics (Figs. 2.9a and 2.9b). The negative regulation by DP cells is also responsible for mTEC overshooting. Preceding experimental investigations [17, 56] support these mechanisms. Metzger *et al.* reported that the percentage of Ki67hi mTECs increases only after the depletion of mTECs [56], suggesting auto-inhibitory regulation. Based on a depletion experiment of DP cells, Dudakov *et al.* suggested that DP cells negatively regulated TEC proliferation in an IL22 dependent manner [17]. However, the DP-dependent regulation was not the sole interaction that could explain the early onset of mTEC recovery. We also found that a DN-dependent regulation could reproduce it (Figs. 2.9c and 2.9d). However, this possibility was excluded in our model because we lack molecular evidence supporting the long-range interaction from DN cells to mTECs, which reside in spatially segregated areas of a thymus.

Along with regulated proliferation, our model assumes reciprocal regulations between mTECs and $CD4^+$ SP cells to account for evidence that mTEC maturation is also related with $CD4^+$ SP cells. According to Williams *et al.* [87], mTECs express ligands CD80 and CD86 and a receptor, CD40; the corresponding ligand and receptor of $CD4^+$SP cells are mainly CD28 and CD40L, respectively. A knockout of CD80, CD86, and CD40 was shown to decrease the number of mTECs and double the number of $CD4^+$ SP cells. We substituted smaller values of μ_4 and ϕ_{m4} than the estimated values into our model to reproduce the experiment in ref. [87] by assuming that the knock-out of CD80, CD86, and CD40 corresponds to this substitution. The result qualitatively reproduced the knock-out mutant result in ref. [87]; the stable number of $CD4^+$ SP cells doubled whereas the number of mTECs was decreased as shown in Fig. 2.7d.

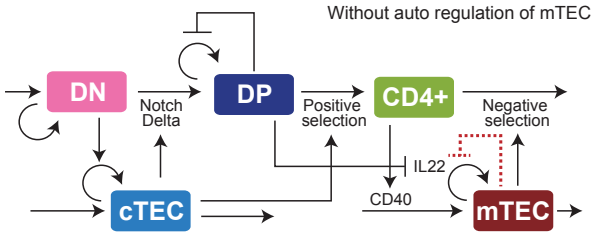

(a)

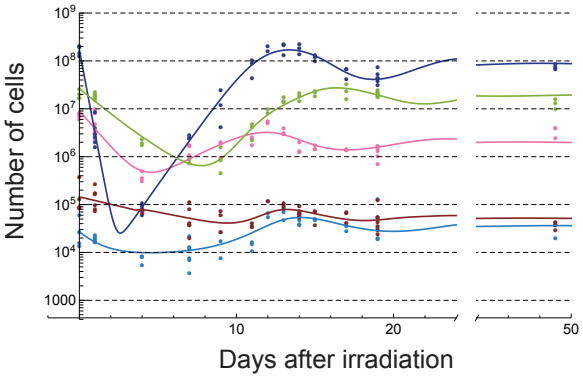

(b)

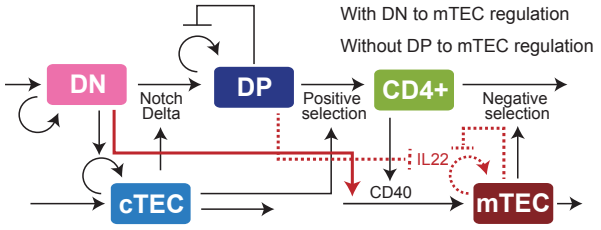

(c)

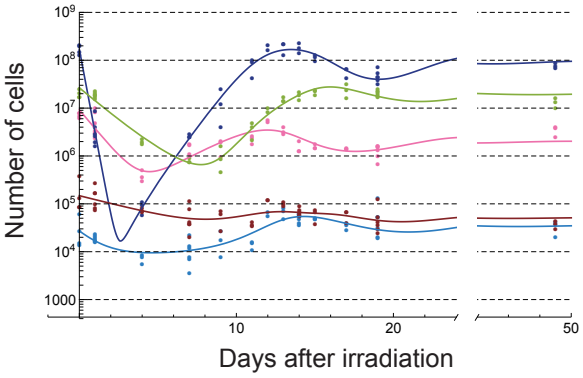

(d)

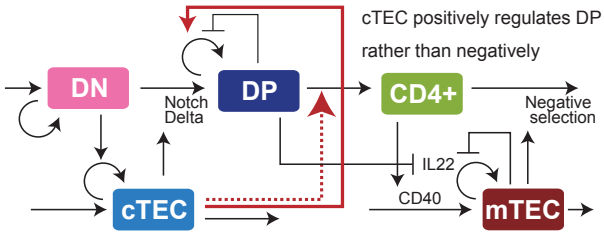

(e)

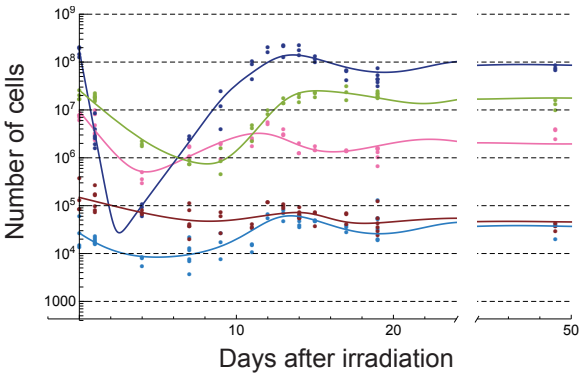

(f)

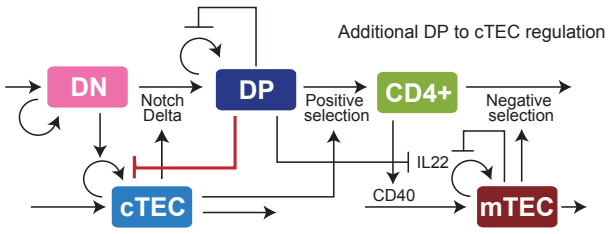

(g)

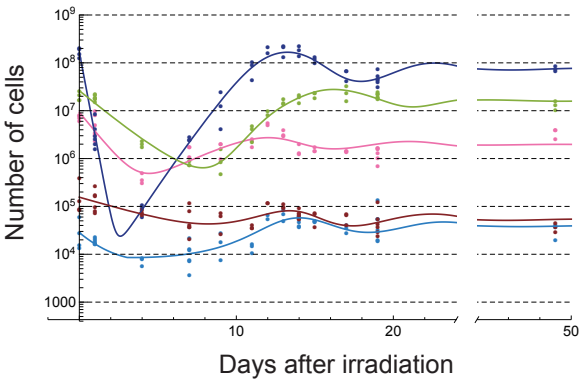

(h)

Figure 2.9: (Continued on the following page.)

Figure 2.9: Possible regulatory mechanisms that are capable of reproducing the recovery dynamics of the data, but that are biologically less relevant than the proposed model shown in Fig. 2.3a. Differences between each model and the one shown in Fig. 2.3a are designated by red solid lines if additionally included or red broken lines if excluded. The equations corresponding to the models are shown in Methods. The model in (a) excludes the autoinhibitory regulation of mTECs. The model in (c) includes an interaction from DN cells to mTECs influx instead of the inhibition from DP cells. The model in (e) assumes that cTECs promote DP cell proliferation, rather than inducing DP cell differentiation or cell death. The model in (g) includes an inhibitory regulation of cTECs from DP cells similar to that of mTECs. (b), (d), (f), and (h) show corresponding trajectories of the models in (a), (c), (e), and (g), respectively.

2.3 Discussion

From quantitative time-series data of thymocytes and TECs recoveries after sub-lethal X-ray irradiation, we constructed a mathematical model for the recovery dynamics of thymocytes and TECs. The model reproduces the transient dynamics of the cell population sizes fairly well, and most of the interactions identified by the modeling are consistent with known molecular evidence.

Since previous modeling works on quantitative characterizations of thymocyte development focused only on thymocytes dynamics, our work, which additionally includes both the dynamics of and the interactions with TECs, can be viewed as an extension of those works [51, 55, 58, 69, 80, 92]. We validated that the estimated parameter values of thymocytes in our model are mostly consistent with those estimated in previous works (Table 2.2). Few parameter value mismatches may also be attributed to differences in the experimental setting and conditions. However, it should be noted that we compared the apparent proliferation rates of our model to previous estimates, which are the marginal rates of population size change owing to the imbalance between proliferation and apoptosis because pure rates of proliferation or apoptosis cannot be estimated from our model. To reveal dynamical change in apoptosis rates, we must develop a new approach that combines our reciprocal regulation model with experimental methods that can directly quantify thymocyte proliferation, apoptosis and differentiation [7, 76]. Further, the parameters of TECs are the first to be estimated by modeling, and should be verified by independent research. Particularly, damage caused by irradiation can affect the thymic tissue structure, which may result in a systematic bias

when counting TECs [30, 67]. While this systematic bias is effectively absorbed in our model by parameters scaling, this potential scaling must be considered when we compare our TEC parameter value estimates with others. Moreover, to assess this problem more carefully, we must develop a new image analysis method that can accurately detect and count cells in 3D tissue images obtained by advanced imaging and tissue clearing [57, 62].

Thymic crosstalk includes various signaling pathways, indicating complex regulations behind the population size control of thymocytes and TECs. Because of this complexity, our model may contain missing interactions or possibly different regulations, some of which were tested during our model identification process. Such possibilities cannot be excluded by the limited amount of the data alone; therefore, we employed previously obtained molecular biological evidence and quantitative estimates to evaluate the possible models.

For example, cTECs rescue DP thymocytes from apoptosis via positive selection, which leads to increase the DP population size. Concurrently, positive selection also induces differentiation of thymocytes from the DP stage to the SP stage, causing DP population size to decrease. These contradicting interactions introduce the possibility that cTECs increase the DP thymocyte population size, rather than decreasing it as assumed in our model. We examined this possibility by introducing the increasing effect of the DP population size by cTECs and concluded that the decreasing effect assumed by our model is more valid because the model with the increasing effect resulted in much higher parameter values than expected based on the previous works (Figs. 2.9e and 2.9f).

We also investigated a model in which DP thymocytes contribute to the recovery of both mTECs and cTECs [17]. We found that the estimated parameter for the interaction from DP cells to cTECs was almost 0 (Figs. 2.9g and 2.9h), which does not support a major contribution of DP cells to cTECs recovery under our experimental condition.

Our model can explain the mechanisms by which specific dynamics appear in recovery dynamics and their potential biological functions; overshoots of DN thymocytes and cTECs may originate from negative feedback between them and may contribute to prompt recovery from various perturbations affecting thymocyte and TEC numbers. Similarly, the disinhibition of DP proliferation upon DP population size decrease facilitates the swift recovery of DP cells, which could not be achieved solely by the influx of DN cells, as they have a

much smaller population size than DP cells. Our model provides an integrative view of thymic crosstalk as a regulatory network and serves as a starting point for comprehensive understanding of homeostasis in thymic development.

However, our model still has room for future improvement by accommodating more detailed information on the cellularity of the thymic resident cells, such as B cells, dendritic cells, and thymic endothelial cells. These cells may have different roles in the dynamic regulation of thymic homeostasis than thymocytes and TECs, although we did not explicitly include them by presuming that their effects to the number of thymocytes or TECs are relatively small or constant, which was implicitly modeled by the constant parameters in our model. Actually, BMP4 production by endothelial cells after irradiation, which can contribute to TECs recovery, was reported constant when normalized by the size of thymus [86]. Explicitly incorporating these cells may be crucial to extending our model to other experimental settings as well as for deriving a more integrative and comprehensive model of thymic development and homeostasis. Among others, the repertoires of thymocytes are particularly relevant. TECs are responsible for controlling the number of thymocytes as well as for selecting thymocytes with appropriate repertoires. An upcoming challenge may be integrative modeling and analyzing thymic homeostasis, both in cell number and repertoires by combining quantitative measurement and high-throughput sequencing [74].

2.4 Methods

2.4.1 Experiment

Animals used in the present study were maintained in accordance with the "Guiding Principles for Care and Use of Animals in the Field of Physiological Science" set by the Physiological Society of Japan. All animal experiments were approved by the Animal Research Committees of RIKEN.

Balb/cA mice were purchased from CLEA Japan. Female mice (7 weeks-old) received X-ray radiation (4.5 Gy). At each sampling point after irradiation, the mice were sacrificed and their thymi were used for a flow cytometric analysis. Each thymus was cut and gently agi-

tated in 2 ml of RPMI-1640 (Sigma-Aldrich, St. Louis, MO, U.S.A.) to release thymocytes for the flow cytometric analysis. The days of measurement and the number of sampled mice are shown in Table 2.1. The remaining thymic tissue was digested using Liberase in RPMI1640 (Wako) at 37 °C for 30 min. The thymic stroma-rich-fraction was analyzed by flow cytometry to detect TEC populations. For flow cytometric staining, cells were pre-treated with anti-CD16 and CD32 (Biolegend) for 20 min and subsequently stained with fluorescence-labeled antibodies in phosphate buffered saline containing 3% fetal bovine serum. The stained cells were analyzed using Canto II (BD). The total thymic cell numbers were determined by the sum of cells in the thymic stroma-rich fraction and the thymocyte fraction. TECs were defined as CD45-TER119-EpCAM+ cells. mTECs and cTECs were separated with UEA-1 staining. For DN thymocyte staining, the lineage negative cell fraction was separated by staining with CD25 and CD44 antibodies. Since the DN population contains other minor cell populations such as dendritic cells, the number of cells from these fractions was subtracted from the number of DN cells in the mathematical modeling based on the average percentage of these cells (16.6%) in the DN fraction under steady conditions (Fig. 2.2a). PECy7-anti-CD4 (clone RAM4-4, used as ×200 dilution), FITC-anti-CD4 (clone RAM4-4, ×200 dilution), APCCy7-anti-CD8 (clone 53-6.7, ×200), APCCy7-anti-CD45 (clone 30 F-11, ×200), APCCy7-anti-TER119 (clone TER-119, ×200), FITC-anti-EpCAM (BioLegend, clone G8.8, ×400), PE-anti-CD80(clone 16-10A1, ×400), Biotin-anti-mouse Ly-6G/Ly-6C(Gr-1) (×400), Biotin anti-mouse/human CD45R/B220 (×400), Biotin anti-mouse TER-119/Erythroid cells (clone TER-119, ×400), Biotin conjugated anti-mouse CD11b (×400), PE anti-mouse/human CD44 (clone IM7, ×400), APC anti-mouse CD25 (clonePC61, ×400), Streptavidin PE-Cyanine7 (×400), and Streptavidin-PECy7 (×400) were purchased from Biolegnd. UEA-biotin (×400) was from Vector laboratories (Burlingame, CA).

In the proliferation assay, thymocytes were pre-treated with anti-CD16 and CD32 (Biolegend) and subsequently stained with anti-CD4 and anti-CD8 antibodies in phosphate buffered saline containing 3% FBS. The cells were fixed and permeabilized with Foxp3/Transcription Factor Staining Buffer Set (eBioscience) according to the manufacturer' s protocol. After fixation and permeabilization, the cells were stained with a PE-labeled anti-Ki67 antibody (Biolegend) and subsequently analyzed by Canto II (BD).

2.4.2 Mathematical Modeling of Thymocyte and TEC dynamics

We assume that the total number of the type i cells, n_i^{tot}, is the sum of cells dying by irradiation n_i^{x} and survived or newly generated cells n_i:

$$n_i^{\mathrm{tot}}(t) = n_i^{\mathrm{x}}(t) + n_i(t), i \in C := \{\mathrm{DN}, \mathrm{DP}, \mathrm{SP4}, \mathrm{cTEC}, \mathrm{mTEC}\} \ , \tag{2.3}$$

where C is the set of the cell types.

We describe the decrease in the irradiated cells by an exponential decay, which assumes that cells die at a constant rate ω_i after irradiation:

$$n_i^{\mathrm{x}}(t) = n_i^{\mathrm{x}}(0)e^{-\omega_i t} \ . \tag{2.4}$$

In the model, $n_i^{\mathrm{tot}}(0)$ represents the initial population size of type i cells and p_i is assumed to be the fraction of survived cells at $t \leq 0$ as

$$n_i(t) = \begin{cases} n_i^{\mathrm{tot}}(0), & t < 0 \\ p_i n_i^{\mathrm{tot}}(0), & t = 0 \end{cases} , \tag{2.5}$$

$$n_i^{\mathrm{x}}(t) = \begin{cases} 0, & t < 0 \\ (1-p_i) n_i^{\mathrm{tot}}(0), & t = 0 \end{cases} . \tag{2.6}$$

Given these initial conditions, the model of Eq. (2.2) was implemented on MATLAB (R2018a; The MathWorks, Natick, MA) and numerically simulated by the 'dde23' function or on Mathematica (version 11.2; Wolfram research, Champaign, Illinois) and simulated by the 'NDSolve' function.

2.4.3 Parameter estimation

In the parameter estimation, ω_i, $n_i^{\mathrm{tot}}(0)$, p_i, and all parameters appearing in Eq. (2.2) were simultaneously estimated. Parameters were estimated by minimizing the sum of the squares of difference between the logarithms of the observed data and simulated values of the model.

Because the orders of the parameters are different, and this caused difficulty in the minimization, we decomposed the parameters as $\boldsymbol{\theta} = \boldsymbol{\theta}_c \circ \boldsymbol{\theta}_p$, where $\boldsymbol{\theta}_c$ is a coefficient vector to estimate, $\boldsymbol{\theta}_p$ is a constant vector of a power of 10, and $\circ$ denotes elementwise multiplication. For the observed time points $\mathbf{t}^* = [t_i, \cdots, t_m]$ and the corresponding data points $N_i(t_j)$ for all $i \in C$, the estimated parameter set $\hat{\boldsymbol{\theta}}$ was obtained by solving

$$\begin{aligned} \hat{\boldsymbol{\theta}}_c &= \arg\min_{\boldsymbol{\theta}_c} \sum_{j=1}^{m} \sum_{i \in C} [\ln(n_i^{\text{tot}}(t_j, \boldsymbol{\theta}_c \circ \boldsymbol{\theta}_p)) - \ln(N_i(t_j))]^2 \ , \\ \hat{\boldsymbol{\theta}} &= \hat{\boldsymbol{\theta}}_c \circ \boldsymbol{\theta}_p \end{aligned} \tag{2.7}$$

To solve this minimization, we used the 'lsqnolin' function in MATLAB Optimization Toolbox in which parameters were estimated by Trust Region Reflective method. The initial parameter values in the estimation were given, so that the result converges to moderate values considering the results of related previous works. The searching range of each parameter except p_i, r_1, and r_{24} was set between 10 and 0.1 times the initial value. Since p_i, r_1, and r_{24} represent fractions, their searching ranges were set between 0 and 1. The symbols, descriptions, and estimated values of the parameters are listed in Table 2.3.

2.4.4 Confidence Interval by bootstrap

We calculated the confidence intervals of the estimated parameter values by a bootstrap method [16].

First, for type i cells, we modeled the statistical variation of the data points using a Gaussian random variable $\varepsilon_i \sim \mathcal{N}(0, \sigma_i^2)$ with mean 0 and variance σ_i^2 as

$$\ln(N_i(t)) = \ln(n_i^{\text{tot}}(t, \hat{\boldsymbol{\theta}})) + \varepsilon_i \ . \tag{2.8}$$

We estimated σ_i^2 by the sample variance as

$$\hat{\sigma}_i^2 = \frac{1}{m-1} \sum_{j=1}^{m} [\ln N_i(t_j) - \ln n_i^{\text{tot}}(t_j, \hat{\boldsymbol{\theta}})]^2 \ . \tag{2.9}$$

We obtained the kth bootstrapped sample of the time point t_j, $N_i^{b_k}(t_j^*)$ by using a random

Symbol	Description	Value [CI]
p_1	Proportion of normal cells in the initial number of DN	1.7×10^{-5} [1.4×10^{-7}, 1.2×10^{-2}]
ω_1	Death rate of irradiated DN	9.2×10^{-1} [7.0×10^{-1}, 1.4×10^{0}]
$n_{\mathrm{DN}}(0)$	Initial value for the number of DN	9.3×10^{6} [6.9×10^{6}, 1.4×10^{7}]
ϕ_1	Inflow to DN	3.3×10^{4} [3.3×10^{3}, 6.6×10^{4}]
μ_1	Negative regulation by cTEC to DN	1.3×10^{-5} [8.1×10^{-6}, 2.1×10^{-5}]
δ_1	Intrinsic proliferation rate of DN	4.7×10^{-1} [2.8×10^{-1}, 6.9×10^{-1}]
r_1	Proportion of differentiation to DP in regulation by cTEC	2.9×10^{-1} [1.6×10^{-5}, 6.9×10^{-1}]
p_2	Proportion of normal cells in the initial number of DP	6.9×10^{-6} [4.5×10^{-9}, 8.4×10^{-5}]
ω_2	Death rate of irradiated DP	4.0×10^{0} [3.5×10^{0}, 4.5×10^{0}]
$n_{\mathrm{DP}}(0)$	Initial value for the number of DP	1.7×10^{8} [1.2×10^{8}, 2.5×10^{8}]
r_2	Proliferation rate of DP	1.3×10^{0} [1.1×10^{0}, 1.5×10^{0}]
k_2	Carrying capacity of DP	4.2×10^{8} [2.4×10^{8}, 1.4×10^{9}]
μ_2	Negative regulation rate by cTEC to DP	2.9×10^{-5} [2.1×10^{-5}, 4.0×10^{-5}]
τ	Delay of cTEC regulating DP	2.1×10^{0} [1.2×10^{0}, 3.1×10^{0}]
r_{24}	Proportion of differentiation to CD4+SP in regulation by cTEC	1.0×10^{-1} [4.9×10^{-2}, 3.0×10^{-1}]
p_c	Proportion of normal cells in the initial number of cTEC	7.6×10^{-1} [1.1×10^{-4}, 9.8×10^{-1}]
ω_c	Death rate of irradiated cTEC	7.7×10^{-1} [9.3×10^{-2}, 7.6×10^{0}]
$n_{\mathrm{cTEC}}(0)$	Initial value for the number of cTEC	2.7×10^{4} [1.9×10^{4}, 4.3×10^{4}]
ϕ_c	Inflow to cTEC	6.5×10^{3} [4.3×10^{3}, 8.8×10^{3}]
γ_c	Death rate of cTEC	7.9×10^{-1} [5.4×10^{-1}, 1.3×10^{0}]
θ_c	Positive regulation by DN to cTEC	3.1×10^{-7} [2.0×10^{-7}, 5.7×10^{-7}]
p_4	Proportion of normal cells in the initial number of CD4+SP	1.5×10^{-2} [8.2×10^{-5}, 1.1×10^{-1}]
ω_4	Death rate of irradiated CD4+SP	6.3×10^{-1} [5.0×10^{-1}, 8.3×10^{-1}]
$n_{\mathrm{SP4}}(0)$	Initial value for the number of CD4+SP	2.7×10^{7} [2.2×10^{7}, 3.4×10^{7}]
γ_4	Negative regulation by mTEC to CD4+SP	9.9×10^{-6} [4.7×10^{-6}, 2.5×10^{-5}]
p_m	Proportion of normal cells in the initial number of mTEC	3.1×10^{-6} [5.5×10^{-8}, 4.4×10^{-1}]
ω_m	Death rate of irradiated mTEC	1.6×10^{-1} [10.0×10^{-2}, 2.8×10^{-1}]
$n_{\mathrm{mTEC}}(0)$	Initial value for the number of mTEC	1.4×10^{5} [1.1×10^{5}, 1.9×10^{5}]
ϕ_m	Constant inflow to mTEC	1.5×10^{1} [1.5×10^{0}, 1.2×10^{2}]
ϕ_{m4}	Inflow to mTEC regulated by CD4+SP	1.6×10^{-4} [1.6×10^{-5}, 1.5×10^{-3}]
r_m	Proliferation rate of mTEC	6.1×10^{-1} [1.7×10^{-1}, 1.2×10^{0}]
K_m	Carrying capacity of mTEC	9.2×10^{4} [4.9×10^{4}, 7.4×10^{5}]
μ_{mp}	Negative regulation rate by DP to mTEC	3.5×10^{-9} [1.8×10^{-9}, 8.2×10^{-9}]
τ_m	Delay of DP regulating mTEC	3.3×10^{0} [2.1×10^{0}, 6.2×10^{0}]

Table 2.3: Estimated parameter values in the coarse-grained model. (CI : confidence interval). We should note that this is the first systematic estimate of the parameters related to the dynamics of TECs. These parameters should be verified by independent researches.

number $\varepsilon_{i,j}^k \sim \mathcal{N}(0, \hat{\sigma}_i^2)$ as

$$\ln N_i^{b_k}(t_j) = \ln n_i^{\mathrm{tot}}(t_j, \hat{\boldsymbol{\theta}}) + \varepsilon_{i,j}^k \ . \tag{2.10}$$

The kth bootstrapped parameter set $\hat{\boldsymbol{\theta}}^{b_k}$ was obtained by solving the same optimization problem of the previous section by replacing the data with the kth bootstrapped sample $N_i^{b_k}(t_j)$ as

$$\hat{\boldsymbol{\theta}}^{b_k} = \arg\min_{\boldsymbol{\theta}} \sum_{j=1}^{m} \sum_{i \in C} [\ln(n_i^{\mathrm{tot}}(t_j, \boldsymbol{\theta})) - \ln(N_i^{b_k}(t_j))]^2 \ . \tag{2.11}$$

The total number of the bootstrapped samples generated was $B = 1000$. The two-sided $\alpha * 100$ % confidence interval of the lth parameter was calculated as $[\hat{\theta}_l^{\frac{B(1-\alpha)}{2}}, \hat{\theta}_l^{\frac{B\alpha}{2}}]$ where $\hat{\theta}_l^{(x)}$ is the xth smallest value of the $l$thparameter obtained from the bootstrapped samples. The confidence interval of each parameter is shown in Table 2.3. A pairwise scatter plot of the bootstrap estimates is shown in Fig. 2.6. The trajectories of the cells obtained from 100 samples of the bootstrap parameter sets are shown in Fig. 2.3c.

2.4.5 Detailed model of DN thymocytes

We additionally measured dynamic changes in the population sizes of DN1, DN2, DN3, and DN4 cells after irradiation.

To estimate the DN subpopulation dynamics in the original data (Fig. 2.1b), we utilized the DN subpopulations data as follows. First, we calculated the average proportions of the DN subpopulations at each time point. Subsequently, assuming that the dynamics of the DN subpopulation proportions were the same as the original data, we multiplied the number of DN cells from the original data with the calculated DN subpopulation proportions at each time point. At time points where we did not have corresponding DN subpopulation data (days 12 and 14), we used the average proportions of neighboring time points (days 11 and 13 for day 12, and days 13 and 15 for day 14).

Employing the obtained estimates of the DN subpopulation dynamics, we estimated the

parameter values of the following detailed model of DN1, DN2, DN3, DN4, DP, and cTEC;

$$
\begin{aligned}
\frac{\mathrm{d}n_{\mathrm{DN1}}}{\mathrm{d}t} &= \phi_1 + (\delta_{\mathrm{DN1}} - \mu_{\mathrm{DN1}} n_{\mathrm{cTEC}}(t)) n_{\mathrm{DN1}}(t) \ , \\
\frac{\mathrm{d}n_{\mathrm{DN}i}}{\mathrm{d}t} &= \mu_{\mathrm{DN}i-1} n_{\mathrm{cTEC}}(t) n_{\mathrm{DN}i-1}(t) + (\delta_{\mathrm{DN}i} - \mu_{\mathrm{DN}i} n_{\mathrm{cTEC}}(t)) n_{\mathrm{DN}i}(t) \ , \\
\frac{\mathrm{d}n_{\mathrm{DP}}}{\mathrm{d}t} &= r_{\mathrm{DN4}} \mu_{\mathrm{DN4}} n_{\mathrm{cTEC}}(t) n_{\mathrm{DN4}}(t) + \left\{ \theta_2 \left(1 - \frac{n_{\mathrm{DP}}(t)}{K_2} \right) - \mu_2 n_{\mathrm{cTEC}}(t - \tau_2) \right\} n_{\mathrm{DP}}(t) \ , \\
\frac{\mathrm{d}n_{\mathrm{cTEC}}}{\mathrm{d}t} &= \phi_{\mathrm{c}} + \left(-\delta_{\mathrm{c}} + \sum_{j=1}^{4} \mu_{\mathrm{cTEC},j} n_{\mathrm{DN}j}(t) \right) n_{\mathrm{cTEC}}(t) \ ,
\end{aligned}
\tag{2.12}
$$

for $i = 2, 3, 4$. The parameter estimation procedure was the same as that for the coarse-grained model. Because the detailed model has parameters common to the coarse-grained model; ϕ_1 and the model parameters of DP and cTECs, except r_{DN4}, μ_{DN4}, and $\mu_{\mathrm{cTEC},i}$, we first fixed those parameter values to the estimates from the coarse-grained model and estimated the remaining parameter values. However, the detailed model with the estimated parameter values did not reproduce the DN1 dynamics (Fig. 2.10). To obtain the parameter values capable of reproducing the dynamics of all cell types, we estimated parameter values including ϕ_1 while other common parameter values were fixed (Fig. 2.7a and Table 2.4).

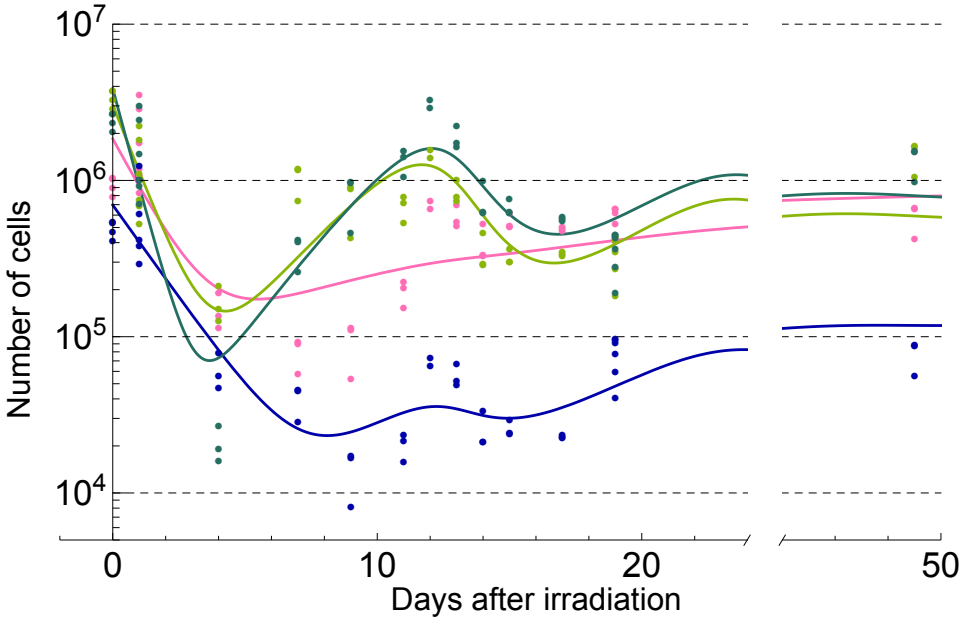

Figure 2.10: Trajectories of the detailed model as a result of fitting to the experimentally obtained dynamics of DN subpopulations while keeping the values of the parameters common to the coarse-grained model fixed. DN1 : pink, DN2 : blue, DN3 : light green, DN4 : green.

Symbol	Description	Value
ϕ_1	Inflow to DN	5.6×10^{1}
δ_{DN1}	Intrinsic proliferation rate of DN1	5.4×10^{-1}
δ_{DN1}	Intrinsic proliferation rate of DN2	3.3×10^{-5}
δ_{DN3}	Intrinsic proliferation rate of DN3	7.4×10^{-1}
δ_{DN4}	Intrinsic proliferation rate of DN4	4.1×10^{-1}
μ_{DN1}	Negative regulation by cTEC to DN1	1.3×10^{-5}
μ_{DN2}	Negative regulation by cTEC to DN2	1.2×10^{-4}
μ_{DN3}	Negative regulation by cTEC to DN3	3.3×10^{-5}
μ_{DN4}	Negative regulation by cTEC to DN4	3.4×10^{-5}
μ_{cTEC1}	Positive regulation by DN1 to cTEC	2.6×10^{-7}
μ_{cTEC2}	Positive regulation by DN2 to cTEC	1.1×10^{-8}
μ_{cTEC3}	Positive regulation by DN3 to cTEC	2.8×10^{-9}
μ_{cTEC4}	Positive regulation by DN4 to cTEC	5.3×10^{-7}
$n_{\mathrm{DN1}}(0)$	Initial value for the number of DN1	1.8×10^{6}
$n_{\mathrm{DN2}}(0)$	Initial value for the number of DN2	7.1×10^{5}
$n_{\mathrm{DN3}}(0)$	Initial value for the number of DN3	2.9×10^{6}
$n_{\mathrm{DN4}}(0)$	Initial value for the number of DN4	3.8×10^{6}
p_{DN1}	Proportion of normal cells in the initial number of DN1	2.3×10^{-3}
p_{DN2}	Proportion of normal cells in the initial number of DN2	2.4×10^{-2}
p_{DN3}	Proportion of normal cells in the initial number of DN3	4.1×10^{-4}
p_{DN4}	Proportion of normal cells in the initial number of DN4	2.5×10^{-5}
ω_{DN1}	Death rate of irradiated DN1	6.2×10^{-1}
ω_{DN2}	Death rate of irradiated DN2	5.1×10^{-1}
ω_{DN3}	Death rate of irradiated DN3	8.9×10^{-1}
ω_{DN4}	Death rate of irradiated DN4	1.4×10^{0}
r_{DN4}	Proportion of differentiation from DN4 to DP in regulation by cTEC	6.7×10^{-1}

Table 2.4: Estimated parameter values in the detailed model.

2.4.6 Possible models (1): No self-suppression of mTEC

We constructed a model of mTEC without the self-suppression (Figs. 2.9a and 2.9b) that had fewer parameters than the proposed model (Figs. 2.3a and 2.3b);

$$\frac{\mathrm{d}n_{\mathrm{mTEC}}}{\mathrm{d}t} = \phi_{\mathrm{m}} + \phi_{\mathrm{m4}} n_{\mathrm{SP4}}(t) - (\gamma_{\mathrm{mp}} n_{\mathrm{DP}}(t - \tau_{\mathrm{m}}) + \mu_{\mathrm{m}}) n_{\mathrm{mTEC}}(t) \ . \tag{2.13}$$

This model is less appropriate than the proposed one because the estimated value of the coefficient $\gamma_{\mathrm{mp}} n^{*}_{\mathrm{DP}} + \mu_{\mathrm{m}}$ was so large that mTECs die within a few hours.

2.4.7 Possible models (2): Regulation by DN to mTEC

We constructed the following model of mTECs with direct regulation by DN cells because the temporal peaks of their population sizes coincided in the data (Figs. 2.9c and 2.9d);

$$\frac{\mathrm{d}n_{\mathrm{mTEC}}}{\mathrm{d}t} = \phi_{\mathrm{mn}} n_{\mathrm{DN}}(t) + \phi_{\mathrm{m4}} n_{\mathrm{SP4}}(t) - \mu_m n_{\mathrm{mTEC}}(t) \ . \tag{2.14}$$

We rejected this model because we have no evidence of direct interaction between DN thymocytes and mTECs, which are located in different regions of a thymus.

2.4.8 Possible models (3): Increase of DP by cTEC

We constructed a model of DP cells in which cTECs promote the increase in the DP population size by assuming that cTECs either induce DP proliferation or rescue DP thymocytes from apoptosis in positive selection (Figs. 2.9e and 2.9f);

$$\frac{\mathrm{d}n_{\mathrm{DP}}}{\mathrm{d}t} = \mu_1 r_1 n_{\mathrm{cTEC}}(t) n_{\mathrm{DN}}(t) + r_2 n_{\mathrm{DP}}(t) \left(1 - \frac{n_{\mathrm{DP}}(t)}{K_2}\right) + \mu_2 n_{\mathrm{cTEC}}(t) n_{\mathrm{DP}}(t) \ . \tag{2.15}$$

This model was determined inappropriate because the estimated values of the coefficients $r_2(1-n^*_{\mathrm{DP}}/K_2)$ and $\mu_2 n^*_{\mathrm{cTEC}}$ were so large that self replication and apoptosis occurred within a few hours.

2.4.9 Possible models (4): Regulation by DP to cTEC

We constructed a model of cTECs with a regulation by DP thymocytes (Figs. 2.9g and 2.9h) because the depletion of DP thymocytes was reported to induce recovery both of mTECs and cTECs [17];

$$\frac{\mathrm{d}n_{\mathrm{cTEC}}}{\mathrm{d}t} = \phi_{\mathrm{c}} + (-\delta_{\mathrm{c}} + \mu_{\mathrm{c}} n_{\mathrm{DN}}(t) - \gamma_c n_{\mathrm{DP}}(t - \tau_{\mathrm{m}})) n_{\mathrm{cTEC}}(t) \ . \tag{2.16}$$

We found that the assumed effect of DP cells to cTECs was negligible because the substitution of 0 to γ_{c} did not change the dynamics after the parameter estimation. Thus, we did

not adopt this additional interaction.

Chapter 3

TCR repertoire analysis of thymic selection and its perturbation

3.1 Introduction

Appropriate diversity of a TCR repertoire is central to the ability of the adaptive immunity to protect against pathogens. This diversity is generated by the probabilistic mechanisms during the T cell development in the thymus: the random gene recombination and the clonal selection.

Statistical property of these probabilistic mechanisms has been studied, especially after the emergence of high-throughput sequencing. TCRs that contain specific amino acids with specific lengths tended to be selected in the thymus [47]. One of the tendencies was that TCRs that were more likely to be produced by the recombination were more likely to pass the thymic selection [20]. Nevertheless, the selection bias did not seem to contribute to how much TCR repertoire is shared among individuals [43].

Impaired functionality of those mechanisms in the thymus for appropriate TCR repertoire can result in T cell immunodeficiency. The cause of some autoimmune diseases has been revealed to be related to the deficiency of the thymic development; in a mouse model of systemic lupus erythematosus, one of the autoimmune diseases, the diversity of both thymic and splenic TCRβ repertoire were significantly low [45]. On the other hand, specific genetic mutation related to the thymus has also been studied; when some genes related to the production of self-peptides in TECs such as thymus-specific serine protease are knocked out, T cells with TCRs specific to several antigens were impaired [83].

The deficient generation of TCR repertoire in the thymus is caused not only by genetic defects but also by temporal perturbation such as stress, infection, and medical treatments. Those perturbations lead to acute thymic atrophy and consequent less-diverse TCR repertoire output [28]. However, it is still poorly understood how thymic atrophy and following recovery change the TCR repertoire. In this study, we analyzed dynamical changes of the thymic TCR repertoire during thymic involution and subsequent recovery after X-ray irradiation.

Table 3.1: The sample size on each day after irradiation. On day 4 of group 1, we had 3 samples for SP cells and 2 samples for DP cells.

Days after irradiation	0	4	7	11	13	17	19	30	42
Group 1	3	3(2)	3	3	3	3	3		
Group 2	2		2		2		3	3	3

3.2 Materials and methods

3.2.1 Experiment

Animals used in the present study were maintained in accordance with the "Guiding Principles for Care and Use of Animals in the Field of Physiological Science" set by the Physiological Society of Japan. All animal experiments were approved by the Animal Research Committees of RIKEN.

We artificially perturbed populations of thymocytes in the thymus by sub-lethal 4.5 Gy irradiation to mice (7 weeks-old), and we performed deep sequencing of TCRα and TCRβ chains from CD69$^+$DP and CD4$^+$SP thymocytes during the recovery from irradiation. The CD69$^+$ population in DP cells is those that have completed positive selection [68]. We hereafter refer to CD69$^+$DP cells and CD4$^+$SP cells as DP cells and SP cells, respectively. We experimented with the same condition twice but different sampling time points; on the second run, we measured samples later than the first run. The sample size at each time point after irradiation is shown in Table 3.1. We denote the first run as group 1 and the second run as group 2 hereafter. Preprocessing was conducted using proprietary software of Repertoire Inc, and we obtained a read count for each combination of V and J gene usages, and an amino acid sequence of a CDR3 region. About 1.4×10^5 reads were observed for one sample on average (Fig. 3.1).

3.2.2 Sequence similarity of CDR3

We employed the sequence similarity index of CDR3 proposed in [91]. This similarity index is based on sequence alignment. To calculate similarity for a pair of CDR3 sequences, we first run a local sequence alignment. We used the blocks substitution matrix (BLOSUM) 62

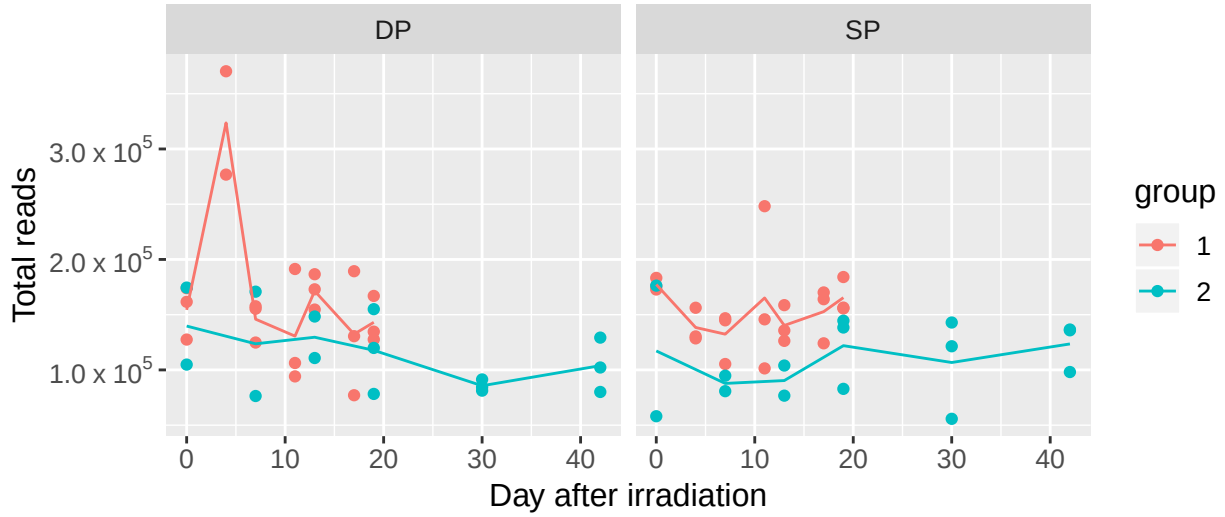

(a)

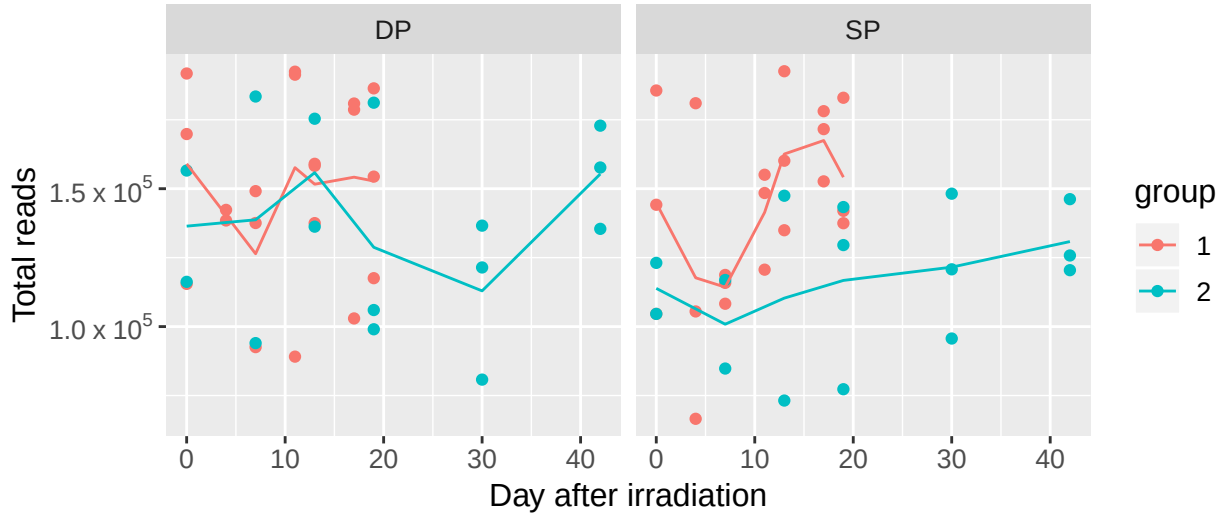

(b)

Figure 3.1: Read counts of (a)TCRα and (b)TCRβ chains on each day after irradiation. Points correspond to the counts of each sample, and lines are linear interpolations of the average reads at each time point.

for the amino acid substitution matrix, which determines the cost of replacing a single amino acid residue by another, and the gap opening and extension penalties were set to 10 and 1, respectively for the local sequence alignment. From the local sequence alignment score, we calculate sequence dissimilarity index as:

$$S_{i,j} = 1 - \frac{2D_{i,j}}{D_{i,i} + D_{j,j}} \ , \tag{3.1}$$

where $D_{i,j}$ and $S_{i,j}$ are the local sequence alignment score and the dissimilarity index between two sequences i and j.

3.2.3 Principal component analysis

Principal component analysis (PCA) is a method to reduce the dimensionality of a data by a linear transformation to a new set of uncorrelated variables, the principal components (PCs) [33]. Suppose we have N observations of P variables ($N > P$), and let X be an $(N \times P)$ observation matrix. A $(N \times P)$ PC score matrix Z is obtained by a linear transform of X,

$$Z = XA \ , \tag{3.2}$$

where A is a $(P \times P)$ orthogonal matrix determined as follows. Let x_p, a_p, and z_p be a pth column vector of X, A, Z, respectively. a_p is determined so that it maximizes a variance of z_p, keeping z_p uncorrelated with $z_{p'}$ for $p' = 1, \cdots, p-1$, under the constraint to be a unit vector.

The quality of representation of the kth variable on the lth PC is expressed by the square of a correlation between x_k and z_l,

$$q(k,l) = \left(\frac{\sigma_{x_k,z_l}}{\sigma_{x_k}\sigma_{z_l}} \right)^2 \ , \tag{3.3}$$

where σ_{x_k} and σ_{z_l} are standard deviations of x_k and z_l, respectively, and σ_{x_k,z_l} is a covariance between x_k and z_l [31].

3.2.4 Correlation ratio

The correlation ratio is a measure that indicates how much the statistical dispersion within individual categories contributes to the dispersion across the whole samples [36]. Suppose we have n samples in total and n_x samples in a category x, and let y_{xi} be ith observation in the category x. The weighted variance of the category means is

$$\sigma_{\bar{y}}^2 = \frac{1}{n}\sum_x n_x(\bar{y}_x - \bar{y})^2 \ , \tag{3.4}$$

where $\bar{y} = 1/n \sum_x \sum_i^{n_x} y_{xi}$ is the mean of the whole sample, $\bar{y}_x = 1/n_x \sum_i^{n_x} y_{xi}$ is the mean of the category x. The weighted mean of the category variances is

$$\bar{\sigma}_x^2 = \frac{1}{n}\sum_x n_x \sigma_x^2 \ , \tag{3.5}$$

where $\sigma_x^2 = 1/n_x \sum_i^{n_x}(y_{xi} - \bar{y}_x)^2$ is the variance of the category x. The variance of all samples $\sigma_y^2 = 1/n \sum_x \sum_i^{n_x}(y_{xi} - \bar{y})^2$ is decomposed as $\sigma_y^2 = \sigma_{\bar{y}}^2 + \bar{\sigma}_x^2$.

The correlation ratio η is defined by the ratio between the weighted variance of the category means and the variance of all samples,

$$\eta^2 = \frac{\sigma_{\bar{y}}^2}{\sigma_y^2} \ . \tag{3.6}$$

3.3 Result

3.3.1 Temporal decrease of CDR3 richness after irradiation and its recovery

We compared the ratio of the number of unique CDR3 to the square root of total reads, which is called Menhinick's index [12], of each sample as a species richness index (Fig. 3.2). The CDR3 richness decreased after irradiation and recovered around 10 days in every TCR chain and cell type. Although α and β chains have different numbers of V, D, and J genes, there was little difference in the CDR3 richness compared to the effect of irradiation. Besides,

the CDR3 richness was relatively higher in SP cells than in DP cells. However, it is not plausible that thymic selection increases the number of unique CDR3s. This suggests that the thymic selection may shift the proportion of each CDR3 in the total sequences toward a uniform distribution. The difference between the groups might be due to different breeding environment.

3.3.2 Most frequent TCRα chain was common in SP thymocytes

The most frequent combination of V, J, and CDR3 was common in most samples of SP cells (Fig. 3.3); a combination of TRAV11D, TRAJ18, and CVVGDRGSALGRLHF was most frequent in 26 out of 37 SP samples. This combination was not observed as the most frequent combination in DP samples; it was different in each DP sample. Furthermore, the significant difference in rank-size distributions between DP and SP samples before irradiation was the prominent abundance of this combination in SP samples (Fig. 3.4). On the other hand, this combination was not frequent in DP cells; it was only observed in 2 out of 3 DP samples at day 0. The abundance of the most frequent combination at day 0 declined by irradiation, and did not get recovered even at 11 days, when the percentage of unique CDR3 counts per total reads had recovered, but in the end at day 42, it got recovered to the original proportion which was significantly higher than that of DP cells (Fig. 3.4).

Thymic selection may cause this prominent abundance of the specific V, J, and CDR3 combination in SP cells and its temporal change. Reactivity of the CDR3 region to self peptides is supposed to determine whether each thymocyte pass thymic selection. Because amino acid sequence similarity of CDR3 sequences correlates with their peptide reactivity [6], we speculated that thymocytes with CDR3 sequences same or similar to CVVGDRGSALGRLHF were also abundant only in $CD4^+$cells. However, combinations of the CDR3 CVVGDRGSALGRLHF with other V and J genes were not frequent in SP or DP cells (Fig. 3.4). Furthermore, there were no sequences similar to CVVGDRGSALGRLHF that were abundant in both DP and SP (Fig. 3.5). Thus, the peptide reactivity of the CDR3 CVVGDRGSALGRLHF did not seem to explain the abundance of the specific combination in SP cells.

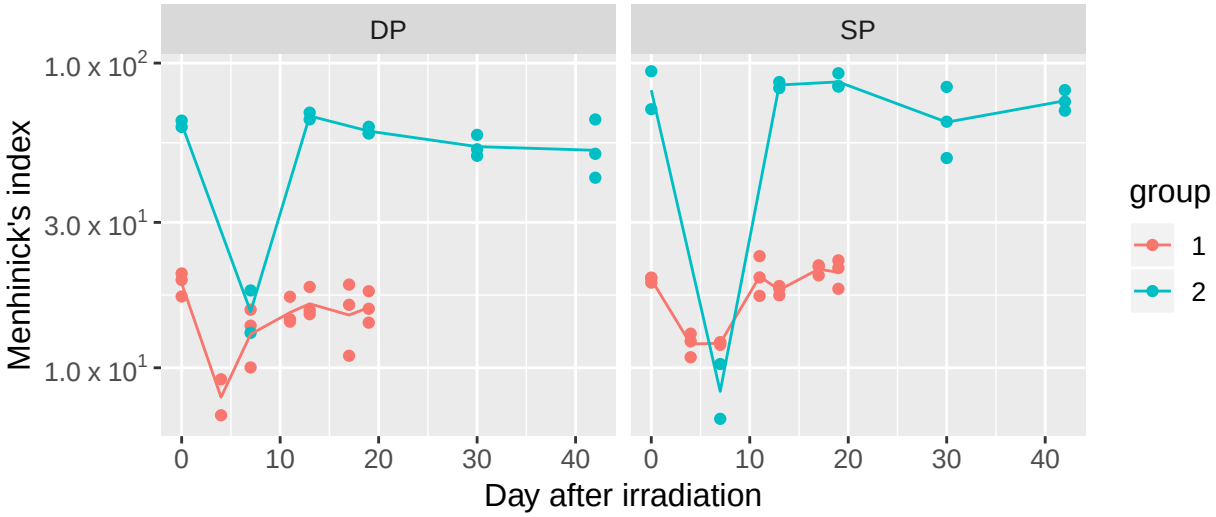

(a)

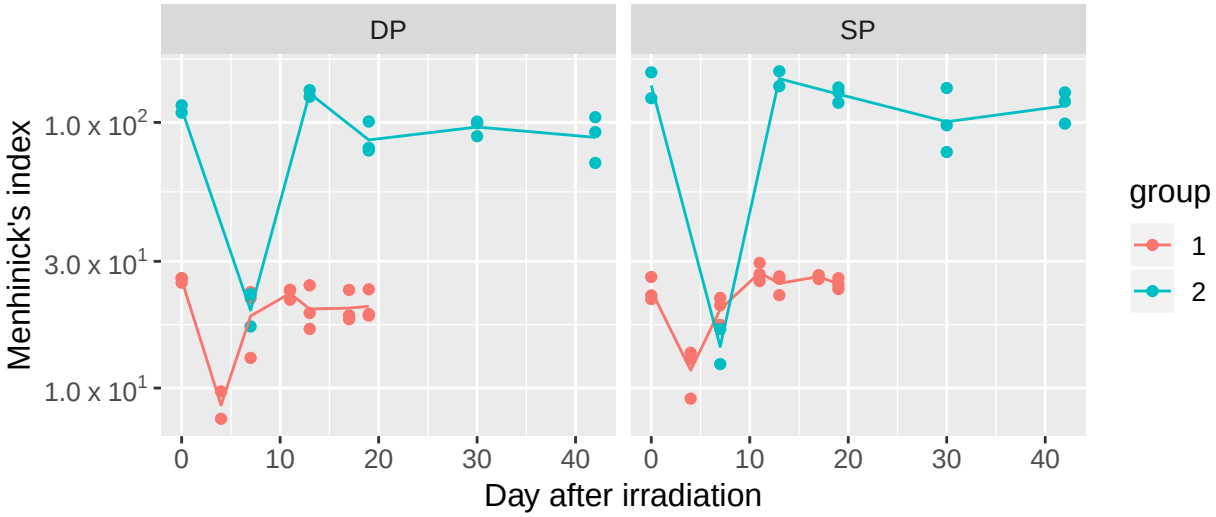

(b)

Figure 3.2: Menhinick's index of (a)TCRα and (b)TCRβ chains on each day after irradiation. Points correspond to the percentage of each sample, and lines are linear interpolations of the average percentage at each time point.

Figure 3.3: The number of times each combination of V, J, and CDR3 was most frequent in each TCRα sample.

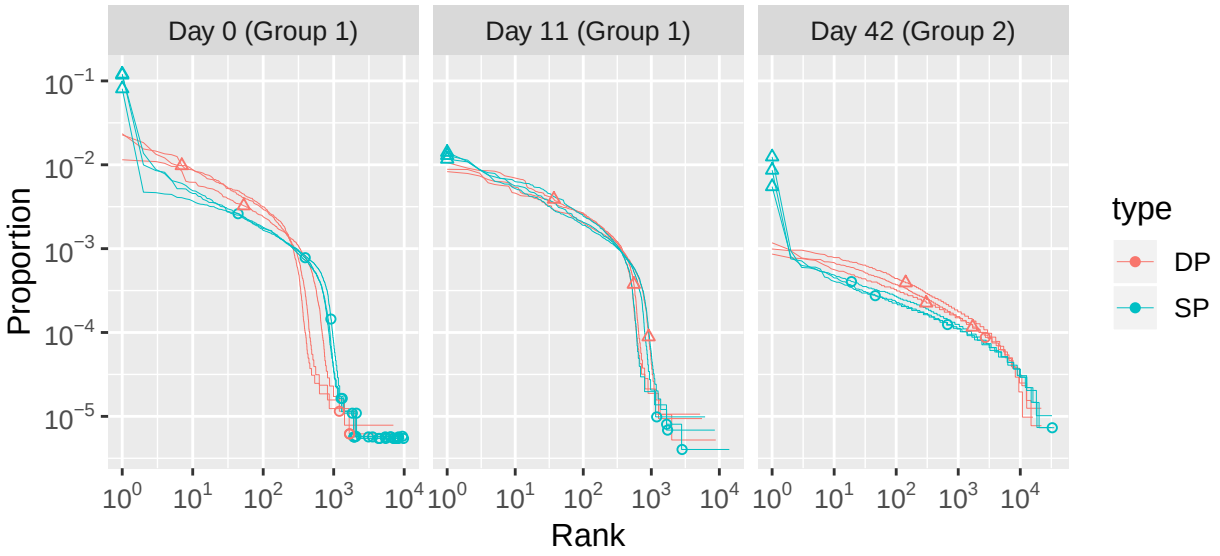

Figure 3.4: Rank size distribution of V, J, and CDR3 combinations in TCRα samples. Triangle points represent positions of TRAV11D, TRAJ18, and CVVGDRGSALGRLHF combination. Circle points represent positions of CVVGDRGSALGRLHF with other V and J combinations.

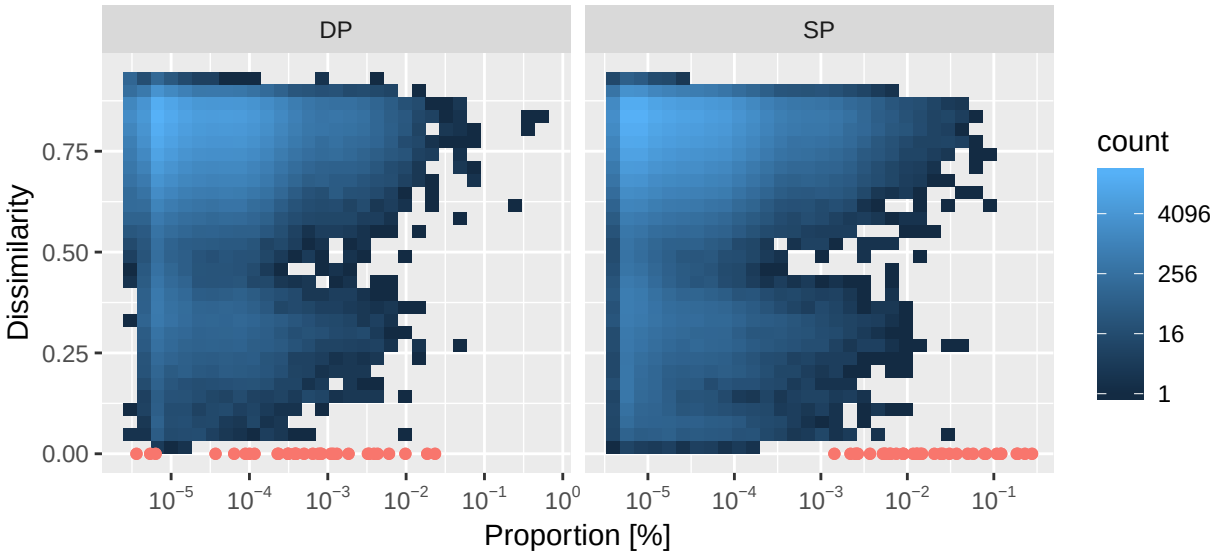

Figure 3.5: Correlation between proportion in a sample and dissimilarity against CVVGDRGSALGRLHF of each CDR3 sequence. Pink points represent values of CVVGDRGSALGRLHF.

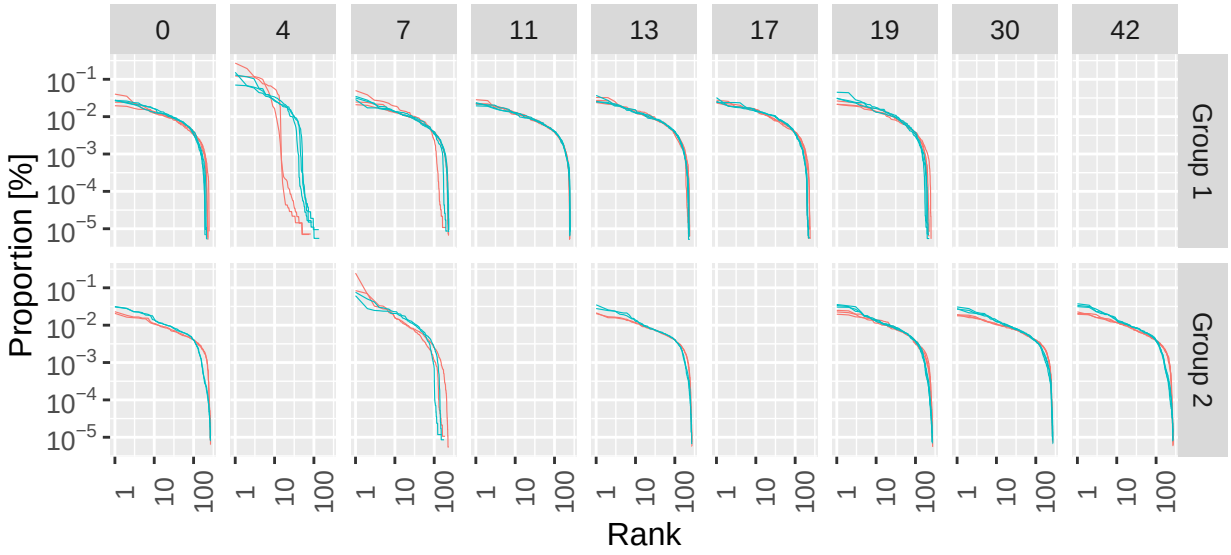

Figure 3.6: Rank size distribution of TCRβ V and J combinations in DP (pink) and SP (cyan) cells. The numbers at the head indicate the day after irradiation.

3.3.3 Difference of TCRβ VJ usage between DP and SP cells

We investigated rank-size distribution of the usage counts of V and J genes (VJ usage) of in TCRβ (Fig. 3.6). In group 2, the proportions of the most abundant VJ combinations were higher in SP cells than DP cells before and 13 days after irradiation; however, in group 1, the difference between DP and SP cells were less obvious. To evaluate the inter-sample difference of the VJ usage, we next applied PCA [33] to the TCRβ VJ usage. Low dimensional representation of each sample by the first and second principal components (PC1 and PC2) captured the differences of cell types as well as the effect of irradiation to the V and J gene usages (Fig. 3.7); PC1 corresponded to the acute change in the gene usage by irradiation, and PC2 corresponded to the difference of the gene usage between DP and SP formed by negative selection.

We then checked the relationship between gene positions and contribution to PC calculated by Eq. (3.3) (Fig. 3.8). Contributions to PCs seemed to correlate with V genes better than with J genes, especially in PC2. Therefore, we compared the correlation ratio (Eq. (3.6)) that measures contribution of inter-group dispersion to the whole dispersion, of V and J gene groups to the quality of representation by PCs(Fig. 3.9). The variance between V genes contributed to the whole variance of the quality of representation remarkably in PC1 and PC2. This V gene dependencies of PC1 and PC2 suggested that both the selection bias

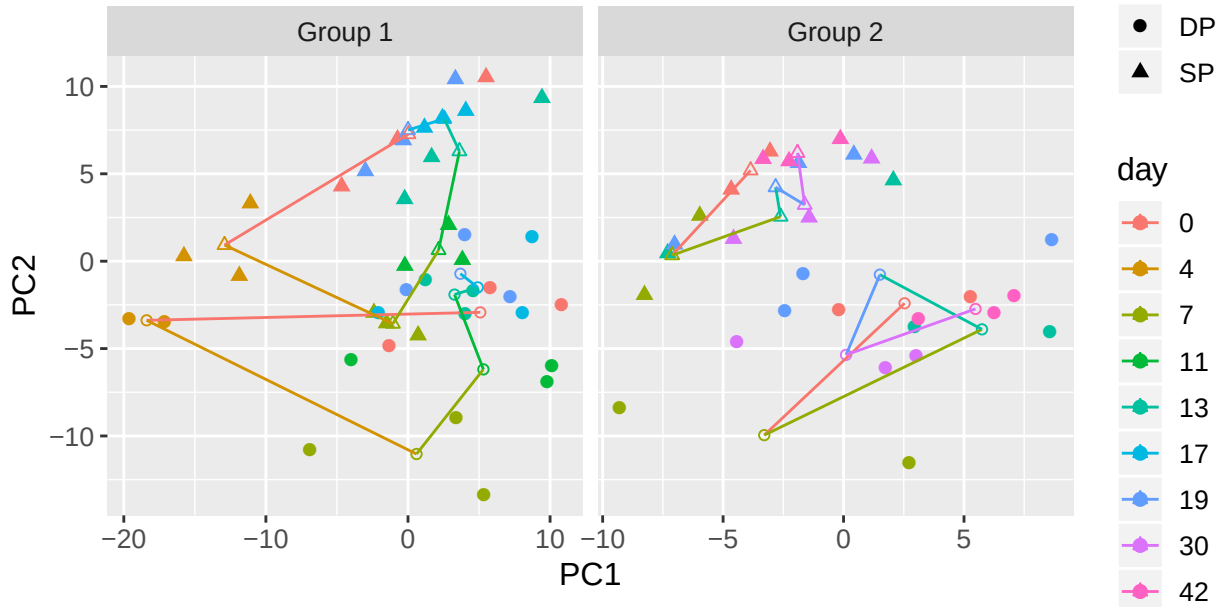

Figure 3.7: 2 dimensional representation of V and J gene usage counts in TCRβ by PCA. Outlined points are averaged PC values of samples at same day for each cell type.

and the acute effect of irradiation changed V gene usage more than J gene usage.

3.3.4 Abundance of specific TCRβ CDR3s after irradiation

There was little difference in the rank-size distribution of TCRβ CDR3 between DP and SP in group 1 except on day 4 and also in group 2 on day 19 and later (Fig. 3.10).

To examine if we could compare the abundance of each CDR3 between samples, we calculated how many samples contained the same CDR3s and the average abundance of the CDR3s in each sample (Fig. 3.11). In group 1, there were only 10 CDRs that were observed in more than one-third of 41 samples, and only 1 out of the 10 CDR3s was observed more than 10 times on average in each sample. On the other hand, in group 2, 363 CDRs were observed in more than two-thirds of 30 samples, and 130 out of the 363 CDR3s were observed more than 10 times on average in each sample.

Therefore, we investigated the transition of proportions of the most common and abundant 130 CDR3s in group 2 (Fig. 3.12). We found that CDR3s that were abundant on day 7, especially in SP cells were also observed on other days with less abundance. This is interesting because thymocytes with CDR3s that are not abundant under normal conditions would not increase their population size by irradiation if every clone was just eliminated

(a)

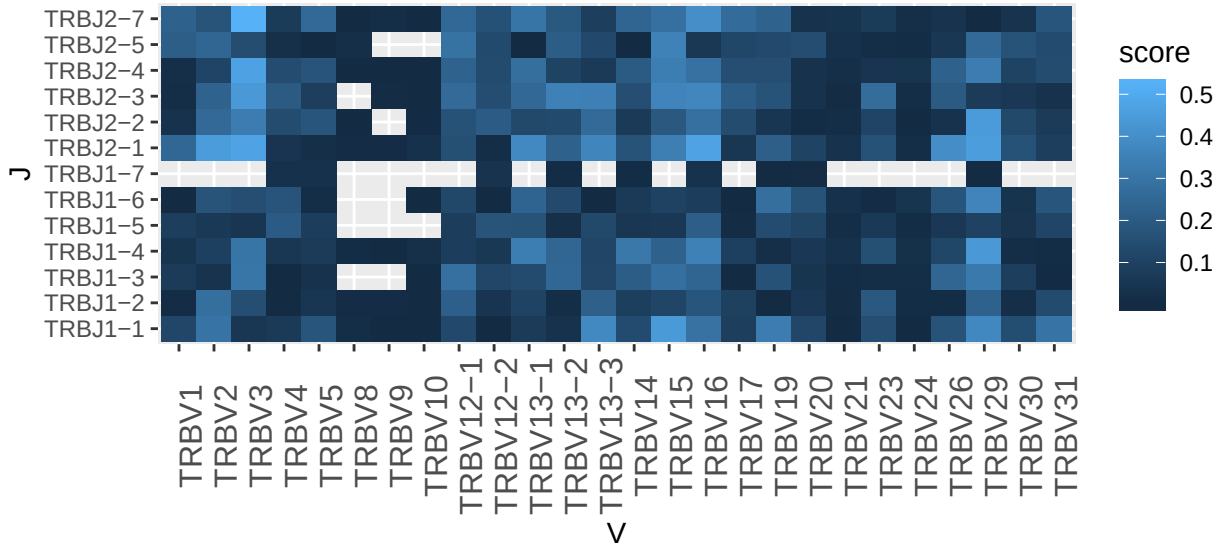

(b)

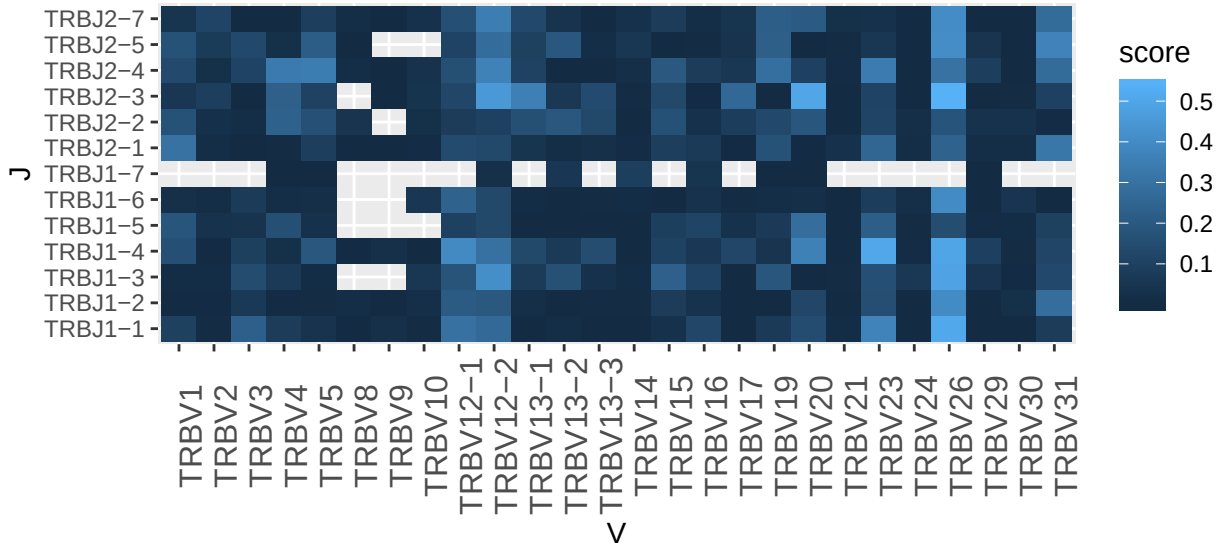

Figure 3.8: Quality of representation by (a) PC1 and (b) PC2 obtained from PCA of VJ gene usage in TCRβ.

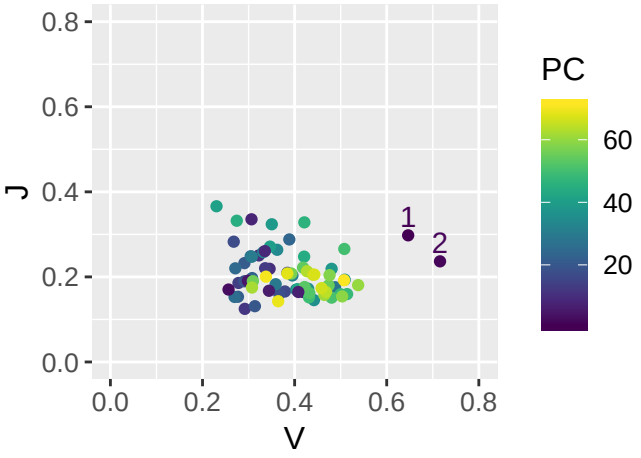

Figure 3.9: The correlation ratios of V and J genes for quality of representation by PCs. The numbers were explicitly shown for PC1 and PC2.

at the same probability by irradiation. Thus, this suggests that whether thymocytes can survive and proliferate after irradiation depends on their CDR3s.

3.4 Discussion

We found that the TCRα combination of TRAV11D, TRAJ18, and CVVGDRGSALGRLHF was especially abundant in the normal CD4$^+$SP cells and the abundance temporally got decreased after irradiation. Invariant natural killer T (iNKT) cells are known to express only this combination of the TCRα chain [93]. While conventional T cells recognize peptide antigens on the MHC [25, 81], iNKT cells recognize glycolipid antigens on CD1d, an MHC-class-I-like molecule [26]. Further, positive selection of iNKT cells in the thymus requires antigen presentation by DP thymocytes [26], not by TECs or DCs. This difference between iNKT cells and conventional T cells is coincident with our results. We observed that the combinations of CVVGDRGSALGRLHF with other V and J genes, or similar CDR3s were not abundant, contrary to our expectation that similar CDR3 sequences show similar abundance. This irrelevance of CDR3 similarity to its abundance might be because immature iNKT cells uniquely express the abundant TCRα chain, and they go through different selection and differentiation processes than other thymocytes. We also observed that the abundance of the iNKT cell-specific TCRα chain had not recovered on day 11, while rank-size distributions except that chain recovered faster. This slower recovery might be because iNKT selection

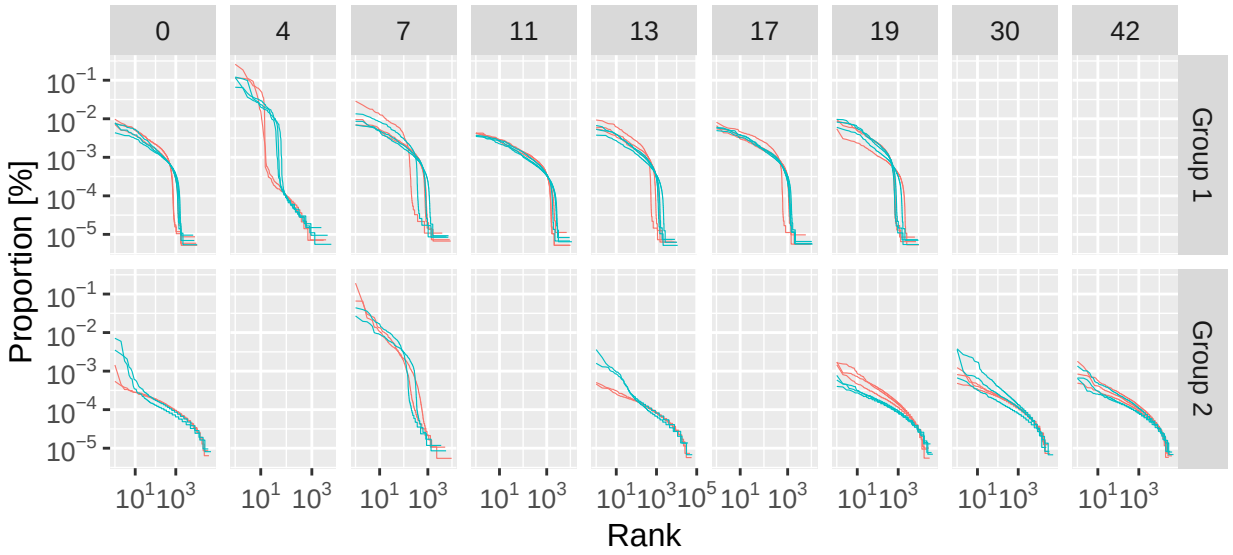

Figure 3.10: Rank size distribution of TCRβ CDR3 in DP (pink) and SP (cyan) cells. The numbers at the head indicate the day after irradiation.

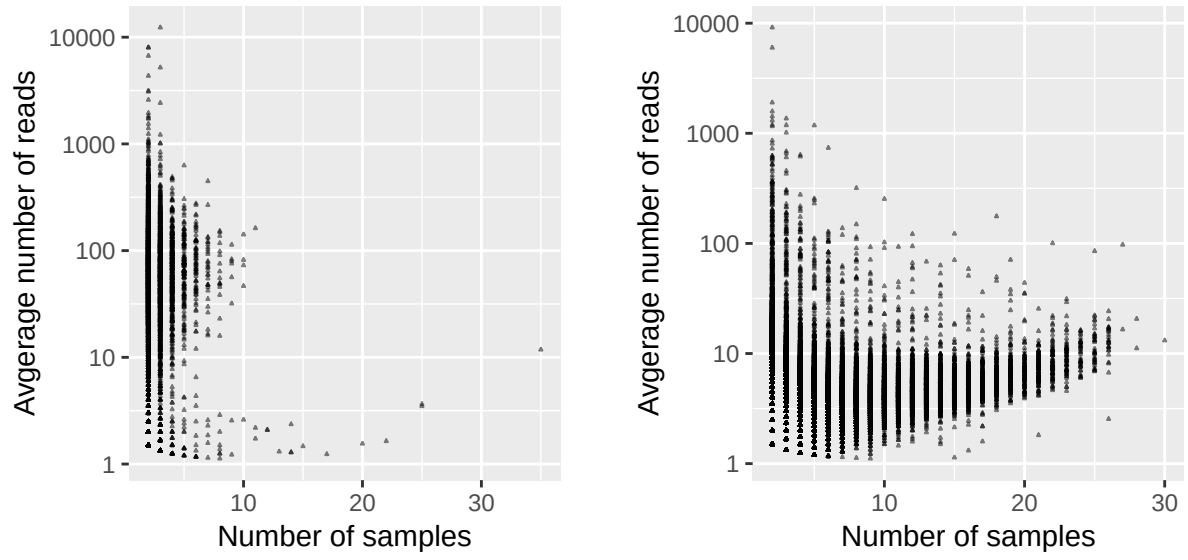

(a) (b)

Figure 3.11: Correlation between commonality and abundance of CDR3s in (a) group 1 and (b) group 2. The horizontal axis represents the number of samples in which each CDR3 sequence was observed. The vertical axis represents the average number of CDR3 reads in the observed samples. CDR3s that were observed in 2 or more samples and the average read number of which were more than 1 are shown.

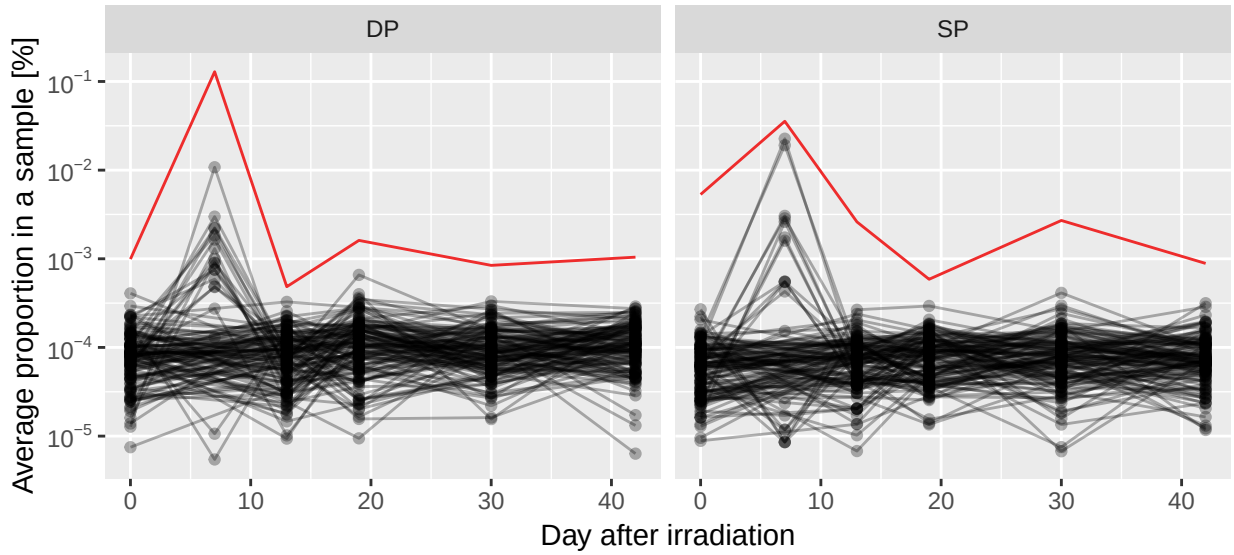

Figure 3.12: Change of average proportions of the most common and abundant 130 CDR3s in group 2. Red lines represent average proportion of the most abundant CDR3s at each day.

was a DP-dependent process. The recovery of the DP cell population also took more than ten days in our analysis of population dynamics (Chapter 2).

In the analysis of TCRβ chain, we characterized the effect of irradiation and negative selection on VJ usage by the first and second principal components of PCA, respectively. Both of PC1 and PC2 were more correlated with V genes than J genes. The correlation of PC1, which represented the effect of negative selection, to V genes suggested that V genes contributed to peptide reactivity of the TCR more than J genes, because negative selection is the process that eliminates TCRs that react to self-peptides. On the other hand, the correlation of PC2, which represented the effect of irradiation, to V genes suggested that tolerance of thymocytes to irradiation may depend on their V gene usage of the TCR. This suggestion of TCR-dependent radiation tolerance coincided with our finding that the proportions of some TCRβ CDR3s got higher after irradiation. Radiation tolerance may be realized by survival from or proliferation after irradiation. Together with the finding of the temporal increase in the proliferation rate of DP cells (Chapter 2), we should investigate each relationship of the survival and proliferation ability to CDR3s.

To summarize, our work has provided various aspects of TCR repertoire recovery from perturbation by comparing the time course of the repertoire change. These results will serve as a starting point of the forthcoming detail study of each aspect.

Chapter 4

Mathematical modeling of intracellular signaling for thymocyte differentiation

4.1 Introduction

Lineage choice of thymocytes between $CD4^+$ helper and $CD8^+$ cytotoxic T cell has been studied as it is a tractable system of the epigenetic bi-potential cell fate decisions [32].

The molecular mechanisms underlying the lineage choice is currently best described by the kinetic signaling model [73]. TCR signal first suppresses CD8 expression of DP thymocytes regardless of their subsequent lineage choices. If the suppression of CD8 ceases the TCR signaling because of the TCR dependency to CD8, signals from cytokines such as IL-7 are allowed to induce re-expression of CD8 for the CD8-lineage fate, otherwise continuous TCR signal specifies the CD4-lineage fate.

Among the lineage choice, the duration of differentiation to $CD8^+$SP cells is suggested to be constant [37]; although the duration of the CD8 suppression from DP varies between clones depending on their TCRs, the duration of CD8 recovery compensate the variation, and as a result, the total differentiation duration from DP to $CD8^+$SP holds constant.

A mathematical model is useful to understand and to extract general laws from these dynamical regulations of intracellular signaling. Mathematical concepts of intracellular signaling derived from the study of other species such as adaptation [21] can indeed explain some aspects of the differentiation of thymocytes. Adaptation is a process where a system initially responds to a stimulus and subsequently returns to original or nearly original levels of activity after a certain amount of time. The expression level of CD8 during differentiation from DP to $CD8^+$SP shows adaptation; the CD8 expression decreases by TCR signal at first, but then gets recovered by IL-7.

Despite the relevance of the thymocyte differentiation to mathematical modeling, any mathematical models have not yet been proposed. In this study, we explore mathematical modeling of intracellular signaling during thymocyte differentiation from DP to $CD8^+$SP with a focus on the mechanism of differentiation for the constant duration by compensatory recovery.

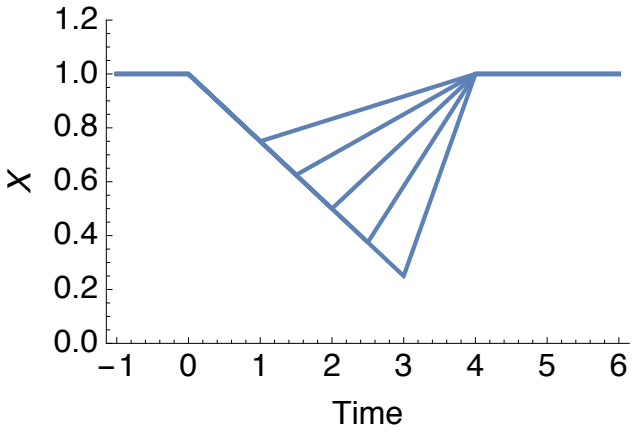

Figure 4.1: Schematic trajectories of the constant response duration by compensatory recovery.

4.2 Result

4.2.1 Setting

Our goal is to construct a mathematical model of intracellular signaling of the thymocyte differentiation in which the duration that an output of a system returns to the original level after response to a stimulus is constant even though the time to reach the peak of transient response varies (Fig. 4.1).

However, the comprehensive regulatory network of the molecules associated with the thymocyte differentiation remains elusive. Therefore, we do not model the regulatory relationship among the molecules. Instead, we model the relationship between representative groups of the molecules to keep the number of variables in the model minimum. The minimum model allows us to succinctly understand the mechanism of the constant response duration by compensatory recovery.

We first introduce input and output variables, x and I as a setting of the model construction. The input $I(t)$ represents the TCR signal strength at time t. After the V(D)J recombination, the TCR signal starts to be transmitted to begin differentiation of thymocytes from DP to SP. Because CD5 expression level which correlated to the TCR signal strength was varied

depending on TCRs [37, 84], we model the input as

$$I(t) = \begin{cases} 1 & \text{for } t < 0 \\ I_{\text{on}} & \text{for } 0 \leq t \end{cases} , \tag{4.1}$$

where $I_{\text{on}} > 1$ is a parameter of the signal strength. We set the initial value $I(t) = 1$ for $t < 0$ for simplicity, but we can transform $I(t)$ so that $I(t) = 0$ for $t < 0$ to represents the event that TCR turns signal on. The output $x(t)$ represents an expression level of CD8 at time t. We assume degradation of CD8 at a constant rate. With a time-dependent expression rate $\phi(t)$, the dynamics of the output is written as

$$\frac{\mathrm{d}x}{\mathrm{d}t} = \phi(t) - x \ , \tag{4.2}$$

and we set the initial condition $x(t) = 1$ for $t < 0$ for simplicity. We derive a signaling model that governs the expression rate $\phi(t)$ given the input (Eq.(4.1)) so that the output $x(t)$ shows the constant response duration by compensatory recovery.

4.2.2 Model Construction

The main factors that control the CD8 expression are the TCR and IL-7 signals. The TCR signal represses CD8 through ThPOK. This leads to the transient decline of the CD8 expression during differentiation. We assume that the CD8 expression rate is proportional to the inverse of the TCR signal strength. On the other hand, the IL-7 signal induces the CD8 re-expression. Thus, we introduce a variable $y(t)$ that represents the IL-7 signal, and assume that the CD8 expression rate is proportional to a certain function of y, denoted as $\phi_{\text{int}}(y)$ for the moment;

$$\frac{\mathrm{d}x}{\mathrm{d}t} = \frac{\phi_{\text{int}}(y(t))}{I(t)} - x \ . \tag{4.3}$$

To determine the form of $\phi_{\text{int}}(y)$ and a model of $y(t)$, we start from considering the simplest case of $\phi_{\text{int}}(y(t))$;

$$\phi_{\text{int}}(y(t)) = \begin{cases} 1 & \text{for } t < t_{\text{sw}} \\ y_{\text{on}} & \text{for } t_{\text{sw}} \leq t \end{cases} , \tag{4.4}$$

and derive the relation of $y_{\rm on}$ and $t_{\rm sw}$ to $I_{\rm on}$ as follows. With Eqs. (4.1) and (4.4), the model of x (Eq.(4.3)) is

$$\frac{\mathrm{d}x}{\mathrm{d}t} = \begin{cases} 1-x & \text{for } t<0 \\ \frac{1}{I_{\rm on}}-x & \text{for } 0 \le t < t_{\rm sw} \\ \frac{y_{\rm on}}{I_{\rm on}}-x & \text{for } t_{\rm sw} \le t \end{cases} . \tag{4.5}$$

For this model (Eq.(4.5)) to show the constant response duration by compensatory recovery, $t_{\rm sw}$ and $y_{\rm on}$ need to be a function of $I_{\rm on}$ such that $x(t_{\rm sw})$ is a decreasing function of $t_{\rm sw}$ and there is a time $t_{\rm en} > t_{\rm sw}$ where $x(t_{\rm en}) = 1$ independently from $I_{\rm on}$ and $t_{\rm sw}$. Because the solutions of Eq.(4.5) at the time $t_{\rm sw}$ and $x(t_{\rm en})$ are

$$x(t_{\rm sw}) = \frac{1}{I_{\rm on}} + e^{-t_{\rm sw}}\left(1-\frac{1}{I_{\rm on}}\right) , \tag{4.6}$$

and

$$x(t_{\rm en}) = \frac{y_{\rm on}}{I_{\rm on}} + e^{-(t_{\rm en}-t_{\rm sw})}\left(x(t_{\rm sw})-\frac{y_{\rm on}}{I_{\rm on}}\right) , \tag{4.7}$$

respectively, the relation between $y_{\rm on}$, $t_{\rm sw}$, and $I_{\rm on}$ for the model (Eq.(4.5)) to pass a point $(t_{\rm en}, 1)$ is,

$$y_{\rm on} = \frac{e^{-t_{\rm en}+t_{\rm sw}} + e^{-t_{\rm en}}(I_{\rm on}-1) - I_{\rm on}}{-1+e^{-t_{\rm en}+t_{\rm sw}}} . \tag{4.8}$$

By assuming $I_{\rm on} = e^{t_{\rm sw}}$ which is the same as $I(t) = e^{t_{\rm sw}}$ for $t > 0$ so that the relation Eq.(4.8) gets simplified and $t_{\rm sw} = 0$ when $I_{\rm on} = 1$, we obtain

$$y_{\rm on}(t_{\rm sw}) = \frac{-1+2e^{t_{\rm sw}} - e^{t_{\rm en}+t_{\rm sw}}}{-e^{t_{\rm en}}+e^{t_{\rm sw}}} . \tag{4.9}$$

By taking the derivative of $y_{\rm on}$ by $t_{\rm sw}$ of Eq.(4.9), and substituting y to $y_{\rm on}$ and t to $t_{\rm sw}$, we derive the differential equation of y that satisfies $y(t_{\rm sw}) = y_{\rm on}$ for any $t_{\rm sw}$;

$$\frac{\mathrm{d}y}{\mathrm{d}t} = \frac{(-2+e^{t_{\rm en}}+y)(-1+e^{t_{\rm en}}y)}{(-1+e^{t_{\rm en}})^2} . \tag{4.10}$$

We modify Eq.(4.10) for $y_{\rm on}$ to be a fixed point;

$$\frac{\mathrm{d}y}{\mathrm{d}t} = \frac{(-2+e^{t_{\rm en}}+y)(-1+e^{t_{\rm en}}y)}{(-1+e^{t_{\rm en}})^2}\left(\frac{2}{1+(\frac{y}{y_{\rm on}(I)})^n}-1\right) , \tag{4.11}$$

where n is a nonlinearity parameter and $y_{\rm on}(I)$ is an increasing function of I obtained by

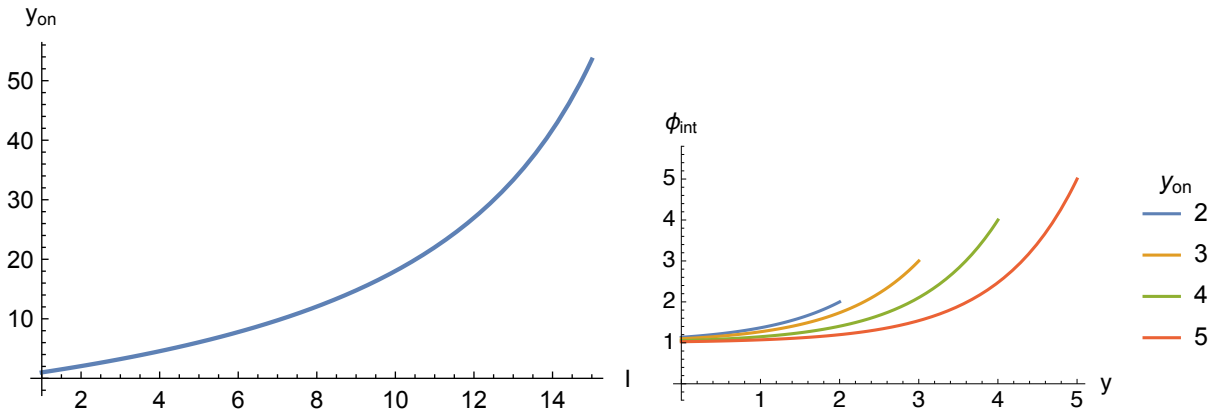

(a) (b)

Figure 4.2: The relationship between the parameters in the model. (a) $y_{\rm on}$, the stable value of y, is an increasing function of I in Eq. (4.12). (b) $\phi_{\rm int}$ is an increasing function of y whereas $y_{\rm on}$ suppresses $\phi_{\rm int}$ in Eq. (4.13).

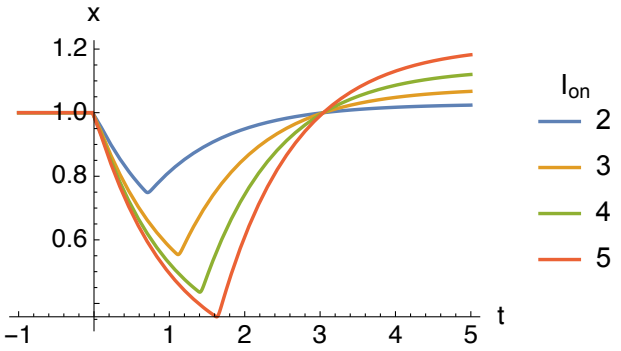

Figure 4.3: Trajectories of $x(t)$ of Eq.(4.3) depending on $I_{\rm on}$ with other variables given by Eqs. (4.1) and (4.11) to (4.13), and parameters $n = 100$ and $t_{\rm en} = 3$.

substituting $t_{\rm sw} = \log I(t)$ to Eq.(4.8) (Fig. 4.2a);

$$y_{\rm on}(I) = \frac{-1 + 2I(t) - e^{t_{\rm en}} I(t)}{-e^{t_{\rm en}} + I(t)} \ . \tag{4.12}$$

Finally, we devise a function with a nonlinear parameter n so that the limit of the function is Eq.(4.4) as n approaches ∞,

$$\phi_{\rm int}(y) = (y_{\rm on} - 1)e^{n(y - y_{\rm on})} + 1 \ , \tag{4.13}$$

where $y_{\rm on}$ acts as a parameter that suppresses the output (Fig. 4.2b).

Although the duration of the obtained model to reach the original value is constant, the stable value of x is not the same as $x(0)$ (Fig. 4.3). Therefore, we introduce an another

variable z biological interpretation of which is discussed later, to regulate x;

$$\frac{\mathrm{d}x}{\mathrm{d}t} = \frac{\phi_{\mathrm{int}}(y(t))}{I(t)\phi_{\mathrm{int}}(z(t))} - x \ . \tag{4.14}$$

We construct a model of z which satisfies

$$\phi_{\mathrm{int}}(z(t)) = \begin{cases} 1 & \text{for } t < t_{\mathrm{en}} \\ z_{\mathrm{on}} & \text{for } t_{\mathrm{en}} \leq t \end{cases} \tag{4.15}$$

as n approaches ∞ in ϕ_{int} where $z_{\mathrm{on}} = y_{\mathrm{on}}/I_{\mathrm{on}}$ such that

$$\frac{\mathrm{d}x}{\mathrm{d}t} = 1 - x \ \text{ for } t_{\mathrm{en}} \leq t \ , \tag{4.16}$$

independent from I_{on}. To satisfy Eq. (4.15), it is required that a stable value of $z(t)$ is z_{on} and that the time to reach the stable value is t_{en}. For the model

$$\frac{\mathrm{d}z}{\mathrm{d}t} = a - z \ , \tag{4.17}$$

the time T that takes for z to reach z_{on} from $z = 1$ is

$$T = \log \frac{a-1}{a - z_{\mathrm{on}}} \ . \tag{4.18}$$

Therefore, in order for T to be t_{en} independently from z_{on}, a as a function of z_{on} and t_{en} is derived by substituting t_{en} to T in Eq. (4.18);

$$a = \frac{z_{\mathrm{on}} e^{t_{\mathrm{en}}} - 1}{e^{t_{\mathrm{en}}} - 1} \ . \tag{4.19}$$

Finally, we should add a revision term $\theta(t)$ in Eq. (4.17) so that z_{on} is the stable value for any a;

$$\frac{\mathrm{d}z}{\mathrm{d}t} = a - z + \theta(t) \ , \tag{4.20}$$

where $\theta(t)$ takes

$$\theta(t) = \begin{cases} 0 & \text{for } z < z_{\mathrm{on}} \\ -a + z_{\mathrm{on}} & \text{for } z = z_{\mathrm{on}} \end{cases} \ , \tag{4.21}$$

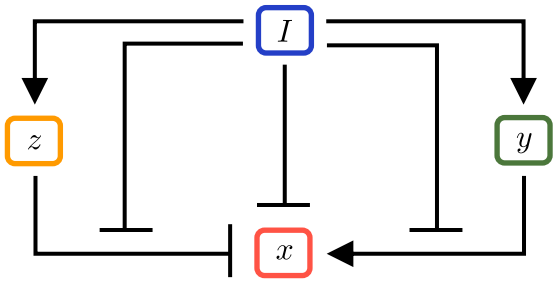

Figure 4.4: Diagram of regulatory network for the constant response duration by compensatory recovery.

so that $\mathrm{d}z/\mathrm{d}t = 0$ for $z = z_{\mathrm{on}}$. We devise a function that satisfy Eq. (4.21) as n approaches ∞;

$$\theta(t) = 2(a - z_{\mathrm{on}}) \left(\frac{1}{1 + (\frac{z}{z_{\mathrm{on}}})^n} - 1 \right) . \tag{4.22}$$

By substituting the obtained a (Eq. (4.19)) and $\theta(t)$ (Eq. (4.22)) to Eq. (4.20), we obtain the model of z;

$$\frac{\mathrm{d}z}{\mathrm{d}t} = z_{\mathrm{on}} - z + \left(\frac{z_{\mathrm{on}} - 1}{e^{t_{\mathrm{en}}} - 1} \right) \left(\frac{2}{1 + (\frac{z}{z_{\mathrm{on}}})^n} - 1 \right) . \tag{4.23}$$

As a whole, the constructed model is;

$$\begin{aligned}
I(t) &= \begin{cases} 1 & \text{for } t < 0 \\ I_{\mathrm{on}} & \text{for } 0 \leq t \end{cases} , \\
\frac{\mathrm{d}x}{\mathrm{d}t} &= \frac{\phi_{\mathrm{int}}(y, y_{\mathrm{on}})}{I(t)\phi_{\mathrm{int}}(z, z_{\mathrm{on}})} - x , \\
\frac{\mathrm{d}y}{\mathrm{d}t} &= \frac{(-2 + e^{t_{\mathrm{en}}} + y)(-1 + e^{t_{\mathrm{en}}} y)}{(-1 + e^{t_{\mathrm{en}}})^2} (\frac{2}{1 + (\frac{y}{y_{\mathrm{on}}})^n} - 1) , \\
\frac{\mathrm{d}z}{\mathrm{d}t} &= z_{\mathrm{on}} - z + (\frac{z_{\mathrm{on}} - 1}{e^{t_{\mathrm{en}}} - 1})(\frac{2}{1 + (\frac{z}{z_{\mathrm{on}}})^n} - 1) , \\
\phi_{\mathrm{int}}(v, v_{\mathrm{on}}) &= (v_{\mathrm{on}} - 1)e^{n(v - v_{\mathrm{on}})} + 1 , \\
y_{\mathrm{on}}(I) &= \frac{1 + (-2 + e^{t_{\mathrm{en}}})I}{e^{t_{\mathrm{en}}} - I} , \\
z_{\mathrm{on}}(I) &= \frac{y_{\mathrm{on}}(I)}{I} ,
\end{aligned} \tag{4.24}$$

with the initial values $x(0) = 1$, $y(0) = 1$, $z(0) = 1$, and the schematic diagram of which is shown in Fig. 4.4.

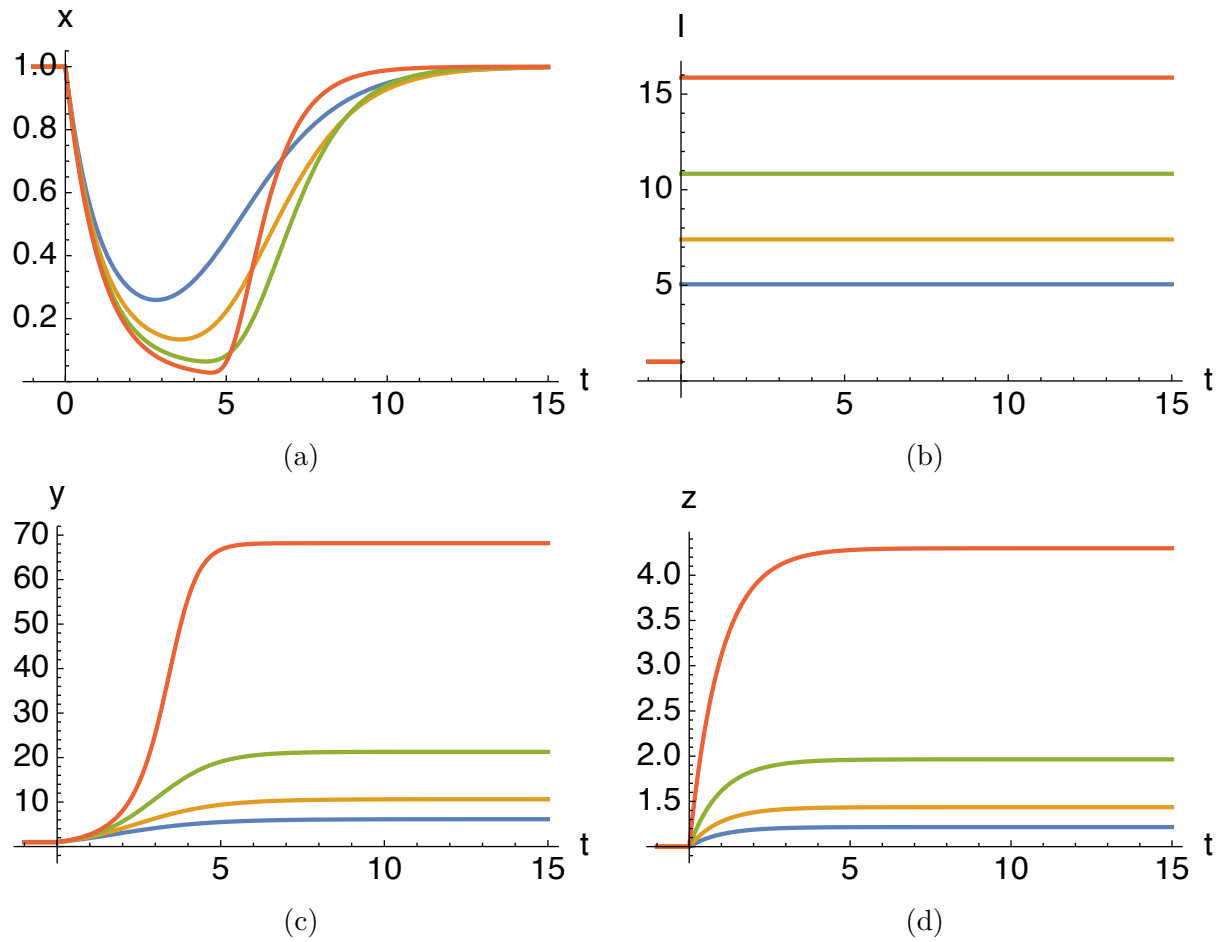

Figure 4.5: Trajectories of the variables (a) x, (b) I, (c) y, and (d) z in the model (Eq. (4.24)) depending on I_{on} with the other parameter values $n = 1$ and $t_{\text{en}} = 3$. Simulations with different I_{on} values are shown in different colors.

4.2.3 Properties of the model

The trajectories of the derived model Eq.(4.24) with the different nonlinearity parameter values $n = 1$ and $n = 100$ are shown in Figs. 4.5 and 4.6 respectively. Regardless of the nonlinearity parameter value, the model output x showed adaptation to the original value. As the input strength I_{on} got higher, the duration where x was declining (phase 1) was prolonged, and the duration where x was increasing (phase 2) was shorten(Fig. 4.7).

4.2.4 Suppression of an indirect regulation is necessary

Because $y_{\text{on}}(I)$ is an increasing function of I (Eq. (4.12) and Fig. 4.2a) and the regulatory effect by y to the x expression rate is downregulated by y_{on} for $y < y_{\text{on}}$ (Eq. (4.13)

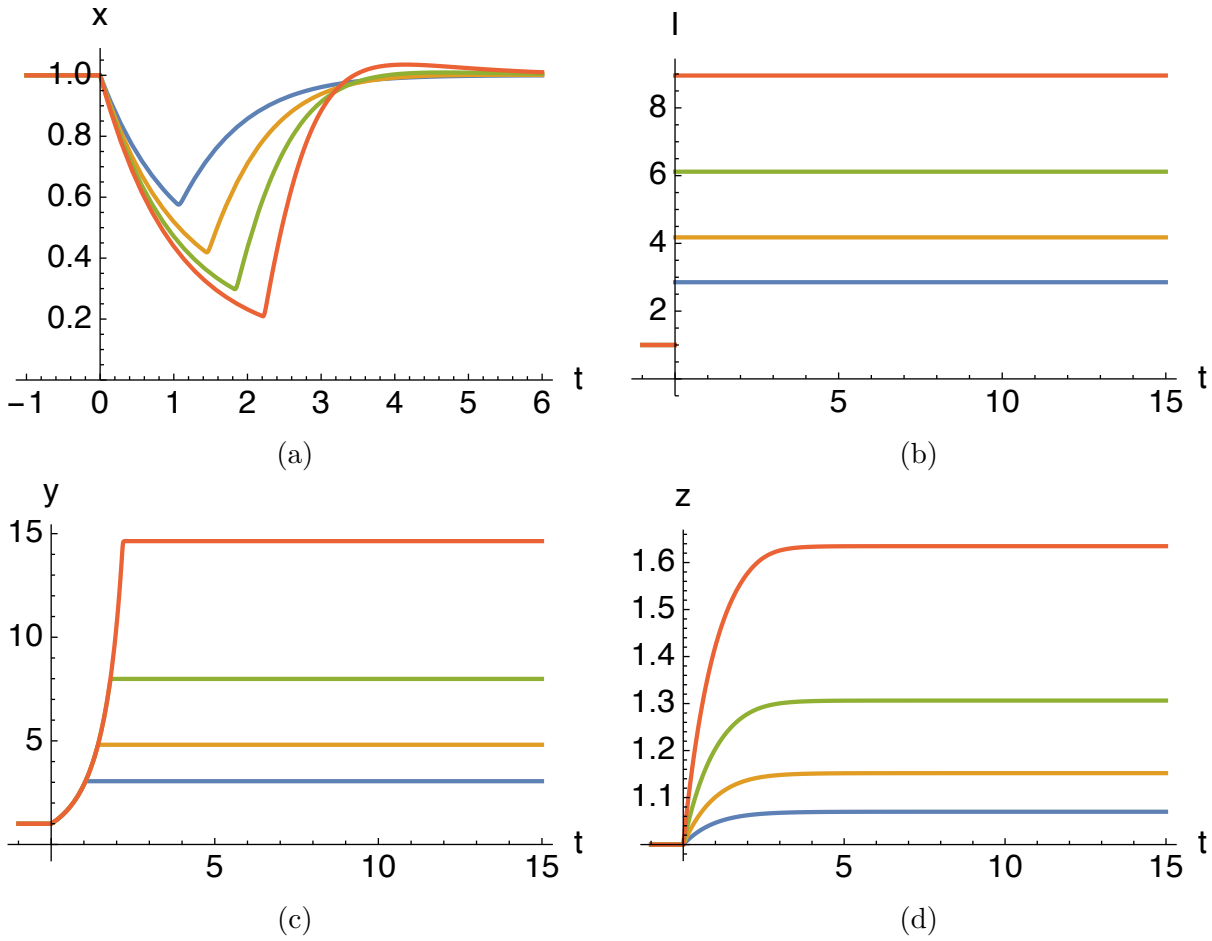

Figure 4.6: Trajectories of the variables (a) x, (b) I, (c) y, and (d) z in the model (Eq. (4.24)) depending on I_{on} with the other parameter values $n = 100$ and $t_{\text{en}} = 3$. Simulations with different I_{on} values are shown in different colors.

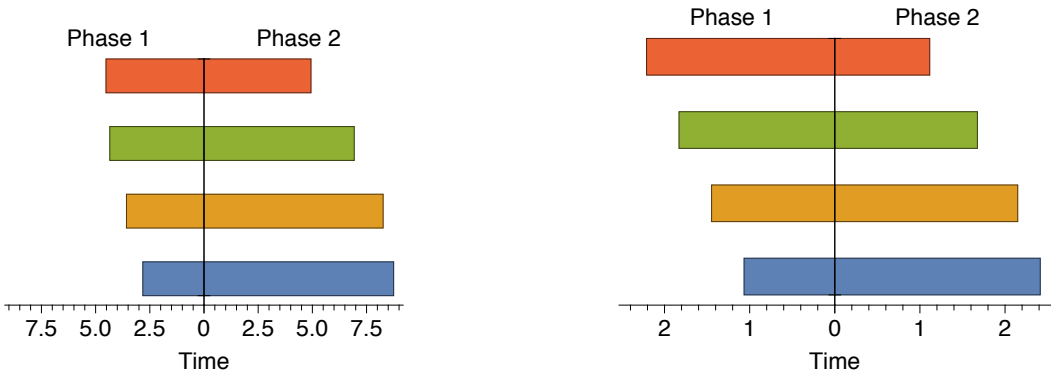

Figure 4.7: Duration time of phase 1 and phase 2 of the model (Eq. (4.24)) with the parameters $t_{\text{en}} = 3$ and (a) $n = 1$ or (b) $n = 100$, where phase 1 is the phase x is decreasing and phase 2 is the phase x is increasing during the transient response to I. Colors in the graphs (a) and (b) represent different I_{on} values and correspond to that of Figs. 4.5 and 4.6, respectively.

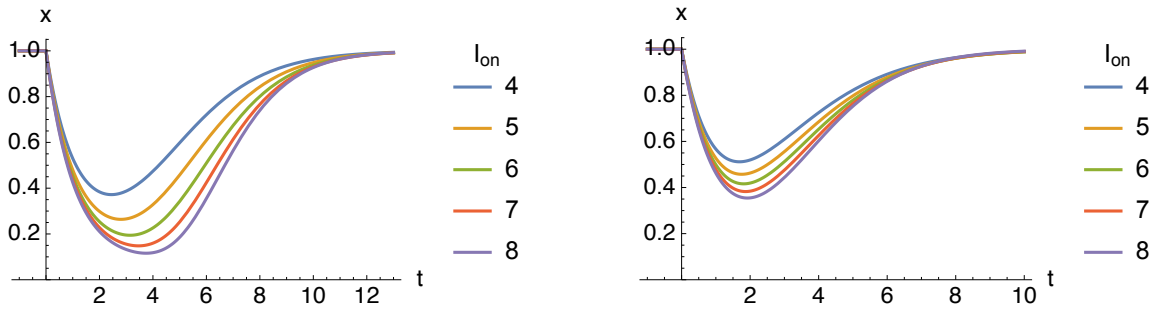

(a) (b)

Figure 4.8: The regulation in which I suppress the x induction by y varies the duration that x decreases. Trajectories of $x(t)$ depending on I_{on} are shown in the model (a) Eq. (4.24) and (b) Eq. (4.24) except $\phi_{\mathrm{int}}(y) = y$. Other parameters are given by $n = 1$ and $t_{\mathrm{en}} = 3$.

and Fig. 4.2b), I has an inhibitory effect on the induction of x by y. This inhibition is critical for the duration compensation. If y solely increases the expression rate of x without the inhibition by I, the duration that x decreases does not vary, because y as well as the expression rate of x increase faster as the input strength I_{on} gets higher (Fig. 4.8). Notably, this inhibition is consistent with the actual intracellular signaling of thymocytes; the TCR signal interrupts the IL-7 signal while the TCR signal upregulates the IL-7 receptor expression [35, 59]. Therefore, substituting $\phi_{\mathrm{int}}(y) = y$ for Eq. (4.13) in Eq. (4.24) corresponds to knocking out the TCR signal-dependent inhibition factors of IL-7 signal, miR-17 and Calpain. From the substitution, the model predicts that, by knocking out the inhibition factors, the duration that CD8 decreases gets constant independently from TCR as indicated in (Fig. 4.8b).

4.3 Discussion

Although the relationship among I, y, and x is consistent with the experimental evidence, z does not have its corresponding molecule. It may be related to molecules of downstream of the TCR signal such as CD5 and Zap70 because the expression level of these molecules positively correlates with the strength or duration of the TCR signal [66, 84]. In our model, z functions to keep the stable value of x to be the same as the original value before the input is on. This functionality may be realized by other regulatory network motifs such as feedback to x or y. To resolve the unclear correspondence, we might have to extend our model to a detailed model based on chemical kinetics.

In our model, I directly inhibits x but promotes x through y. This regulatory network motif is called as an incoherent feedforward loop [52]. Our model has still another regulation that I prevents the induction of x by y and suggests that this regulation is crucial for the constant differentiation duration by compensatory recovery. This network motif and its function should be tested experimentally and might be found in other signaling circuits.

In summary, we constructed a novel mathematical model of intracellular signaling for thymocytes differentiation. Our model focused on the mechanism of the distinctive property of the differentiation that the duration is constant by a compensatory adaptation. We expect our model to evoke experimental verification and exploration of signaling circuits that our model can be applied to.

Chapter 5

Conclusion

In this thesis, we applied mathematical modeling and bioinformatic methods to study homeostatic T cell development. By utilizing the quantitative approaches, we clarified the extent and mechanism of the various homeostatic properties. In Chapter 2, we combined mathematical modeling with time courses of population change in the thymus to reveal intracellular interactions that contribute to maintain the population size of thymocytes and TECs. In Chapter 3, we conducted the high throughput sequencing analysis of TCRs from thymocytes to elucidate how repertoire diversity changes against perturbations. In Chapter 4, we constructed a mathematical model of intracellular signaling during the differentiation of thymocytes to understand the mechanism that controls the duration of differentiation in a compensatory manner.

Our study focused on the temporal change of cell population, TCR repertoire, and intracellular signals during T cell development. There is still room for further exploration of the relationship among these dynamics. It would be of interest to investigate the relationship of the dynamics of thymocytes at the population level to the intracellular signaling and the TCR repertoire diversity. For example, we anticipate that we can estimate the differentiation rate at the population level from the intracellular signaling model during recovery from irradiation. We should also await for study on how TCR dependent variations of cell division and differentiation rate are related to that of the population level.

To tackle these questions, we need experimental methods to measure multiple aspects of T cell development all at once with a time interval of higher resolution, as well as corresponding mathematical models and data analysis methods. Although many systems for real-time observation of T cell development *in vivo* and *in vitro* have been developed [2], it is still impractical to measure multiple features such as expression levels of cell surface markers and TCR sequences simultaneously in real-time.

One of the promising techniques to measure high dimensional data with a short time interval is single-cell RNA sequencing. Many methods called pseudotime analysis, which computationally order cells along differentiation trajectories from the single-cell sequencing data, have been proposed and applied to the T cell differentiation [70]. By employing the pseudotime anlysis, we can estimate the time course of multidimensional gene expression levels. Further, single-cell RNA sequencing allows reading a TCRα and β chains pair [29] for each clone. By developing appropriate mathematical models and data analysis framework to exploit the

single-cell sequencing, we will deepen our understanding of T cell development from the more integrative viewpoint.

In summary, our quantitative studies exploit mathematical modeling and sequence analysis, emerging approaches in immunology, to deepen understanding of the mechanisms of the homeostasis in the thymus. We anticipate that our studies have a pivotal impact on future directions for research to reveal mechanisms of the immunological systems.

Bibliography

[1] Jakub Abramson and Graham Anderson. "Thymic epithelial cells". In: *Annual Review of Immunology* 35.1 (2017), pp. 85–118.

[2] Narges Aghaallaei and Baubak Bajoghli. "Making Thymus Visible: Understanding T-Cell Development from a New Perspective". In: *Frontiers in Immunology* 9 (2018), p. 375.

[3] Iren Bains, Hisse M van Santen, Benedict Seddon, and Andrew J Yates. "Models of Self-Peptide Sampling by Developing T Cells Identify Candidate Mechanisms of Thymic Selection". In: *PLoS computational biology* 9.7 (2013), e1003102.

[4] Thomas Boehm and Jeremy B Swann. "Thymus involution and regeneration: two sides of the same coin?" In: *Nature Reviews Immunology* 13 (2013), pp. 831–838.

[5] Nathalie Bosc and Marie-Paule Lefranc. "The Mouse (*Mus musculus*) T Cell Receptor Beta Variable (TRBV), Diversity (TRBD) and Joining (TRBJ) Genes". In: *Experimental and Clinical Immunogenetics* 17.4 (2000), pp. 216–228.

[6] Philip Bradley and Paul G Thomas. "Using T Cell Receptor Repertoires to Understand the Principles of Adaptive Immune Recognition". In: *Annual Review of Immunology* 37.1 (2019), pp. 547–570.

[7] Elise R Breed, Masashi Watanabe, and Kristin A Hogquist. "Measuring Thymic Clonal Deletion at the Population Level". In: *The Journal of Immunology* 202.11 (2019), pp. 3226–3233.

[8] Marcel R M van den Brink, Önder Alpdogan, and Richard L Boyd. "Strategies to enhance T-cell reconstitution in immunocompromised patients". In: *Nature Reviews Immunology* 4.11 (2004), pp. 856–867.

[9] Anna Q Cai, Kerry A Landman, Barry D Hughes, and Colleen M Witt. "T cell development in the thymus: From periodic seeding to constant output". In: *Journal of Theoretical Biology* 249.2 (2007), pp. 384–394.

[10] Andrea C Carpenter and Rémy Bosselut. "Decision checkpoints in the thymus". In: *Nature Immunology* 11.8 (2010), pp. 666–673.

[11] Rod Ceredig and Ton Rolink. "A positive look at double-negative thymocytes". In: *Nature Reviews Immunology* 2.11 (2002), pp. 888–897.

[12] Alessandro Chiarucci, Giovanni Bacaro, and Samuel M Scheiner. "Old and new challenges in using species diversity for assessing biodiversity". In: *Philosophical Transactions of the Royal Society B: Biological Sciences* 366.1576 (2011), pp. 2426–2437.

[13] Mark M W Chong, Ann L Cornish, Rima Darwiche, Edouard G Stanley, Jared F Purton, Dale I Godfrey, Douglas J Hilton, Robyn Starr, Warren S Alexander, and Thomas W H Kay. "Suppressor of Cytokine Signaling-1 Is a Critical Regulator of Interleukin-7-Dependent CD8+ T Cell Differentiation". In: *Immunity* 18.4 (2003), pp. 475–487.

[14] Maria Ciofani and Juan Carlos Zúñiga-Pflücker. "A Survival Guide to Early T Cell Development". In: *Immunologic Research* 34.2 (2006), pp. 117–132.

[15] Maria Ciofani and Juan Carlos Zúñiga-Pflücker. "Notch promotes survival of pre–T cells at the β-selection checkpoint by regulating cellular metabolism". In: *Nature Immunology* 6.9 (2005), pp. 881–888.

[16] Anthony C Davison and David V Hinkley. *Bootstrap Methods and their Application*. 1st ed. Cambridge University Press, 1997.

[17] J A Dudakov et al. "Interleukin-22 drives endogenous thymic regeneration in mice". In: *Science* 336.6077 (2012), pp. 91–95.

[18] Maude Dumont-Lagacé, Hervé Gerbe, Tariq Daouda, Jean-Philippe Laverdure, Sylvie Brochu, Sébastien Lemieux, Étienne Gagnon, and Claude Perreault. "Detection of quiescent radioresistant epithelial progenitors in the adult thymus". In: *Frontiers in Immunology* 8 (2017), pp. 3102–13.

[19] M Egerton, R Scollay, and K Shortman. "Kinetics of mature T-cell development in the thymus". In: *Proceedings of the National Academy of Sciences* 87.7 (1990), pp. 2579–2582.

[20] Yuval Elhanati, Anand Murugan, Curtis G Callan Jr., Thierry Mora, and Aleksandra M Walczak. "Quantifying selection in immune receptor repertoires". In: *Proceedings of the National Academy of Sciences* 111.27 (2014), pp. 9875–9880.

[21] James E Ferrell Jr. "Perfect and Near-Perfect Adaptation in Cell Signaling". In: *Cell Systems* 2.2 (2016), pp. 62–67.

[22] Emma Fiorini, Isabel Ferrero, Estelle Merck, Stéphanie Favre, Michel Pierres, Sanjiv A Luther, and H Robson MacDonald. "Cutting edge: thymic crosstalk regulates delta-like 4 expression on cortical epithelial cells." In: *The Journal of Immunology* 181.12 (2008), pp. 8199–8203.

[23] Idoia Gimferrer, Taishan Hu, Amie Simmons, Chi Wang, Abdallah Souabni, Meinrad Busslinger, Timothy P Bender, Gabriela Hernandez-Hoyos, and José Alberola-Ila. "Regulation of GATA-3 Expression during CD4 Lineage Differentiation". In: *The Journal of Immunology* 186.7 (2011), pp. 3892–3898.

[24] V Giudicelli. "IMGT/GENE-DB: a comprehensive database for human and mouse immunoglobulin and T cell receptor genes". In: *Nucleic Acids Research* 33.Database issue (2004), pp. D256–D261.

[25] Jacob Glanville et al. "Identifying specificity groups in the T cell receptor repertoire". In: *Nature* 547.7661 (2017), pp. 94–98.

[26] Dale I Godfrey and Stuart P Berzins. "Control points in NKT-cell development". In: *Nature Reviews Immunology* 7.7 (2007), pp. 505–518.

[27] D H D Gray, N Seach, T Ueno, M K Milton, A Liston, A M Lew, C C Goodnow, and R L Boyd. "Developmental kinetics, turnover, and stimulatory capacity of thymic epithelial cells". In: *Blood* 108.12 (2006), pp. 3777–3785.

[28] Amanda L Gruver and Gregory D Sempowski. “Cytokines, leptin, and stress-induced thymic atrophy”. In: *Journal of Leukocyte Biology* 84.4 (2008), pp. 915–923.

[29] Arnold Han, Jacob Glanville, Leo Hansmann, and Mark M Davis. “Linking T-cell receptor sequence to functional phenotype at the single-cell level”. In: *Nature Biotechnology* 32.7 (2014), pp. 684–692.

[30] Mayumi Hirakawa, Daisuke Nagakubo, Benoamp x000EE t Kanzler, Sergiy Avilov, Brigitte Krauth, Christiane Happe, Jeremy B Swann, Anja Nusser, and Thomas Boehm. “Fundamental parameters of the developing thymic epithelium in the mouse”. In: *Scientific Reports* (2018), p. 11095.

[31] François Husson, Jérome Pagès, and Sébastien Lê. *Exploratory Multivariate Analysis by Example Using R*. Chapman & Hall/CRC Computer Science & Data Analysis. CRC Press Taylor & Francis, 2010, p. 240.

[32] Priya D A Issuree, Charles P Ng, and Dan R Littman. “Heritable Gene Regulation in the CD4:CD8 T Cell Lineage Choice”. In: *Frontiers in Immunology* 8.1 (2017), p. 291.

[33] Ian T Jolliffe. *Principal Component Analysis*. Springer Series in Statistics. New York: Springer-Verlag, 2002.

[34] Kazumasa B Kaneko, Ryosuke Tateishi, Takahisa Miyao, Yuki Takakura, Nobuko Akiyama, Ryo Yokota, Taishin Akiyama, and Tetsuya J Kobayashi. “Quantitative analysis reveals reciprocal regulations underlying recovery dynamics of thymocytes and thymic environment in mice”. In: *Communications Biology* 2 (2019), p. 444.

[35] G Katz, L A Pobezinsky, S Jeurling, M Shinzawa, F Van Laethem, and A Singer. “T cell receptor stimulation impairs IL-7 receptor signaling by inducing expression of the microRNA miR-17 to target Janus kinase 1”. In: *Science Signaling* 7.340 (2014), ra83.

[36] John F Kenney and E. S. Keeping. *Mathematics of statistics*. Vol. 1. Van Nostrand company, 1954.

[37] Motoko Y Kimura, Julien Thomas, Xuguang Tai, Terry I Guinter, Miho Shinzawa, Ruth Etzensperger, Zhenhu Li, Paul Love, Toshinori Nakayama, and Alfred Singer. “Timing and duration of MHC I positive selection signals are adjusted in the thymus to prevent lineage errors”. In: *Nature Immunology* 17.12 (2016), pp. 1415–1423.

[38] Ludger Klein, Maria Hinterberger, Gerald Wirnsberger, and Bruno Kyewski. “Antigen presentation in the thymus for positive selection and central tolerance induction”. In: *Nature Reviews Immunology* 9.12 (2009), pp. 833–844.

[39] Ludger Klein, Bruno Kyewski, Paul M Allen, and Kristin A Hogquist. “Positive and negative selection of the T cell repertoire: what thymocytes see (and don’t see)”. In: *Nature Reviews Immunology* 14.6 (2014), pp. 377–391.

[40] D B Klug, C Carter, E Crouch, D Roop, C J Conti, and E R Richie. “Interdependence of cortical thymic epithelial cell differentiation and T-lineage commitment”. In: *Proceedings of the National Academy of Sciences* 95.20 (1998), pp. 11822–11827.

[41] Ute Koch and Freddy Radtke. “Mechanisms of T Cell Development and Transformation”. In: *Annual Review of Cell and Developmental Biology* 27.1 (2011), pp. 539–562.

[42] Andreas Krueger, Natalia Ziętara, and Marcin Łyszkiewicz. “T cell development by the numbers”. In: *Trends in Immunology* 38.2 (2017), pp. 128–139.

[43] Hanjie Li et al. “Recombinatorial Biases and Convergent Recombination Determine Interindividual TCRβ Sharing in Murine Thymocytes”. In: *The Journal of Immunology* 189.5 (2012), pp. 2404–2413.

[44] Jinbo Li. “X-ray irradiation selectively kills thymocytes of different stages and impairs the maturation of donor-derived CD4+CD8+ thymocytes in recipient thymus”. In: *Journal of Biomedical Research* 26.5 (2012), pp. 355–364.

[45] Zhou Li, Ma Long, Liu ChunMei, Shi Bin, Yu Jiang, Ma Rui, Ma Qingqing, and Yao XinSheng. “Composition and variation analysis of TCR β-chain CDR3 repertoire in the thymus and spleen of MRL/lpr mouse at different ages”. In: *Immunogenetics* 67.1 (2014), pp. 25–37.

[46] Noëlla Lopes, Arnauld Sergé, Pierre Ferrier, and Magali Irla. “Thymic Crosstalk Coordinates Medulla Organization and T-Cell Tolerance Induction”. In: *Frontiers in Immunology* 6.12 (2015), pp. 383–13.

[47] Jinghua Lu et al. “Molecular constraints on CDR3 for thymic selection of MHC-restricted TCRs from a random pre-selection repertoire”. In: *Nature Communications* 10 (2019), p. 1019.

[48] Megan A Luckey, Motoko Y Kimura, Adam T Waickman, Lionel Feigenbaum, Alfred Singer, and Jung-Hyun Park. “The transcription factor ThPOK suppresses Runx3 and imposes CD4+ lineage fate by inducing the SOCS suppressors of cytokine signaling”. In: *Nature Immunology* 15.7 (2014), pp. 638–645.

[49] Grant Lythe, Robin E Callard, Rollo L Hoare, and Carmen Molina-París. “How many TCR clonotypes does a body maintain?” In: *Journal of Theoretical Biology* 389.C (2016), pp. 214–224.

[50] Robert J Mallis et al. “Pre-TCR ligand binding impacts thymocyte development before $\alpha\beta$TCR expression”. In: *Proceedings of the National Academy of Sciences* 112.27 (2015), pp. 8373–8378.

[51] Erica Manesso, Vijay Chickarmane, Hao Yuan Kueh, Ellen V Rothenberg, and Carsten Peterson. “Computational modelling of T-cell formation kinetics: output regulated by initial proliferation-linked deferral of developmental competence.” In: *Journal of The Royal Society Interface* 10.78 (2013), pp. 20120774–20120774.

[52] S Mangan and U Alon. “Structure and function of the feed-forward loop network motif”. In: *Proceedings of the National Academy of Sciences* 100.21 (2003), pp. 11980–11985.

[53] D Maraninchi et al. “Impact of T-cell depletion on outcome of allogeneic bone-marrow transplantation for standard-risk leukaemias”. In: *The Lancet* 330.8552 (1987), pp. 175–178.

[54] Vera C Martins, Eliana Ruggiero, Susan M Schlenner, Vikas Madan, Manfred Schmidt, Pamela J Fink, Christof von Kalle, and Hans-Reimer Rodewald. “Thymus-autonomous T cell development in the absence of progenitor import”. In: *The Journal of Experimental Medicine* 209.8 (2012), pp. 1409–1417.

[55] Ramit Mehr, Amiela Globerson, and Alan S Perelson. “Modeling positive and negative selection and differentiation processes in the thymus”. In: *Journal of Theoretical Biology* 175.1 (1995), pp. 103–126.

[56] Todd C Metzger, Imran S Khan, James M Gardner, Maria L Mouchess, Kellsey P Johannes, Anna K Krawisz, Katarzyna M Skrzypczynska, and Mark S Anderson. "Lineage Tracing and Cell Ablation Identify a Post-Aire-Expressing Thymic Epithelial Cell Population". In: *Cell Reports* 5.1 (2013), pp. 166–179.

[57] Erick Moen, Dylan Bannon, Takamasa Kudo, William Graf, Markus Covert, and David Van Valen. "Deep learning for cellular image analysis". In: *Nature Methods* (2019), pp. 1–14.

[58] Radu Dumitru Moleriu, Daniela Zaharie, Lavinia Cristina Moatar-Moleriu, Alexandra Teodora Gruia, Ani Aurora Mic, and Felix Aurel Mic. "Insights into the mechanisms of thymus involution and regeneration by modeling the glucocorticoid-induced perturbation of thymocyte populations dynamics". In: *Journal of Theoretical Biology* 348.c (2014), pp. 80–99.

[59] M Noguchi, A Sarin, M J Aman, H Nakajima, E W Shores, P A Henkart, and W J Leonard. "Functional cleavage of the common cytokine receptor chain (c) by calpain". In: *Proceedings of the National Academy of Sciences* 94.21 (1997), pp. 11534–11539.

[60] Jung-Hyun Park et al. "Signaling by intrathymic cytokines, not T cell antigen receptors, specifies CD8 lineage choice and promotes the differentiation of cytotoxic-lineage T cells". In: *Nature Immunology* 11.3 (2010), pp. 257–264.

[61] Robertson Parkman and Kenneth I Weinberg. "Immunological reconstitution following bone marrow transplantation". In: *Immunological Reviews* 157.1 (1997), pp. 73–78.

[62] Douglas S Richardson and Jeff W Lichtman. "Clarifying Tissue Clearing". In: *Cell* 162.2 (2017), pp. 246–257.

[63] Elisa Rosati, C Marie Dowds, Evaggelia Liaskou, Eva Kristine Klemsdal Henriksen, Tom H Karlsen, and Andre Franke. "Overview of methodologies for T-cell receptor repertoire analysis". In: 17 (2017), p. 61.

[64] David B Roth. "V(D)J Recombination: Mechanism, Errors, and Fidelity". In: *Microbiology spectrum* 2.6 (2014).

[65] Jinxiu Rui, Haifeng Liu, Xiaoyan Zhu, Yu Cui, and Xiaolong Liu. "Epigenetic Silencing of Cd8Genes by ThPOK-Mediated Deacetylation during CD4 T Cell Differentiation". In: *The Journal of Immunology* 189.3 (2012), pp. 1380–1390.

[66] Manoj Saini, Charles Sinclair, Daniel Marshall, Mauro Tolaini, Shimon Sakaguchi, and Benedict Seddon. "Regulation of Zap70 expression during thymocyte development enables temporal separation of CD4 and CD8 repertoire selection at different signaling thresholds." In: *Science signaling* 3.114 (2010), ra23. ISSN: 1937-9145.

[67] Mie Sakata, Izumi Ohigashi, and Yousuke Takahama. "Cellularity of Thymic Epithelial Cells in the Postnatal Mouse". In: *The Journal of Immunology* 200.4 (2018), pp. 1382–1388.

[68] David Sancho, Manuel Gómez, and Francisco Sánchez-Madrid. "CD69 is an immunoregulatory molecule induced following activation". In: *Trends in Immunology* 26.3 (2005), pp. 136–140.

[69] Maria Sawicka, Gretta L Stritesky, Joseph Reynolds, Niloufar Abourashchi, Grant Lythe, Carmen Molina-París, and Kristin A Hogquist. "From pre-DP, post-DP, SP4, and SP8 Thymocyte Cell Counts to a Dynamical Model of Cortical and Medullary Selection". In: *Frontiers in Immunology* 5 (2014), p. 19.

[70] Manu Setty, Michelle D Tadmor, Shlomit Reich-Zeliger, Omer Angel, Tomer Meir Salame, Pooja Kathail, Kristy Choi, Sean Bendall, Nir Friedman, and Dana Pe'er. "Wishbone identifies bifurcating developmental trajectories from single-cell data". In: *Nature Biotechnology* 34 (2016), pp. 637–645.

[71] Saba Shakib, Guillaume E Desanti, William E Jenkinson, Sonia M Parnell, Eric J Jenkinson, and Graham Anderson. "Checkpoints in the development of thymic cortical epithelial cells." In: *The Journal of Immunology* 182.1 (2009), pp. 130–137.

[72] Charles Sinclair, Iren Bains, Andrew J Yates, and Benedict Seddon. "Asymmetric thymocyte death underlies the CD4:CD8 T-cell ratio in the adaptive immune system". In: *Proceedings of the National Academy of Sciences* 110.31 (2013), E2905–E2914.

[73] Alfred Singer, Stanley Adoro, and Jung-Hyun Park. "Lineage fate and intense debate: myths, models and mechanisms of CD4- versus CD8-lineage choice". In: *Nature Reviews Immunology* 8.10 (2008), pp. 788–801.

[74] Adrien Six, Maria Encarnita Mariotti-Ferrandiz, Wahiba Chaara, Susana Magadan, Hang-Phuong Pham, Marie-Paule Lefranc, Thierry Mora, Véronique Thomas-Vaslin, Aleksandra M Walczak, and Pierre Boudinot. "The Past, Present, and Future of Immune Repertoire Biology – The Rise of Next-Generation Repertoire Analysis". In: *Frontiers in Immunology* 4 (2013), p. 413.

[75] Yinhong Song, Min Su, Pranau Panchatsharam, Debra Rood, and Laijun Lai. "c-Met signalling is required for efficient postnatal thymic regeneration and repair". In: *Immunology* 144.2 (2015), pp. 245–253.

[76] G L Stritesky, Y Xing, J R Erickson, L A Kalekar, X Wang, D L Mueller, S C Jameson, and K A Hogquist. "Murine thymic selection quantified using a unique method to capture deleted T cells". In: *Proceedings of the National Academy of Sciences* 110.12 (2013), pp. 4679–4684.

[77] Lina Sun, Hongran Li, Haiying Luo, and Yong Zhao. "Thymic epithelial cell development and its dysfunction in human diseases." In: *BioMed Research International* 2014.11 (2014), pp. 206929–14.

[78] Yousuke Takahama. "Journey through the thymus: stromal guides for T-cell development and selection". In: *Nature Reviews Immunology* 6.2 (2006), pp. 127–135.

[79] Yousuke Takahama, Izumi Ohigashi, Song Baik, and Graham Anderson. "Generation of diversity in thymic epithelial cells". In: *Nature Reviews Immunology* 17 (2017), pp. 295–305.

[80] V Thomas-Vaslin, H K Altes, R J de Boer, and D Klatzmann. "Comprehensive assessment and mathematical modeling of t cell population dynamics and homeostasis". In: *The Journal of Immunology* 180.4 (2008), pp. 2240–2250.

[81] Vanessa Venturi, David A Price, Daniel C Douek, and Miles P Davenport. "The molecular basis for public T-cell responses?" In: *Nature Reviews Immunology* 8.3 (2008), pp. 231–238.

[82] Julien Vibert and Véronique Thomas-Vaslin. "Modelling T cell proliferation: Dynamics heterogeneity depending on cell differentiation, age, and genetic background". In: *PLoS computational biology* 13.3 (2017), e1005417.

[83] Christophe Viret, Camille Lamare, Martine Guiraud, Nicolas Fazilleau, Agathe Bour, Bernard Malissen, Alice Carrier, and Sylvie Guerder. “Thymus-specific serine protease contributes to the diversification of the functional endogenous CD4 T cell receptor repertoire”. In: *The Journal of Experimental Medicine* 208.1 (2011), pp. 3–11.

[84] Guillaume Voisinne, Anne Gonzalez de Peredo, and Romain Roncagalli. “CD5, an Undercover Regulator of TCR Signaling”. In: *Frontiers in Immunology* 9 (2018), p. 2900.

[85] Lie Wang, Kathryn F Wildt, Jinfang Zhu, Xianyu Zhang, Lionel Feigenbaum, Lino Tessarollo, William E Paul, B J Fowlkes, and Rémy Bosselut. “Distinct functions for the transcription factors GATA-3 and ThPOK during intrathymic differentiation of CD4+ T cells”. In: *Nature Immunology* 9.10 (2008), pp. 1122–1130.

[86] Tobias Wertheimer et al. “Production of BMP4 by endothelial cells is crucial for endogenous thymic regeneration”. In: *Science Immunology* 3.19 (2018), eaal2736.

[87] J A Williams et al. “Thymic Medullary Epithelium and Thymocyte Self-Tolerance Require Cooperation between CD28-CD80/86 and CD40-CD40L Costimulatory Pathways”. In: *The Journal of Immunology* 192.2 (2014), pp. 630–640.

[88] Shiyun Xiao, Ivo D Shterev, Wen Zhang, Lauren Young, Jae-Hung Shieh, Malcolm Moore, Marcel van den Brink, Gregory D Sempowski, and Nancy R Manley. “Sublethal total body irradiation causes long-term deficits in thymus function by reducing lymphoid progenitors.” In: *The Journal of Immunology* 199.8 (2017), pp. 2701–2712.

[89] Yumi Yashiro-Ohtani, Takuya Ohtani, and Warren S Pear. “Notch regulation of early thymocyte development”. In: *Seminars in Immunology* 22.5 (2010), pp. 261–269.

[90] Andrew J Yates. “Theories and quantification of thymic selection”. In: *Frontiers in Immunology* 5 (2014), pp. 1–15.

[91] Ryo Yokota, Yuki Kaminaga, and Tetsuya J Kobayashi. “Quantification of Inter-Sample Differences in T-Cell Receptor Repertoires Using Sequence-Based Information”. In: *Frontiers in Immunology* 8 (2017), p. 1500.

[92] Daniela Zaharie, Radu D Moleriu, and Felix A Mic. “Modeling the development of the post-natal mouse thymus in the absence of bone marrow progenitors”. In: *Scientific Reports* 6 (2017), p. 36159.

[93] Jingjing Zhang, Romain Bedel, S Harsha Krovi, Kathryn D Tuttle, Bicheng Zhang, James Gross, Laurent Gapin, and Jennifer L Matsuda. “Mutation of the Traj18 gene segment using TALENs to generate Natural Killer T cell deficient mice”. In: *Scientific Reports* 6 (2016), p. 27375.

[94] Natalia Ziętara, Marcin Łyszkiewicz, Jacek Puchałka, Katrin Witzlau, Annika Reinhardt, Reinhold Förster, Oliver Pabst, Immo Prinz, and Andreas Krueger. “Multicongenic fate mapping quantification of dynamics of thymus colonization”. In: *The Journal of Experimental Medicine* 212.10 (2015), pp. 1589–1601.

List of publications and invited talks

Publications

Kazumasa B. Kaneko, Ryosuke Tateishi, Takahisa Miyao, Yuki Takakura, Nobuko Akiyama, Ryo Yokota, Taishin Akiyama, and Tetsuya J. Kobayashi. "Quantitative analysis reveals reciprocal regulations underlying recovery dynamics of thymocytes and thymic environment in mice". In: *Communications Biology* 2 (2019), 444.

Invited talks

Kazumasa B. Kaneko, R. Tateishi, T. Miyao, Y. Takakura, N. Akiyama, R. Yokota, T. Akiyama, and T. J. Kobayashi. Quantitative analysis of reciprocal regulations between thymocytes and thymic environment during recovery, One Day Workshop on Virus Dynamics in Japan 2018, Tokyo, November 2018

金子和正, 小林徹也. 細胞内シグナリングネットワークにおける応答時間を一定に保つメカニズム, 第 3 回理論免疫学ワークショップ, 秋田, 2019 年 1 月

金子和正, 横田亮, 秋山泰身, 小林徹也. 胸腺 T 細胞分化の数理モデリング, 第 2 回理論免疫学ワークショップ, 富山, 2018 年 2 月